ANTAL KERPELY DOCTORAL SCHOOL OF MATERIALS SCIENCE & TECHNOLOGY

High-Temperature Corrosion Resistance Investigation of Hot-Dip Aluminized Carbon Steel C45

A PhD Dissertation Submitted in Fulfillment of the Requirements for the Degree of Doctor of Philosophy in Material Science and Engineering

By

Hawkar Jalal Muhammed

Supervisor:

Prof. Dr. Tamás I. Török (Emeritus Professor)

Head of the Doctoral School

Prof. Dr. Valéria Mertinger

Institute of Chemical Metallurgy and Foundry Engineering

Faculty of Materials and Chemical Engineering

University of Miskolc, Hungary

Miskolc

2023

List of Symbols, Indices, and Abbreviations

Symbol	Description	Units
HDA	hot-dip aluminizing	
HEAs	high-entropy alloys	
TBCs	thermal barrier coatings	
PVD	physical vapor deposition	
IMC	intermetallic compound	
IMs	intermetallics	
HDG	hot-dip galvanizing	
ODS	oxide-dispersion strengthened	
HTSMA	high-temperature shape memory alloys	
HVOF	high velocity oxygen fuel	
CVD	chemical vapor deposition	
PHMS	polymethylhydrosiloxane	
YSZ	yttria-stabilized zirconia	
TGA	thermogravimetric analysis	
SEM	scanning electromicroscope	
EDS	energy-dispersive X-ray spectroscopy	
OIM	orientation imaging microscopy	
EBSD	electron backscatter diffraction	
SE	secondary electrons	
BSE	backscattered electrons	
GD-OES	glow discharge optical emission spectrometry	
PFIB	plasma focused ion beam	
ID	Interdiffusion	

Table of Contents

CHAPTER 1: Introduction

Operating metallic base materials in most structural components is still a practical matter. These materials have superior mechanical and physical properties, which are the primary reasons behind their application. Incineration, heat-exchanger, power station, and turbine blades are examples of structural components.

A metallic material functions in high-temperature environments requires special features, such as corrosion resistance, that enable it to operate in these harsh environments without rapidly degrading and failing catastrophically. Although in order to overcome the abovementioned problem, alloying the metals, first of all the iron base alloys, with elements such as Cr, Ni, Al, and Si is considered a viable solution, as these elements have stable, protective oxide layers that act as a barrier and mitigate against the flow of oxygen as well as other corrosive agents to the base metal. In this context, a recent focus has been placed also on high entropy alloys. Alternatively, a suitable coating and/or surface modification by, for example, surface alloying can be applied to protect the base metal component. There are a variety of coating techniques, such as PVD, CVD, HVOF, HDA, HDG, etc. However, it is important to note that the usage of these techniques depends on several factors, such as cost, the level of quality or the purpose of the coating, the type of protective layer/substance, and the type of substrate/base component to be used.

Temperature ranges from low to high, and extremely high temperatures can be used to categorize operating environments. Specifying the proper metallic base material according to the operating temperature is essential, hereinafter some possible metals type usage versus working temperatures are worth mentioning, like those low-alloy steels, which form M_3O_4 (M=Fe, Cr) surface layers/scales, and are used to temperatures of about or below 500 ºC in hot air. Titanium-base alloys form TiO_2 and are used up to about 600 ºC. Ferritic stainless steels, which form Cr_2O_3 passive layer, are used to about 650 ºC. Austenitic Fe–Ni–Cr alloys, which form Cr_2O_3 passive layer, are used to about 850 ºC. Austenitic Ni–Cr alloys, which form Cr_2O_3 passive layer, are used to about 950 ºC. Austenitic Ni–Cr–Al alloys, aluminides, and MCrAlY (M = Ni, Co, or Fe) coatings, which form Al_2O_3 passive layer, are used to about 1100 ºC. Applications above 1100 ºC require the use of ceramics or refractory metals.

For decades, scientists/researchers have attempted to understand, explore, and illustrate the oxidation/corrosion phenomena at elevated temperatures. Interactions, diffusion, structural changes, phase changes, intermetallic evolution, and interfacial reaction have been the primary focus of their research. To manage the component's performance and real operating-life time, continuous study is necessary to assess the metal base material intended for use in high-temperature environments, either bare or coated.

One of the key advantages of hot-dip aluminizing (HDA) is that it provides superior corrosion resistance at high temperatures owing to the formation of a stable aluminum oxide layer that prevents corrosion from damaging the base metal, besides the simplicity and cost-effectiveness.

The primary purpose of this PhD program and research work was to use an inexpensive iron base metal, that was the carbon steel C45, coated with the most straightforward and inexpensive coating technique, i.e., HDA. During the PhD research period of several years, first, setting up the necessities to perform laboratory HDA experiments was achieved, where preparations included the molten bath consisting of commercially pure aluminum as well as the preparations of the steel specimens for coating. Then, sophisticated metallographic technology available at the University of Miskolc, Faculty of Material Science and Chemical Engineering was employed to characterize the morphologies, structures, and mechanical properties and reported accordingly. Afterward, several corrosion resistance examinations were designed and utilized to investigate the structural changes of HDA carbon steel C45, corrosion kinetics, and imitate the same conditions as the actual component serving. Before HDA, attempts were made to pre-coat the specimens, followed by a structural evaluation to reveal the precoat layer's effect on the intermetallic layer's evolution at the interface. All are reported in this PhD dissertation, and appropriate explanations and discussions are provided with firm and possible causes of the changes.

CHAPTER 2: Literature review

2.1 Corrosion

Corrosion is an inevitable process that inflicts significant harm to structures and materials through its reaction with the surrounding environment. This harmful process leads to the generation of compounds such as oxides and salts that significantly impact various industries, including transportation, infrastructure, manufacturing, and energy production. Globally, corrosion has a tremendous economic impact, estimated to be several trillions of Euro/Dollars per year [1].

Corrosion can manifest itself in different forms on metal surfaces, including uniform, pitting, crevice, and galvanic. It's important to note that various factors contribute to corrosion, such as the type of material, the environmental conditions, and the presence of contaminants. These factors significantly influence the extent and severity of corrosion [2,3].

2.2 High temperatures oxidation in air

High-temperature oxidation occurs when materials are exposed to high temperatures in the presence of oxygen. This reaction leads to the generation of oxide layers on the material's surface, which can significantly impact its properties. Industries such as aerospace, power generation, and metallurgy are highly concerned with this process because it can have diverse impacts on the efficiency and reliability of components and structures operating at high temperatures. This is particularly crucial in the aerospace industry.

Equation (1) (where (M) represents a metal) in itself does not yet demonstrate the complexity of the oxidation process. It is crucial to note that a higher temperature accelerates the reaction rate, leading to the formation of oxide layers at a faster rate. Various factors, including the composition of the material, temperature, and partial pressure of oxygen heavily influence the properties of the oxide layer.

$$2M + O_2 \rightarrow 2MO \qquad (1)$$

Numerous techniques have been devised for analyzing high-temperature oxidation, such as thermogravimetric analysis, X-ray diffraction, and scanning electron microscopy. These methods offer valuable glimpses into the oxide layers' characteristics and facilitate comprehension of oxidation mechanisms.

Materials used in high-temperature applications face a significant challenge in oxidation at high temperatures. Oxide layers can adversely affect their mechanical, thermal, and electrical properties, leading to a drop in performance and early failure. As a result, it is crucial to

comprehend the oxidation mechanisms and create effective preventive measures in order to guarantee safe and dependable functioning in high-temperature applications [4,5].

2.3 High temperatures corrosion in molten salt

Iron-based materials used in structural engineering are frequently subjected to high-temperature environments, including gases, melts, and particles in power plants, waste incinerators, and chemical processing plants. This exposure causes the materials to absorb and transfer heat from their surroundings, leading to degradation, such as surface scale formation in hot air. Corrosion processes, including oxidation, are also accelerated by time and temperature fluctuations. Elements such as chlorine, sulfur, sodium, and vanadium often exacerbate corrosion degradation, particularly at high temperatures [4]. Due to aggressive chemical components reacting with surfaces, the formation of new corrosion products, or new scale, weakens the adhesion and permits corrosion species to penetrate and react with the matrix. These processes also produce mechanical stresses that, when coupled with attacks, will severely compromise the components' performance and potentially lead to failure [4].

Corrosion at high temperatures is an extremely critical engineering issue requiring utmost care before utilizing any material component. Many studies have been carried out to examine closely the subject impact of various harsh environments simulated at elevated temperatures on different carbon steels [6] as well as the impact of chlorine on bare carbon steel [7] when corrosion accelerates due to cyclic oxychlorination. Iron oxides (Fe_xO_y) can spall off and weaken the components as iron oxidizes. The degradation of dual-phase steel substrates was observed to occur even at low temperatures using a chloride-based solution [8]. The production of a passive protective film is crucial for achieving sustainable performance in high-temperature environments. Elements such as aluminum and chromium serve as exceptional examples in this regard [9].

The examination of the corrosion and oxidation behavior of high alloy steels and stainless steels with exceptional heat and corrosion resistance has been conducted at high temperatures in the presence of sulfur and chlorine in various forms, including gases, deposited salts, or molten salts [10-16]. Furthermore, in the case special coatings, such as aluminizing [17,18], to enhance the durability of steel components in extreme environments, it is crucial to reduce the rate at which they degrade. However, it is worth noting that protective measures and techniques are susceptible to deterioration, which is often influenced by kinetic factors, diffusion rates, and thermodynamics. For instance, it has been proven that deposited salt mixtures, such as NaCl and Na_2SO_4 in varying concentration ratios, can significantly accelerate the corrosion of low-carbon steel [7], and the chloride and sulfur present cause corrosion.

2.4 Methods for corrosion mitigation

The problem of corrosion is a persistent and expensive issue affecting various industries, infrastructure, and everyday objects. This happens when metals react with their surroundings and lose their structural integrity and properties. Corrosion in high-temperature environments brings its own set of challenges due to the increased chemical reactivity at elevated temperatures that hasten degradation processes. Specialized methods are necessary to mitigate corrosion in these conditions. The primary aim of corrosion mitigation techniques is to prevent or slow down the corrosion process, thereby extending the lifespan and reliability of materials. Protective coatings, alloying, cathodic protection, environmental control, corrosion inhibitors, monitoring, and inspection are some of the techniques used to prevent corrosion.

The mitigation of corrosion in high-temperature environments relies heavily on two crucial parameters: protective coatings and alloying of the metal substrate. It is imperative to utilize appropriate protective coatings and alloying techniques to safeguard materials against the harmful effects of corrosion. This will guarantee prolonged service life and enhanced performance, ensuring that materials remain in top condition.

2.4.1 Material improvements functioning at high-temperatures

Effective performance at high temperatures is absolutely critical for various industries, including aerospace, power generation, automotive, and manufacturing. High-temperature environments are extremely challenging, with increased reactivity, thermal stresses, and accelerated degradation processes. However, thanks to material science and engineering advancements, novel materials have been developed that are capable of withstanding and performing well under extreme temperatures. For high-temperature materials to maintain their integrity and functionality in harsh environments, they must possess exceptional thermal stability, mechanical strength, chemical resistance, and corrosion resistance. These materials are designed to endure elevated temperatures, thermal cycling, and exposure to corrosive gases, molten metals, or intense radiation. Withstanding these extreme conditions contributes significantly to improved safety, enhanced performance, and extended service life of components and systems operating at high temperatures. Choosing or developing appropriate alloys, ceramics, composites, and coatings is essential for improving high-temperature material. These materials possess exceptional properties that enable them to endure extreme temperatures without succumbing to thermal degradation, oxidation, or mechanical failure. Developing new materials that boast customized microstructures, superior creep resistance, and heightened thermal stability has opened up a whole new realm of possibilities for their use in high-temperature environments.

Silicon carbide and alumina are indisputably perfect for deployment in extreme conditions thanks to their exceptional thermal stability, low thermal expansion, and chemical attack resistance [19]. Utilizing reinforcement materials like carbon fibers or ceramic particles

embedded in a matrix material, composite materials synergistically improve properties and provide high-temperature performance [20]. It is essential to utilize cutting-edge processing techniques and manufacturing methods and carefully select appropriate materials to achieve desired properties in high-temperature materials. Advanced fabrication techniques, including powder metallurgy, sintering, chemical vapor deposition, and hot isostatic pressing, offer unparalleled precision in microstructure control, unparalleled improvement in mechanical properties, and unparalleled customization in composition [21]. Advancements in high-temperature material improvements have made significant progress in critical areas, including gas turbines, heat exchangers, exhaust systems, and aerospace components. These materials enable efficient energy conversion, enhance thermal management, and improve overall system performance at elevated temperatures [22].

Alloys intended for high-temperature applications often incorporate chromium, nickel, molybdenum, and cobalt elements. These alloying elements are essential to forming protective oxide scales, sustaining mechanical strength, and enhancing corrosion resistance at elevated temperatures [23]. Alloying the base metal component is an absolute must for effective corrosion mitigation. By adding specific alloying elements to a base metal, the resulting alloy can exhibit vastly improved resistance to corrosion. For instance, adding chromium to steel forms stainless steel, which boasts unparalleled corrosion resistance thanks to the initiation of a passive oxide layer on the surface. This is a no-brainer when it comes to preventing corrosion [24,25]. The selection process must be meticulously scrutinized of alloys based on the particular application and the corrosive environment in which the material will be utilized. Not to do so can result in serious consequences.

Alloying elements like aluminum, nickel, and molybdenum can significantly improve high-temperature corrosion resistance in addition to chromium. The addition of aluminum, for instance, forms a protective aluminum oxide scale that enhances corrosion resistance at elevated temperatures [26]. It is imperative to utilize nickel-based alloys in industries that are subjected to harsh, high-temperature environments. This is due to their exceptional ability to withstand oxidation and sulfidation [27]. The presence of alloying elements serves as a strong barrier against the harmful effects of corrosive species. It effectively prevents the formation of damaging phases while simultaneously facilitating the formation of protective oxides or scales on the surface of the metal.

Entropy alloys have become a captivating class of materials in the field of materials science due to their exceptional mechanical, thermal, and corrosion-resistant properties. Unlike traditional alloys that rely on specific compositions, entropy alloys possess a random or nearly random arrangement of elements, resulting in an extraordinary level of disorder. This unique atomic configuration makes entropy alloys ideal for use in high-temperature applications [28].

High-entropy alloys (HEAs), researchers and engineers have shown a great interest in this topic worldwide since their introduction in the early 2000s. These alloys consist of three or more elements in equimolar proportions, resulting in a solid solution with a disordered atomic structure. By deliberately incorporating multiple elements into the alloy, the concept of configurational entropy can be utilized to enhance its performance [28]. Entropy alloys possess a unique characteristic that enables them to form solid solutions with exceptional lattice distortion. This exceptional ability significantly enhances the material's mechanical properties, resulting in remarkable strength and stability. Moreover, their outstanding resistance to thermal creep, oxidation, and corrosion makes them ideal for use in extreme environments, particularly those with high temperatures [29].

Various types of entropy alloys have been developed, each with its own set of elements and unique properties. One of the most notable is the refractory-based entropy alloys which incorporate highly resistant elements such as tungsten, molybdenum, and tantalum. These alloys exhibit remarkable strength even at elevated temperatures and demonstrate excellent resistance to thermal degradation. Hence, they are the ideal choice for applications in gas turbines, jet engines, and other high-temperature machinery [30]. The oxide-dispersion-strengthened (ODS) alloy is a type of entropy alloy that is highly resilient to creep deformation, oxidation, and high-temperature corrosion. This is achieved by dispersing nano-sized oxide particles within a metallic matrix. Due to these properties, the ODS alloy is might seem to be an ideal for use in applications such as nuclear reactors, aerospace components, and power plants [31].

It is important to note that HTSMAs are a highly sought-after class of entropy alloys. These alloys can recover their original shape even at high temperatures, making them an ideal choice for industries that require precise shape recovery, such as aerospace, automotive, and biomedical sectors. Their unique properties make them a valuable asset and have gained significant attention in recent years [32].

2.4.2 Coatings at high temperature

Protective coatings are a highly effective method for mitigating corrosion on metal surfaces. These coatings act as an impenetrable barrier that prevents direct contact between the metal and the corrosive environment. Organic coatings, including paints, varnishes, and polymer films, are commonly utilized for this purpose [28,29]. These coatings serve as a crucial physical barrier that effectively shields metal surfaces from corrosive agents such as moisture, chemicals, and atmospheric pollutants. With advancements in coating technologies, traditional protective coatings are no longer the only solution available for corrosion mitigation. Nano coatings have garnered significant attention due to their unique properties and superior performance. By utilizing nanomaterials such as nanoparticles or nanocomposites, these coatings are able to form an ultra-thin protective layer on the metal surface, thus providing unmatched corrosion resistance [35]. Nano coatings with high surface area and tailored

composition are essential for effective barrier properties and enhanced resistance to corrosion. Additionally, self-healing coatings represent a highly promising solution, as they are able to autonomously repair any damage or breaches, providing long-term protection against corrosion [36]. Self-healing mechanisms must include the immediate release of potent corrosion inhibitors, the prompt sealing of cracks through encapsulated materials, or the swift activation of intrinsic healing agents.

It is crucial to use specialized methods to prevent corrosion in high-temperature environments. In order to ensure longer service life and better performance, it is necessary to employ protective coatings that can shield materials from the harmful effects of corrosion. Protective coatings are essential in mitigating corrosion in high-temperature environments, as they create a barrier between the metal substrate and corrosive elements. For these coatings to be effective in these extreme conditions, they must possess exceptional thermal stability, chemical resistance, and adhesion to the substrate [37]. Thermal barrier coatings (TBCs) are widely used in high-temperature applications, and they usually comprise ceramic materials such as yttria-stabilized zirconia (YSZ) [38]. TBCs offer a safeguarding layer against high temperatures that shield the metal substrate from oxidation, thermal cycling, and corrosive environments. Additionally, TBCs are effective in restricting the diffusion of corrosive agents into the metal, which leads to a decrease in the corrosion rate.

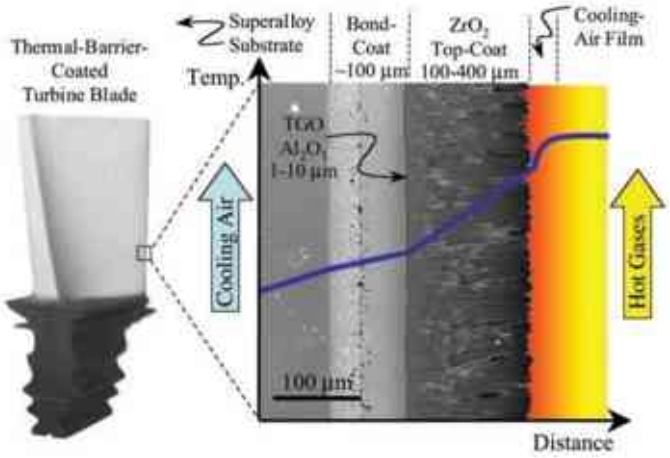

Figure 1. Cross-sectional SEM of an EB-PVD TBC with a schematic diagram showing temperature (blue curve) reduction [39].

High-temperature environments require protective coatings that possess exceptional thermal stability and resistance to chemical attack. High-temperature-resistant polymers or inorganic coatings fall under this class and have proven to be effective at mitigating high-temperature corrosion. Promising results have been observed with silicone-based polymers and inorganic coatings such as aluminum silicates [40]. The coatings have the ability to create a compact and firmly attached layer on the metal base, which efficiently obstructs the entry of corrosive elements and diminishes the spread of detrimental substances into the material.

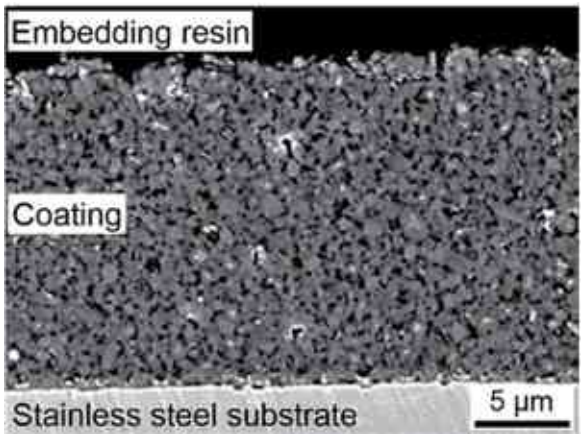

Figure 2. After being pyrolyzed in the air at 800 ºC for 2 hours, coatings containing polysiloxane PHMS and $TiSi_2$ as active fillers [41].

It's worth considering metallic coatings like aluminizing and chromizing for high-temperature applications. These coatings are great for preventing oxidation and can also improve the material's high-temperature capabilities.

For instance, a study by Dutta et al. [42], titled "Development of Aluminide Coatings on Ni-Cr-Fe Based Superalloy 690 Substrates For High-Temperature Applications Using Atmospheric Plasma Spraying Technique" can well demonstrate this. The research team examined aluminide coatings on nickel-based superalloys, focusing on assessing their ability to resist high-temperature oxidation, adhere to the substrate, and enhance the mechanical properties of the coated material. The findings of the study underscored the potential of aluminide coatings to safeguard superalloys at elevated temperatures and improve their overall performance in harsh environments.

2.5 Coating processes

Applying a layer of material onto a substrate is known as coating technology. This technique is commonly used to enhance a product's properties, appearance, or functionality. Coatings are prevalent across many industries and applications, from consumer products to industrial machinery. Several types of coating technologies are available, each with unique characteristics and uses. The following are some of the most common types of coating technologies, also being relevant to the present study.

2.5.1 Electroplating

Electroplating is a crucial surface treatment process utilized across various industries to enhance the properties and aesthetics of materials via the controlled deposition of a thin metal layer onto a substrate. This technique is pivotal in improving several products' functionality, durability, and appearance, including consumer goods and industrial components.

Electroplating employs an electrolytic process whereby a metal ion solution deposits metal atoms onto a conductive surface. It has garnered significant consideration due to its ability to modify the surface properties of materials, providing benefits such as improved corrosion resistance, enhanced electrical conductivity, and even decorative finishes. The electroplating process commences with the meticulous preparation of both the substrate and plating solution. The substrate, commonly made of a metal or conductive material, undergoes thorough cleaning and preparation to ensure proper adhesion of the plated layer. The plating solution, consisting of metal ions of the desired plating material, is meticulously chosen based on the coated object's intended application and desired properties [43].

During electroplating, an external power source must be utilized to create an electric field between the substrate (acting as the cathode) and the anode, typically composed of the metal to be plated. This electric field forcefully drives the movement of metal ions from the plating solution toward the substrate's surface. Once the metal ions reach the substrate, they undergo reduction reactions, creating a continuous and adherent layer of metal atoms on the substrate's surface. Electroplating offers unparalleled versatility in producing coatings with tailored properties. The precision with which the thickness of the deposited layer can be controlled by adjusting factors such as plating time and current density makes it an essential technique in applications where specific durability, conductivity, or appearance requirements must be met. Moreover, the range of available plating materials allows for the customization of properties, making electroplating the go-to solution for applications as diverse as automotive parts, electronics, jewelry, and aerospace components [44].

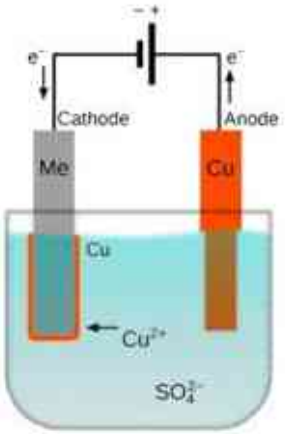

Figure 3. Electroplating schematic of copper deposition [45].

2.5.2 Physical Vapor Deposition (PVD)

In a vacuum setting, PVD entails the evaporation or sputtering of a material that condenses and produces a thin film on a substrate. This technique is frequently employed to fabricate decorative coverings for jewelry and watches and functional coatings for cutting tools and

semiconductor devices [46, 47], The schematic principle of the deposition mechanism of the PVD is illustrated in Figure (4).

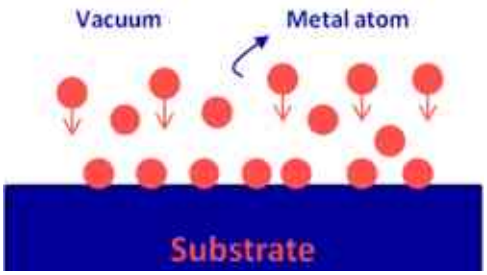

Figure 4. Schematic of the vacuum/PVD metal deposition process [48].

To obtain vaporized metal, sputtering or thermal heating can be used. It is imperative to evacuate the chamber before starting the sputtering process. Argon gas is then injected into the chamber at low pressure (in our case, 2.8 $\times 10^{-2}$ mbar to 5.7 $\times 10^{-3}$ mbar). The potential difference between the target metal and the substrate will excite the argon atoms, forming Ar^{+} ions and transforming the neutral argon gas to argon plasma. The ionized argon atoms will collide with the metal target and remove metal atoms, which will then travel toward the substrate and deposit on its surface, creating the coating. Figure 5 illustrates the process schematic of producing a film on the substrate.

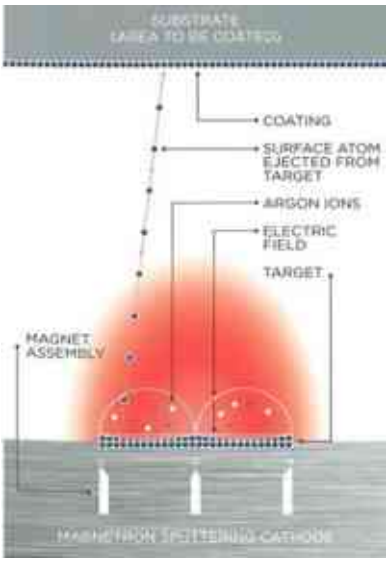

Figure 5. The schematic of the magnetron sputtering PVD process of producing a thin film coating the substrate [48].

2.5.3 Slurry-type coating

The slurry-type coating is an absolute must-have when it comes to applying thin and uniform layers of materials onto surfaces. This technique uses a mixture, or slurry, composed of coating material particles suspended in a liquid medium to the substrate. Slurry-type coatings are employed in various industries, including electronics, optics, and manufacturing, where precise control over layer thickness, surface quality, and material composition is critical. This method

offers advantages such as ease of application, adaptability to different substrate shapes, and achieving high-quality coatings with tailored properties.

Today, several commercial companies use the slurry technique of aluminizing for protection against high-temperature oxidation up to 1000°C, particularly in the gas turbine's hot section. An organic binder is essential for creating slurries. However, volatile organic compounds are released during the heat treatment process, which poses a serious danger to workers and the environment. To mitigate this risk, it is crucial to use a suitable organic binder such as polyvinyl alcohol (PVA). PVA is an excellent choice due to its ability to act as a binder, its water solubility, and its ability to protect aluminum surfaces by adsorbing them. In fact, PVA is the preferred water-based binder due to its superior physicochemical characteristics [49]. Figure 6 shows the chemical representation of polyvinyl alcohol (PVA) molecules.

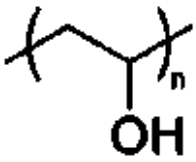

Figure 6. Chemical structure of polyvinyl alcohol (PVA) [50].

In the highly innovative and rather complex slurry-type "PARTICOAT" coating project [51]the slurry performance could be effectively managed by utilizing micro-sphere Al particles to generate hollow alumina spheres on the topcoat after Al diffusion into the substrate. As a result, this structured coating delivers both thermal insulating and oxidation-resistant properties [51]. The steps for coating the surface with this slurry-type aluminizing are illustrated in Figure 7. The aluminum microparticles are suspended in a binder (PVA) and then sintered. However, it is crucial to note that post-heat treatment is required to diffuse the aluminum toward the substrate. The coating structure comprises aluminum in the top layer, followed by intermetallic and then the substrate.

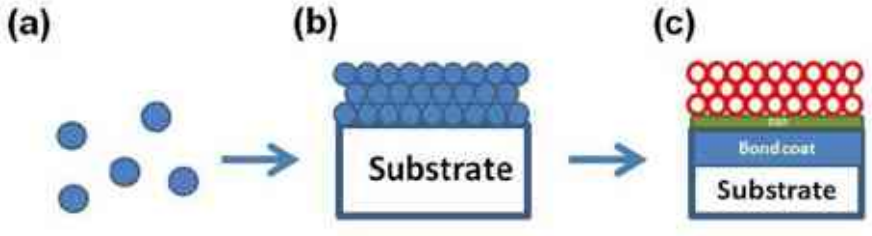

Figure 7. The PARTICOAT coating concept with the Al microspheres (a) initially embedded in a binder then deposited on the substrate (b), followed by a proper thermal treatment resulting in the illustrated structure (c) composed of a bond coat which is linked to a ceramic topcoat foam having a thermally grown oxide scale [51]

Studies have conclusively proven that implementing slurry-type aluminizing is crucial to safeguarding the surface and enhancing the surface characteristics of various materials. This is

particularly relevant for materials that are used in environments with high temperatures and exposure to different gases that cause surface degradation. B. Grégoire et al. [52] implemented a new design on slurry coating the surface of polycrystalline Ni20Cr and directionally solidified superalloy CM-247 LC. The substrate was enriched with micro-particles of Cr as the first layer and micro-particles of Al on top. The intermetallic compound of Al-Cr acted as a barrier to molten Al microparticles by restraining exothermic reactions between Ni-based superalloy and molten aluminum. As a result, at 700 °C annealing, the diffusion of Al towards the substrate decreased, while at 1100°C annealing, the diffusion of Ni outwards was promoted, leading to the formation of β-NiAl. J. Lu et al. [53] have thoroughly studied the characteristics of the slurry aluminized inner face of the super 304H boiler tube under steam temperature reaching 650 °C. The results unequivocally revealed that the resistance of steam oxidation of super 304H has been significantly improved through the formation of a thin scale of Al_2O_3 on the surface. The sequence of the slurry-type coating procedure steps is clearly demonstrated in Figure 8. Firstly, the inside of the super 304H tube was meticulously cleaned using acid. Then, the slurry was used as a coating, which was subsequently dried and cured. Finally, the tube was prepared as a closed chamber to carry out the post-heat treatment to form the desired coat on the inner surface of the tube.

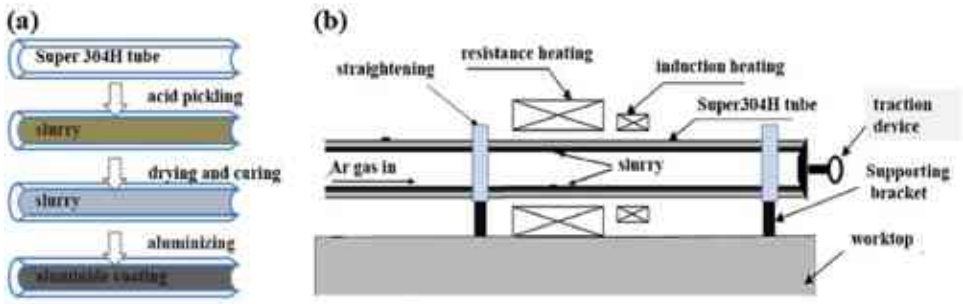

Figure 8. Processing steps for inner surface aluminizing starting with cleaning then coating the inside surface of a super 304H tube (a); and schematic diagram of the coating deposition device (b) [53].

The steel used in high temperatures and humid environments especially those used in waste incineration plants, required protective coating that was developed by M. D. Nguyen et al. [54] who successfully deposited 162 μm thick glass-ceramic coatings on S45C JIS G 4051 carbon steel using water glass as a binder, Al powder as active filler, Cr_2O_3 powder as passive filler, and NiO powder as reduction agent. An enhancement technique was conducted to achieve crack-free coatings that demonstrated high performance in oxidizing environments. The developed coating might be used on steel in such environments. New concepts of Al-Si slurry-type coating have been studied by J. T. Bauer et al. [55] where barrier, eutectic, and oxygen getter concepts were all used to reduce critical gases and pressure of oxygen in the alloy (800H) used in power plants and the chemical industry. The best result was achieved with the barrier concept and homogenous diffusion coating under a second protective layer near the substrate within the aluminum-containing slurry.

B. Bouchaud et al. [56] studied the sintered slurry containing spherical microparticles of Al with an interlayer of ceria (CeO_2) electro-synthesized on the growth of thermal barrier coating TBC, the interlayer of ceria restricts or is limiting the upward diffusion of Cr and segregates the formation of intermetallic layer of Al_xCr_y, at annealing temperature about 1100 °C for two hours; the formation of β-NiAl will result thicker than that obtained without interlayer and a sintering of Al_2O_3 particles will promote thicker crust. The thickness of the slurry has an effect on the morphology and composition this study has been carried out by A. J. Rasmussen et al. [57] the results of coating the superalloy Inconel 690 reveal a thick aluminide coating that has a precipitate-free inner layer of Ni-rich β-NiAl, an outer layer of Al-rich β-NiAl with many α-Cr precipitates is formed and a thin aluminide that composed of a single layer of Ni-rich β-NiAl matrix containing few large Cr precipitates with a high P content.
Further investigation on different kinds of steels carried out by X. Montero et al. [58] whose studies have been done on AISI 347, P91, 10CrMo9-10, and K41 as a substrate focusing on the aluminide formation mechanism different parameters such as steel surface finishes, heat treatment atmosphere, and steel composition were studied, the results reveal that the post-heat treatment in argon atmosphere will provide protection versus oxidation instead of air atmosphere, especially for iron that oxidizes faster in air, heat treating of different kind of steels at 680 °C in argon atmosphere showed that increasing of Cr content the probability of uncoated surface is increased. The experiment's outcome revealed that the formation of aluminide with a thicker layer and homogenous structure is provided by small grain size and high roughness. All in all, for the purpose of utilizing aluminum and/or alumina for developing more effective protective surface layers on special refractory alloys, it is well demonstrated by the above reviewed new studies, that the potential in such approach is promising, but the required multistep technologies are rather complex and must be quite expensive as well.

2.5.4 Hot-dip process

Hot-dip coating process is an essential and widely recognized process in the realm of surface coating and corrosion protection for various metallic materials. This technique involves immersing a metal substrate, typically steel or iron, into a molten metal or metal alloy bath (common metals used for hot-dip coat are zinc and aluminum). The result is a robust metallurgically bonded layer of metal or metal-based alloy on the surface of the substrate. This protective layer provides exceptional corrosion resistance, prolongs the material's lifespan, and improves its aesthetic appeal [59].

The hot-dip coating process is primarily carried out through batch-type dip coating and continuous-type coating, depending on the component's geometry that requires coating. It is crucial to note that both methods consist of several vital stages.

1. **Surface preparation:** Thorough cleaning of the metal substrate is necessary before initiating the coating process to eliminate all contaminants, including rust, grease, and

dirt. This critical step guarantees the appropriate adherence of the metal coating to the substrate.

2. **Fluxing:** The metal must be immersed in a flux solution after cleaning to ensure surface cleanliness and facilitate the reaction with the molten metal.
3. **Dipping:** After cleaning and fluxing, the metal must be immediately dipped into a precisely regulated molten metal or metal alloy bath. This is crucial to achieve the desired thickness and adhesion of the coating. Any delay or deviation from this procedure could result in a subpar final product.
4. **Alloy formation:** As soon as the metal is dipped into the molten metal, a remarkable metallurgical reaction occurs between the coated metal and iron in the substrate. This results in the development of multiple layers of metal-iron alloy called intermetallic (IM) that are firmly bonded to the underlying metal.
5. **Cooling and solidification:** After coating the substrate with metal, it is taken out of the bath and left to cool and solidify. The resulting metal coating adheres firmly to the substrate, offering excellent protection against corrosion.

The process of hot dip coating can be performed by following the instructions provided in Figure 9.

Hot-dip coating process offers numerous advantages:

1. **Exceptional corrosion protection:** The metal coating serves as a crucial sacrificial barrier that undergoes corrosion over time, providing impregnable protection to the underlying substrate against hazardous environmental elements.
2. **Longevity:** Hot-dip coatings boast unparalleled durability, providing superior longevity for both structures and components.
3. **Uniform coating:** This process ensures consistent and seamless coverage, even on intricate structures and areas.
4. **Cost-effective:** Hot-dip coating is unequivocally the most cost-effective solution for corrosion protection compared to any other coating methods available.
5. **Low maintenance:** Hot-dip-coated structures demand little upkeep, thus lowering overall maintenance expenses in the long run.
6. **Aesthetic appeal:** A freshly galvanized/ aluminized surface can possess an aesthetically pleasing silver-gray appearance. Furthermore, it is capable of being painted over if desired.
7. **Environmental benefits:** It is important to note that hot-dip coating is not only sustainable but also highly efficient. Zinc and aluminum, being widely available materials, can be easily recycled, making it an ideal choice for many industries.

Hot-dip coating technology plays a crucial role in supporting a range of industries, such as construction, automotive, agriculture, transportation, and manufacturing. This technology is

particularly advantageous for products that are exposed to harsh environmental factors, such as outdoor infrastructure, utility poles, guardrails, and diverse metal components [60].

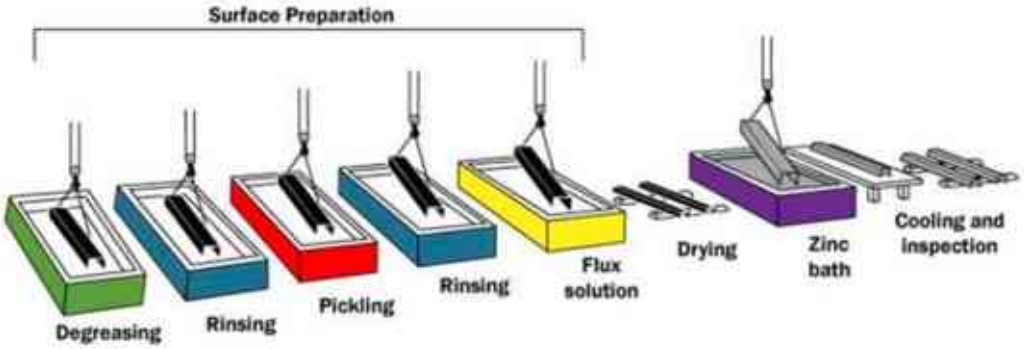

Figure 9. Scheme of a batch-type hot galvanized method [61].

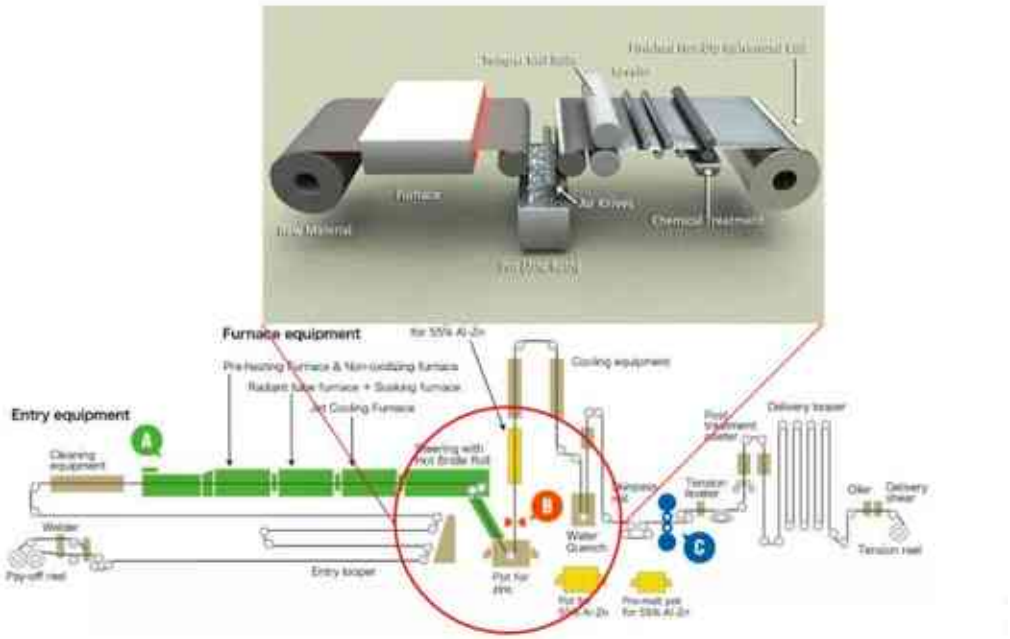

Figure 10. Schematic diagram clearly depicting the continuous hot-dip galvanizing line (Galvalume) [62] where the red circled area reveals the coating stage [63] with the air knives (B). The important pre-treatment steps (A) and one of the post-treatment steps (temper mill) are also indicated (C)

2.6 Aluminizing

Enhancing a substrate's surface through adding aluminum (or aluminum alloy) is known as aluminizing. This process generates a top layer of aluminum oxide (α-Al_2O_3) beneath which intermetallic compounds are produced, leading to improved mechanical and oxidation resistance properties. There are several methods available to apply aluminum coatings onto metals [64]:

1. Spray aluminizing.
2. Hot-dipping.
3. Calorizing.
4. Vacuum deposition.
5. Electroplating.
6. Vapor deposition.
7. Cladding.

2.7 Hot-dip aluminizing

In the process of hot-dip aluminizing, the molten bath is composed of either pure aluminum or an aluminum alloy [64]. There are two types of aluminum coating available, Type I and Type II, each having its own specific use and application depending on environmental conditions. Type I is made of an aluminum-silicon alloy that can withstand high temperatures and is easy to form. The addition of silicon or other alloying agents improves the stability of the compound and prevents the formation of the unstable iron-aluminum intermetallic compound. Type II, on the other hand, involves immersing steel in pure aluminum, which is best suited for outdoor steel structures that require protection against atmospheric corrosion [47,65].

2.7.1 Characterization of hot-dip aluminized steels

The corrosion resistance of aluminum and the high strength of steel, a thought to combine these two properties with one has been coming out. The coating of steel with aluminum might be performed with several techniques, but the most economical is the use of the hot-dip route [66]. The study of the intermetallic compound produced between aluminum and iron focuses on analyzing the Fe-Al phase diagram. Figure 11 displays various phases that arise from different aluminum-to-iron percentages, each with unique characteristics.

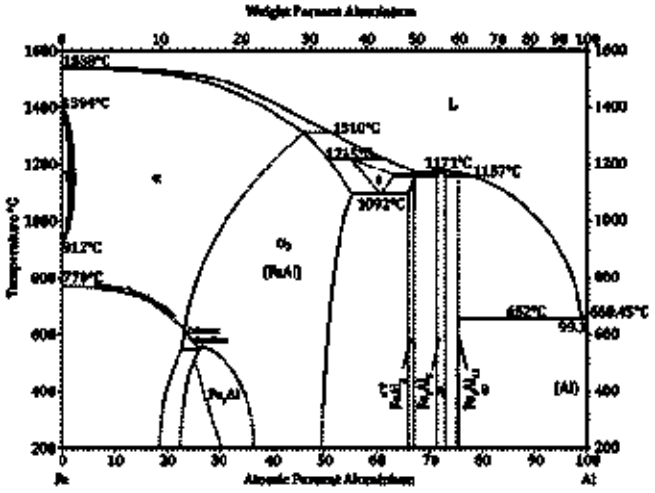

Figure 11. Fe-Al phase diagram [67].

The coating's structure is made up of an oxide layer of α-Al_2O_3, followed by a layer of aluminum-containing intermetallic compounds dispersed in the form of flake or acicular, and

then an intermetallic layer consisting mainly of two prominent phases: $FeAl_3$, which is thinner than the Fe_2Al_5 formed from the substrate side. The thickness of the coating layer depends on the dipping time and the temperature of the molten path.

Numerous studies and experimental research have been conducted to examine the impact of various parameters on the Fe-Al properties. Proper protection against high-temperature corrosion/oxidation can be achieved by controlling the factors that affect the coat's quality. In hot-dip aluminizing, three factors (dipping time, aluminizing temperature, and alloying aluminum) are critical in determining the structure properties of the intermetallic formed during the interfacial reaction between molten aluminum and solid iron and, consequently, the coating.

2.7.2 Dipping time

The duration of the dipping and soaking process during the coating/aluminizing of the part directly impacts the thickness of the topcoat aluminum and the intermetallic thickness. A longer duration will result in a thicker intermetallic layer.

By Cheng and Wang [68] the Fe-Al intermetallic growth mechanism and dipping time's effect on aluminide mild steel were analyzed using electron backscattering diffraction (EBSD). The intermetallic layer consisted of a top layer of aluminum, followed by a thinner layer of $FeAl_3$ and a major layer of Fe_2Al_5, which exhibited finger-like structures. Increasing the dipping time led to an observed increase in intermetallic layer thickness.

The thickness of the intermetallic layer shows a significant increase according to a parabolic law [69][70][71]. The thicknesses of the topcoat and intermetallic layers will be equally affected by the dipping time in two different aluminizing temperatures shown in Figure 12 (a) and (b). Additionally, increasing the dipping time while alloying the molten bath, it will also play a role in the thicknesses, albeit to a lesser extent [72]. It is a definitive conclusion that the dipping time's effect will remain constant in all circumstances. This means that any increase in the dipping time will undoubtedly result in an increase in the thickness of the intermetallic layer and the topcoat, albeit in different ways.

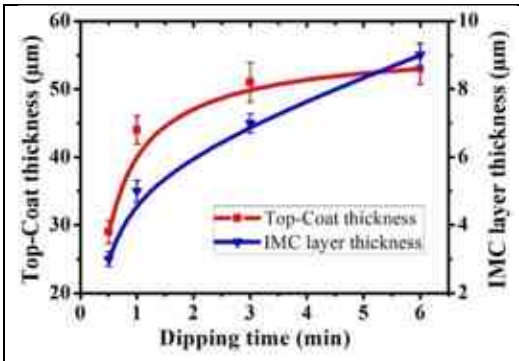

Figure 12(a). Shows intermetallic and topcoat aluminum thicknesses were HDA at 700 °C [69].

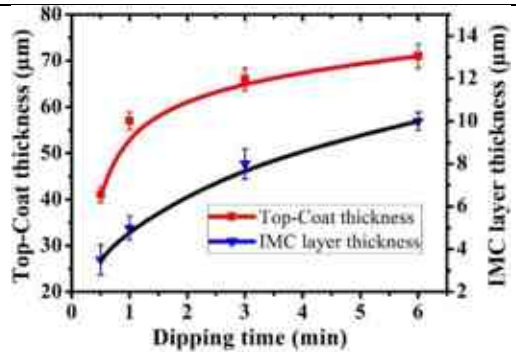

Figure 12(b). Shows intermetallic and topcoat aluminum thicknesses were HDA at 800 °C [70].

2.7.3 Aluminizing temperature

The term used to describe the temperature at which the specimen is immersed and retained in the molten aluminum bath is called the aluminizing/dipping temperature. Proper temperature control is critical in determining the aluminized coating's quality, thickness, and effectiveness. Achieving the desired microstructure and properties of the coating requires precise temperature control. It's worth noting that higher temperatures promote greater diffusion rates between aluminum and substrate atoms, leading to a thicker intermetallic layer. However, excessively high temperatures may pose challenges such as increased intermetallic brittleness and potential substrate deformation. On the other hand, lower temperatures may result in insufficient interdiffusion, leading to a thinner and less adherent coating.

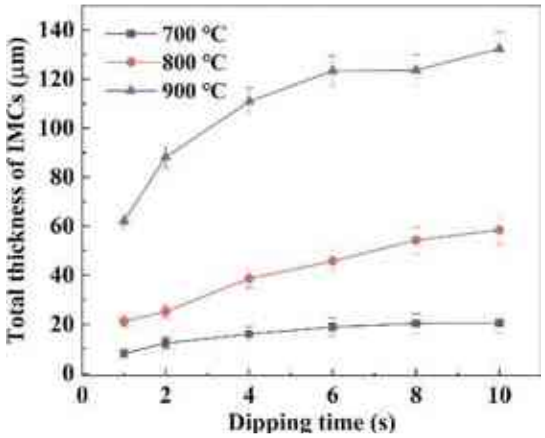

Figure 13. The correlation between total IMC thickness and dipping duration with three different aluminizing temperatures [73].

Figure 13 indisputably illustrates that the total thickness of the intermetallic layer increases in direct proportion to the aluminizing temperature.

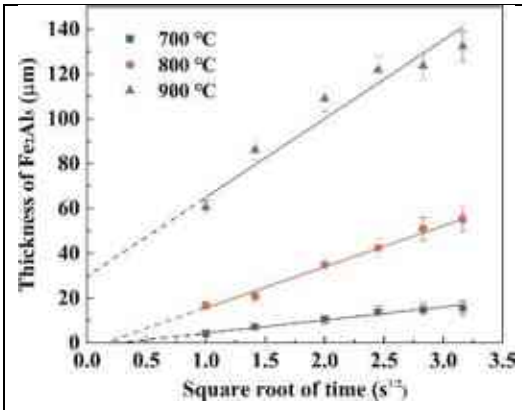

Figure 14(a). The relationship between the thickness of Fe_2Al_5 and $t^{0.5}$ is represented by linear fitting curves.

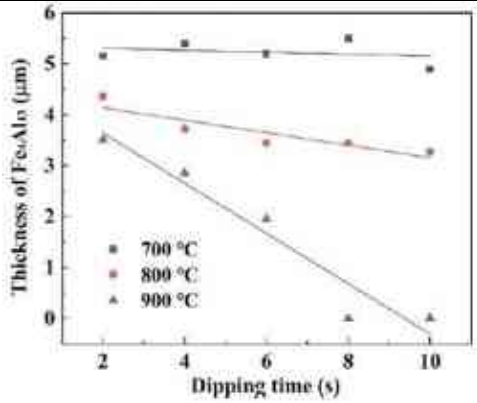

Figure 14(b). The linear relationship between the thickness of Fe_4Al_{13} and the dipping time and temperatures is being studied through a linear fitting.

The η-Fe_2Al_5 phase follows a parabolic thickness evolution, indicating that diffusion kinetics are the primary factor influenced by rising temperatures. Meanwhile, the θ-Fe_4Al_{13} phase displays a linear thickness evolution, indicating that interfacial kinetics are the dominant factor. As the reaction temperature and duration increase, the θ layer thickness decreases. Higher temperatures and longer reaction times facilitate the dissolution of the θ phase, leading to further thickness reduction [73].

To sum up, there is a direct correlation between the aluminizing temperature and the thickness of the intermetallic and topcoat aluminum layers. Any increase in the aluminizing temperature will unavoidably lead to an increase in the thickness of both layers.

2.7.4 Alloying the molten aluminum bath

The process of alloying a molten aluminum bath involves adding an element (M) to the bath to enhance or alter unfavorable characteristics of the coating. The mechanical and structural properties of the (Fe-Al) intermetallic layer formed during HDA are influenced by alloying molten aluminum baths. It is well-known that aluminum has a high tendency towards iron and leads to the formation of Fe-Al. The formation and growth of the intermetallic (IM) is governed by the kinetic properties between aluminum and iron, which depend on factors such as crystal structure and solid solution solubility. Despite several attempts over the years, stabilizing the intermetallic structure has proven challenging. Researchers have explored adding a third element or more to stabilize the intermetallic structure, with studies focusing heavily on the effects of (Si) as an alloying element in the molten bath on the intermetallic layer. The initial effect of Si is the flattening of the intermetallic interface towards the substrate, rather than the typical tongue/finger-like shape [74-78], the Al_2O_3 is seen as more compact. Another approach has been made by varying the Si content from (1-10) wt. % [75] The results clearly indicate that the amount of Si significantly impacts reducing the thickness of the IM layer when combined with a minimal dipping time and aluminizing temperature. Notably, a mere 0.05% of vanadium (V) was introduced into the molten aluminum bath [76]. The presence of V served as an effective barrier to prevent any further reactions between Al and Fe within the molten bath. As a result, this led to a significant reduction in the thickness of the intermetallic layer, causing the Fe_2Al_5 to become thinner. Due to the brittle nature of Fe_2Al_5, which leads to the formation of voids and cracks in the intermetallic layer, it was imperative to find a viable alternative. Therefore, a decisive effort was made to procure a sound phase such as Fe3Al and FeAl. To achieve this, a molten bath was meticulously prepared using a mixture of 90% Al, 6% Fe, 3% Si, and 1% other essential elements [77]. After structural examinations it was revealed that the whole texture consists of Fe_3Al and FeAl.

Modeling is another manner to study the effects of an alloying element on the structure of the intermetallic layer. The study conducted by M. V. Akdeniz and A. 0. Mekhrabov [78,79]. The study conducted analyzed the effect of the alloying element on the formation and growth of Fe-Al. The influence of elements on the intermetallic is predicted based on the interfacial

interaction potentials using the statistical-thermodynamic theory of multicomponent alloys combined with electronic theory in the pseudopotential approximation. The elements were divided into two groups based on their effects on the activity of Al atoms in α-Fe0.95 $(Al_{1-n}X_n)_{0.05}$, where X represents elements (Si, Ti, Ge, Sb, Mg, Cu, Ca, Ag, Cd, Cr, Co, Zn, Mn, Ni, Pb, or Bi). Group one (XI) includes elements that retard the formation and growth of the intermetallic, ultimately decreasing the Al coefficient activity, which reduces the thickness of the intermetallic layer. The elements in this group are Si, Ti, Ge, Sb, Mg, Cu, Ca, Ag, Cd, and Cr. Group two (XII) shows less influence compared to group one, and the elements in this group, including Co, Zn, Mn, Ni, Pb, and Bi, are less effective in altering the activity of Al atoms towards Fe and forming the Fe-Al intermetallic. Consequently, the growth of such intermetallic will continues, increasing the intermetallic layer's thickness. Alloying the molten bath significantly impacts the structure of the intermetallic layer and may even alter the mechanical properties of the intermetallics. This effect cannot be ignored [70] using a mixture of Al, 6.9% Si, and 1.4% Mg in a molten bath with varying dipping times resulted in microhardness values of approximately 400 HV for the intermetallics zone, which is significantly lower than that of a pure aluminum bath. To improve results, it is recommended to add approximately 5 wt.% Cr to the molten bath [79] The coating's scratch resistance has been significantly improved through enhancement. It has been discovered that the introduction of alloying elements does not impact the structure and mechanical properties. Additionally, it has been found that the addition of elements also aids in enhancing the corrosion resistance of the aluminized parts. The Mg [80] in the molten bath shows sacrificial properties that improved the corrosion resistance of steel about six times comparable with galvanized steel in the sacrificial property.

To summarize, incorporating alloying elements into a molten aluminum bath during the hot-dip aluminizing process delivers significant advantages that enhance the quality, durability, and overall performance of coated products. The selection of alloying elements is based on their properties and desired outcomes, which may involve improving corrosion resistance, enhancing mechanical strength, increasing adhesion, and even tailoring aesthetic characteristics. By carefully introducing these elements into the molten aluminum bath, the resulting aluminized coatings exhibit superior resistance to harsh environments, including high temperatures, aggressive chemicals, and atmospheric corrosion. This is particularly valuable in industries such as automotive, construction, and aerospace, where materials face challenging conditions.

Furthermore, alloying elements can foster the formation of intermetallic compounds at the coating-substrate interface, promoting strong adhesion and preventing the potential for delamination or peeling over time. As a result, the coating's longevity is ensured, and its protective properties are maintained throughout the service life of the coated product.

2.7.5 Precoat before dipping

The precoating process involves applying an interlayer on a metal substrate before immersion into an aluminum bath. Efforts to enhance the intermetallic layer are underway through the implementation of a new interlayer to be deposited on the substrate's surface prior to aluminizing, utilizing techniques such as electroplating, electroless plating, PVD, CVD, etc. Incorporating an interlayer between the substrate and the aluminizing process will yield numerous benefits that enhance the intermetallics layer. Ultimately, this will have a significant impact on the performance of the coating, making it a robust protection layer for structural materials in harsh environments. It's worth noting that nickel (Ni) has been employed as an interlayer [81]; the results indicate that the performance of aluminized carbon steel with Ni interlayer has been significantly enhanced, by as much as five times, in harsh environments such as hot exposure and salt mixture under static load. It is also worth noting that Ni has a significant impact on the periodic oxidation resistance [82] of aluminized milled steel, to prevent carburization on the steel substrate, a protective interlayer comprising Ni and Re was employed [83] The interlayer results demonstrate a compelling barrier layer in contrast to the diffusion of carbon.

To enhance the coating ability of dual-phase steel during galvanization, interlayers have been employed along with a flash coating of Cu and Cu-Sn [84]. Aluminizing copper as a substrate may require this method to achieve proper adherence between aluminum and copper [85]. The cerium (Ce) is used as an interlayer on the Ni-base alloy [86] The Ce acts as a strong barrier that effectively retards the formation of Al_xCr_y intermetallic by strictly limiting the upward diffusion of Cr. Simultaneously, during annealing at high temperatures, it allows for Ni to diffuse out and form the much more stable β-NiAl phase. This process should not be undermined, as it is crucial for achieving optimal results.

2.7.6 Influence of substrate’s composition (carbon content)

When it comes to hot-dip aluminizing, the success and effectiveness of the process depend on more than just the properties of the aluminum bath and process parameters. The carbon content of the iron-base substrate material is also a crucial factor that plays a pivotal role. The presence or absence of carbon and its concentration in the substrate metal can result in significant variations in the behavior of the coating process and properties of the final aluminized product. The interaction between the substrate's carbon content and the molten aluminum bath can lead to various outcomes, which can impact the coating's adhesion, microstructure, and overall performance. Therefore, to optimize the process and tailor the characteristics of the coated products to specific applications, it is essential to understand the effects of substrate carbon content on hot-dip aluminizing.

As long as the hot-dip aluminizing process is conducted for relatively pure iron base substrates, such as unalloyed low carbon steels, and solely with pure aluminum free from any other common contaminating elements, such as iron and silicon, at low concentration levels afterward, the chemical and phase composition of the intermetallics' interlayer will correspond

well to those appearing in the equilibrium phase diagram of iron and aluminum. This primarily includes the Fe_2Al_5 grains exhibiting a robust [001] texture along the growth direction [87].

Others have studied the impact of carbon presence in the substrate [92-94] and thoroughly evaluated the impact of the iron diffusion outward to the molten bath, as well as the appearance and layer thickness of the structure. It has been duly reported [88] that the increase in the substrate steel's carbon content could prevent the iron (Fe) from diffusing.

The diffusivity of iron into the molten aluminum is significantly impacted by the carbon content present in the carbon steel. This is because the ferrite is more prone to diffuse out, rather than pearlite, Hwang et al. [91] where the research findings unequivocally demonstrate that the thickness of the coating layer exhibits a notable decline as the carbon content increases. A consequential decrease in the diffusion rate further accompanies this decline. The study meticulously analyzed carbon steel with varying carbon content, ranging from 0.2 to 1.1 wt.%.

2.7.7 Influence of heat treatment after HDA

The post-treatment step of diffusion heat treatment significantly impacts the properties and performance of coated materials following the hot-dip aluminizing process. It is crucial to optimize the microstructure and properties of the aluminized coating. The interplay between the substrate material, the aluminum coating, and the heat treatment conditions yields a range of benefits that enhance the coated product's durability, mechanical strength, and overall functionality.

The heat treatment process significantly influences the microstructure of the aluminized coating. It induces the growth and transformation of different phases within the coating, including the formation of protective aluminum oxide layers. These layers augment the coating's resistance to oxidation and corrosion, rendering it ideal for use in harsh environments. Moreover, heat treatment can refine the substrate and coating's grain structure, yielding superior mechanical properties such as toughness and hardness. However, it is crucial to note that improper or excessive heat treatment can lead to undesirable outcomes like excessive intermetallic compound growth, increased brittleness, or even coating delamination. Therefore, it is imperative to have a comprehensive understanding of the material's behavior during heat treatment to strike a balance between enhanced properties and potential drawbacks.

An approach has been made to control the formation of an intermetallic compound layer by diffusion treatment Kobayashi and Yakou [92] It has been observed that the formation of Fe_2Al_5, which has a brittle structure, primarily occurs at diffusion temperatures between 600 °C to 650 °C. On the other hand, intermetallic compounds of FeAl and Fe_3Al are formed at diffusion temperatures higher than 1000 °C, exhibiting relative oxidation resistance and high fracture compared to the Fe_2Al_5 intermetallic. Another approach by Y. Yürektürk and M. Baydoğan [93] where the HDA process was conducted on an SSF ductile iron, followed by austenitizing at 750 °C for 2 h and austempering at 330 °C for 1 h. The outcomes reveal that

the intermetallic compounds layer has transformed to Fe_2Al_5 + $FeAl_2$, FeAl, and α-Fe with Al_2O_3 scale on the surface after austempering, whereas the coating layer consists of topcoat aluminum and intermetallic compounds of Fe_2Al_5 and $FeAl_3$ in the HDA samples without any heat treatment. Based on the results of the room temperature tensile tests, it was determined that the HDA samples without any heat treatment do not significantly affect the mechanical properties of as-cast ductile iron. In mutual contrast to decreasing the strength, the ductility increased. After employing the austempering, the wear resistance increased by about 30% compared to non-treated HDA samples.

It is imperative to note that heat treatment is essential in the hot-dip aluminizing process to tailor the aluminized coating's characteristics to meet specific application requirements. Heat treatment significantly adds value to the coated materials by promoting diffusion, modifying microstructures, and enhancing mechanical properties, making them more resilient and versatile for a wide range of industrial applications.

2.7.8 Limitation in hot-dip aluminizing process

It is imperative that researchers and practitioners are aware of the limitations and challenges that come with the hot-dip aluminizing method for coating. While this technique may have advantages in certain aspects, it is important to note that it also has several key limitations:

1. **Limited substrate compatibility:** Hot-dip aluminizing is primarily utilized for steel and iron substrates, with its suitability for other materials, including non-ferrous metals or complex alloys, potentially restricted by variations in reactivity, diffusion rates, and formation of intermetallic compounds.
2. **Temperature sensitivity:** Attaining necessary diffusion and reaction rates requires extremely high temperatures during the process. This poses a problem for substrates with low melting points and materials sensitive to high temperatures, which can lead to potential distortions or degradation.
3. **Thickness control:** Achieving precise control over the coating thickness with hot-dip aluminizing can be challenging. It is important to note that thicker coatings may require longer immersion times, significantly increasing the risk of substrate damage or distortion.
4. **Intermetallic formation:** Excessive or undesirable intermetallic phases during the process can result in brittle coatings or reduced adhesion between the coating and substrate, despite intermetallic compound formation being a crucial aspect of the process.
5. **Uneven coating:** Uneven coating distribution is common with complex shapes or parts featuring intricate geometries. As a result, the coating thickness and properties across the substrate may vary significantly.

6. **Alloy composition optimization:** Identifying the optimal composition of aluminum alloy is crucial for achieving desired properties. Balancing corrosion resistance, mechanical properties, and other attributes can be challenging.
7. **Surface preparation requirements:** Effective surface preparation is crucial for successful hot-dip aluminizing. Any contaminants, oxides, or residual coatings can have a detrimental effect on the quality of the coating. It is essential to ensure that the surface is properly cleaned and free from any impurities before proceeding with the coating process. Failure to do so will compromise the adhesion of the coating, resulting in an inferior product.
8. **Limited alloy options:** The range of properties that can be achieved through hot-dip aluminizing is limited by the availability and compatibility of suitable aluminum alloys.
9. **Environmental concerns:** High temperatures and molten metals used in the process can lead to harmful emissions and waste. Environmental considerations and proper waste management are imperative and must be addressed.
10. **Post-treatment challenges:** It is imperative to note that certain applications may necessitate supplemental procedures subsequent to hot-dip aluminizing, such as sealing or extra coatings. The compatibility of coatings and adhesion between layers can present daunting obstacles.

Although hot-dip aluminizing has its limitations, it remains an invaluable coating technique due to its unique advantages. Implementing this method requires meticulous attention to the intended application's limitations, potential challenges, and specific requirements. Extensive research and engineering efforts are constantly underway to overcome these limitations and devise optimal strategies for various materials and applications.

2.8 Research aims and objectives

The study of the hot-dip aluminizing carbon steel C45 coating process aims to comprehensively explore a specialized surface treatment technique with significant potential. Hot-dip aluminizing immerses metal substrates in a molten aluminum alloy bath, forming a protective layer that offers unique advantages, including increased corrosion resistance, and improved oxidation resistance.

The primary research aim is to thoroughly investigate and comprehend the fundamental mechanisms and characteristics of the hot-dip aluminizing process. This requires a detailed exploration of the interactions between the molten aluminum (commercially pure) and the metal substrate (carbon steel C45), a thorough understanding of the formation of intermetallic compounds, and a comprehensive analysis of the resulting microstructure and its impact on material properties involving oxidation/corrosion properties. The research seeks to gain a deeper comprehension of these underlying mechanisms to provide valuable insights into characterizing the process parameters for achieving coatings with tailored properties.

To achieve the primary objective, the research has set the following objectives:

1. **Microstructural analysis:** The primary goal of this study is to utilize cutting-edge microscopy methods, including scanning electron microscopy (SEM) and glow discharge optical emission spectroscopy (GDOES), to thoroughly examine the microstructure of the coatings. The research aims to reveal the morphology of intermetallic phases that are created between aluminum and the substrate material, as well as their distribution and potential impact on coating properties.
2. **Corrosion and oxidation resistance:** The study aims to assess the effectiveness of hot-dip aluminized carbon steel C45 coatings in resisting corrosion and oxidation under relevant environmental conditions. Various methods were employed, such as high-temperature oxidation studies at different temperatures and exposure periods, cyclic exposure at high temperatures, and immersion in molten salts, to determine the protective capabilities of the coatings.
3. **Kinetic growth of the intermetallic layer:** An additional aim is to utilize a computational technique that imitates the kinetics of intermetallic compound development while performing the hot-dip aluminizing process on carbon steel C45 precoat with copper. These models are crucial in predicting coating properties and comprehending the diffusion and reaction kinetics' function.

To summarize, the research on hot-dip aluminizing carbon steel C45 has a clear purpose: to advance the understanding of this specialized coating technique and its potential applications. The objectives are comprehensive, covering every aspect from process parameters to corrosion resistance. The aim is to make a significant contribution to the field of materials science and engineering by providing valuable insights into optimizing hot-dip aluminizing for enhanced material performance. This research is not only important but also necessary for the advancement of this field.

2.8.1 Knowledge gap

The research on hot-dip aluminizing carbon steel identifies numerous significant knowledge gaps within the existing body of literature. These gaps must be addressed to enhance our understanding of the process and its implications. It is imperative to investigate further to fill these knowledge gaps and comprehensively comprehend the hot-dip aluminizing technique and its potential applications. Some of the key knowledge gaps include:

1. **Microstructure-property relationships:** It is imperative to note that despite previous research on the microstructural changes during hot-dip aluminizing, there still needs to be a significant gap in understanding the direct impact of these variations on the corrosion and oxidation properties of coated material It is crucial to establish clear correlations between microstructure and performance to optimize specific application

processes. Not doing it properly may result in less than optimal results and hinder progress in the field.

2. **Intermetallic compound formation kinetics:** A complete understanding of the kinetics involved in forming intermetallic compounds between the aluminum coating and substrate material is imperative. Investigating the factors that have an impact is imperative these are compounds' growth rates, composition, and distribution to effectively predict and manage coating properties.
3. **Long-term durability:** It is imperative to conduct long-term durability studies on hot-dip aluminized coatings that incorporate real-world exposure conditions in order to accurately evaluate their practical utility. While these coatings' short-term corrosion and oxidation resistance have been examined, it is crucial to understand their performance over extended periods and under varying environments and temperatures.
4. **Effect of interlayer:** Further investigation is required to determine the influence of interlayer between aluminum and substrate material on the overall performance of hot-dip aluminized coatings. It should be noted that different interlayer elements can significantly impact properties such as grain refinement, growth mechanism, morphology of the intermetallic layer, and corrosion resistance.

Addressing these knowledge gaps is absolutely crucial to improving our understanding of the hot-dip aluminizing process and optimizing it for various practical applications. This research might fill these gaps to contribute to the development of innovative coating solutions that offer tailored performance benefits to a wide range of industries and applications.

2.8.2 Scientific goals

The study of hot-dip aluminizing carbon steel C45 aims to advance our fundamental understanding of this specialized coating process and its underlying mechanisms and develop more effective and optimized coating solutions. This objective encompasses a range of goals that seek to uncover the intricate details of the process, characterize the resulting coatings, and leverage this knowledge to enhance material properties for multiple applications.

In order to conduct effective scientific research on a system, it is crucial to have clear scientific goals in mind. The following goals are typically pursued in such research, as they are fundamental to advancing our understanding and knowledge of the system at hand.

1. **Mechanistic insights:** Researchers must investigate the fundamental mechanisms governing the intermetallic compound formation and the interaction between the aluminum coating and the substrate material during hot-dip aluminizing. It is imperative to understand the kinetics, diffusion pathways, and reactions involved to elucidate the processes that shape the resulting microstructure and properties of the coatings.

2. **Microstructural understanding:** It is imperative that a thorough comprehension of the microstructural evolution within hot-dip aluminized coatings is achieved. The characterization of the morphology, composition, and distribution of intermetallic phases formed at the coating-substrate interface and throughout the coating's thickness is essential for establishing a correlation between microstructure and performance attributes.
3. **Property-structure relationships:** Establishing unequivocal connections between microstructural features and the mechanical, corrosion, and oxidation properties of hot-dip aluminized coatings is imperative. Researchers must quantify the influence of various microstructural characteristics on different performance metrics to steer the design of coatings with customized properties.
4. **Optimization strategies:** Developing systematic strategies to optimize the hot-dip aluminizing process for specific applications is imperative. A thorough investigation of the influence of process parameters, including temperature, immersion time, and aluminum alloy composition or interlayer, is necessary to identify conditions that yield coatings with desired attributes.
5. **Functional tailoring:** Examine potential avenues for customizing the features of hot-dip aluminized coatings to suit particular purposes and uses. Thoroughly scrutinize how modifying alloy composition, coating thickness, and microstructure can be intentionally utilized to amplify resistance to corrosion and high-temperature resilience.

The attainment of these scientific objectives is crucial for researchers as they strive to make the field of materials science and engineering receive noteworthy contributions. Their primary focus is to advance the comprehension of surface coatings, intermetallic reactions, and material behavior at elevated temperatures. The investigations have provided valuable knowledge and insights that will serve as the basis for designing superior coatings, optimizing industrial processes, and developing materials with exceptional performance capabilities that can be applied across various industries and applications.

CHAPTER 3: Structural characterization of hot-dip aluminized carbon steel C45

3.1 Structure features of HDA carbon steel C45 aluminized with commercially pure aluminum

3.1.1 Experiments and methodologies

3.1.1.1 Hot-dip aluminizing laboratory set-up

The equipment and instruments required for hot-dip aluminizing coating processes have been meticulously prepared at the University of Miskolc workshops/ Faculty of Material and Chemical Engineering, as depicted in Figure 15(a). The workplace has been set up with all the necessary tools and equipment to ensure a flawless coating process. The setup includes an electrical furnace type, a graphite crucible for the molten aluminum, and a thermocouple K-type to measure the instance temperature at the dipping time, all of which are shown in Figure 15(b).

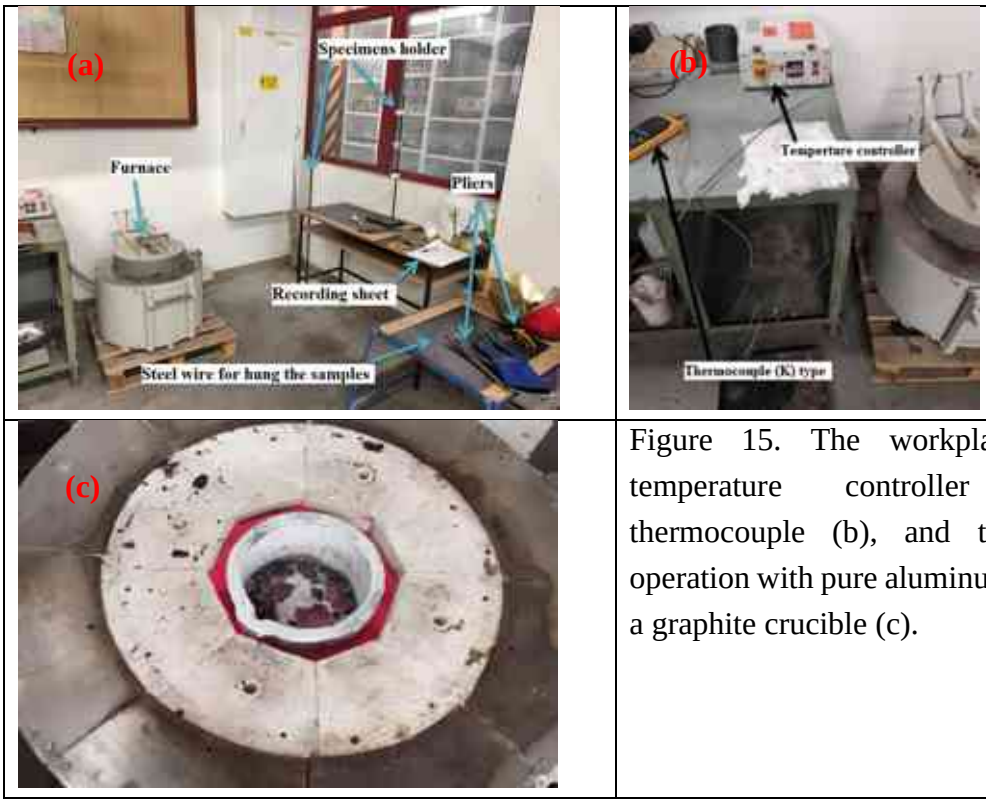

Figure 15. The workplace setup (a), temperature controller unit and thermocouple (b), and the furnace in operation with pure aluminum melted inside a graphite crucible (c).

The schematic representation of the HDA (Hot Dip Aluminizing) process, which was performed in a laboratory setting, has been presented to delineate the procedure adopted for aluminizing the carbon steel C45, Figure 16.

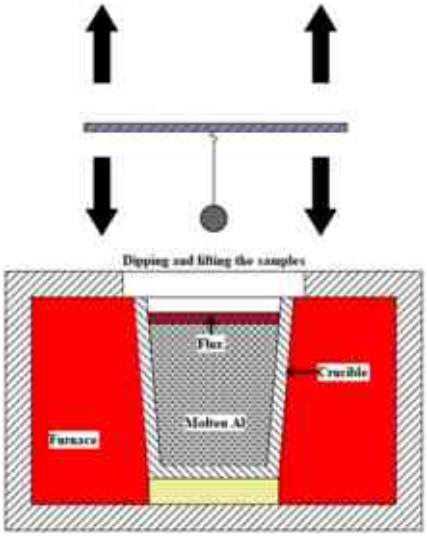

Figure 16. The schematic process illustrates the way conducted to HDA carbon steel C45 specimens.

The aluminizing process was carried out at a constant temperature of 800°C initially. Subsequently, with a modified fluxing salt mixture, the temperature was lowered to approximately 700°C. The cooling process was performed under normal air conditions.

3.1.1.2 Materials and sample preparation

For this research, carbon steel C45 EN10083 cold drawn rods from STALMA in Poland were chosen for their abundance, high mechanical properties, and cost-effectiveness. This material may also be a viable alternative for structural use in challenging environments with appropriate coating or aluminizing.

The chemical composition of carbon steel C45 can be found in Table 1. The disc sample with A section of the rod was cut with a diameter measuring 32 mm and a thickness of 5 mm, as depicted in Figure 17. Using a grinding machine, the samples were ground with SiC emery paper (220, 320, 500, 800) and then polished with a diamond wax stick applicator DP-stitch P, 3 µm from Struers ApS®. DP-lubricants were utilized in conjunction with MD-Mol, a 200 mm woven wool MD-Mol™, to ensure appropriate cooling and lubrication of the material surface. The surface was then washed with distilled water, followed by ethanol, and dried. Finally, the specimens were soaked in alcohol (ethanol) before usage.

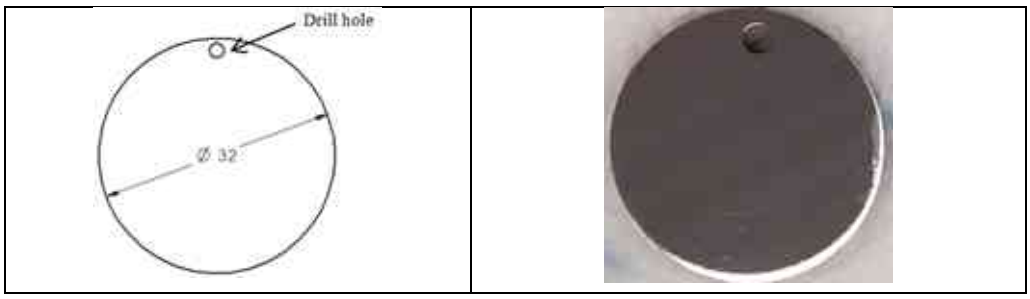

(a)Drawing sketch of the sample.	(b) carbon steel C45 after the grinding, polishing, and cleaning stage.
Figure 17. Carbon steel C45 sample showing dimensions and shape details.	

The type of molten aluminum bath utilized in this study is commercially pure aluminum, and its chemical compositions are presented in Table 1.

Table 1. Constituting major chemical elements of steel C45 specimens and the commercial aluminum bath used in the laboratory HDA experiments

C45 steel elementary composition (obtained by spectroscopic analysis), wt%									
C	Mn	Si	Cu	Ni	Cr	Mo	S	P	Fe
0.44	0.52	0.18	0.22	0.09	0.08	0.02	0.03	0.01	Rest
Aluminum melt elementary composition (obtained by spectroscopic analysis), wt%									
Fe	Mn	Si	Cu	Zn	Ti	Ni	Ga	Mg	Al
0.92	0.55	0.12	0.08	0.18	0.05	0.02	0.06	0.01	Rest

Salt mixtures containing (KCl + NaCl + 4% CaF_2) were utilized as a flux layer over the molten aluminum. It was observed through thermogravimetric analysis measurements that the melting point of the salt mixture was lower than that of aluminum

3.1.1.3 Investigation methods

The investigation of the structure features was primarily carried out through the application of metallographic analysis techniques. A Zeiss Evo MA10 scanning electron microscope (SEM) equipped with an energy dispersive spectrometer (EDS) and a Thermo Scientific Helios G4 PFIB CXe type of SEM combined with EDS using a lanthanum hexaboride (LaB6) emitter were utilized to analyze the structures of cross-sections. For further evaluation of the PFIB SEM images, Orientation Imaging Microscopic (OIM) software was used to analyze each phase's grain size and fraction distribution. An optical microscopic ZEISS Axioscope was used to reveal the structural changes. Further, glow discharge optical emission spectroscopy (GD-OES) GD-profile 2^{TM} from HORIBA was applied to show the distribution profile of the elements developed in the topcoat layer and interdiffusion zone during hot-dipping, it is noteworthy to mention that metallographic techniques were employed throughout all sections of the study.

3.1.2 Results and discussions

3.1.2.1 Carbon steel C45 as substrate metal

Carbon steel C45 grade will be an appropriate choice for structural steel in harsh environments with high temperatures and corrosive media, as long as it is coated with aluminizing. Its strength and durability make it the ideal material for such extreme conditions.

The structure of unalloyed carbon steel C45 is depicted in Figure 18. The colony structure of pearlite is shown adjacent to the ferrite structure, occupying about 50 percent of the area

determined by the ImageJ software estimation. Thus, this type of steel falls within the hyper-eutectoid region of the iron-carbon phase diagram, with an initial ferrite and pearlite structure at room temperature. Most of the steel's carbon content is present as cementite phase.

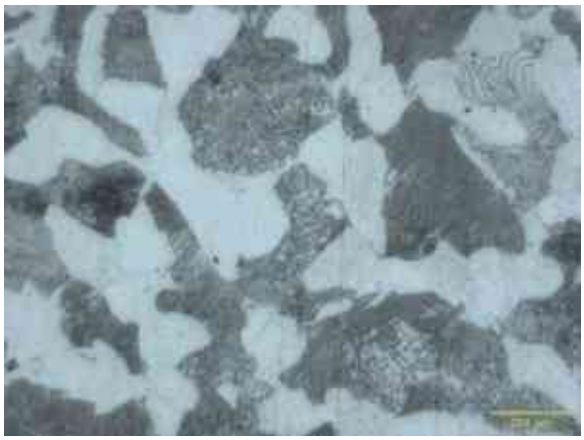

Figure 18. Optical microscopic image for steel C45 before HDA, the photo was taken perpendicular to the extrusion direction, revealing the distribution of pearlite colonies structure (dark) together with ferrite (white color).

3.1.2.2 Structure characteristics of HDA carbon steel C45

The aluminized samples always showed a layered structure, as is seen in the optical microscopic image in Figure 19. The structure of the aluminized C45 steel specimens exhibits three distinct layers in their cross sections: an aluminum top layer, an intermetallic layer, and a steel substrate. In Figure 19, the form of the intermetallics grown toward the substrate seems to show a tongue or a finger-like structure, which is consistent with studies done by others [89], [94-96]. Fe–Al intermetallics also appear to be found in the topcoat layer and are spread as needle-like (acicular) crystals see Figure 20. Voids, gaps, and cracks can also be observed, resulting from inclusions incorporated from the molten bath and the intermetallic layer's inherent brittleness Figure 20. Moreover, some small broken fractions even fell out during the saw machine's sectioning of the aluminized sample.

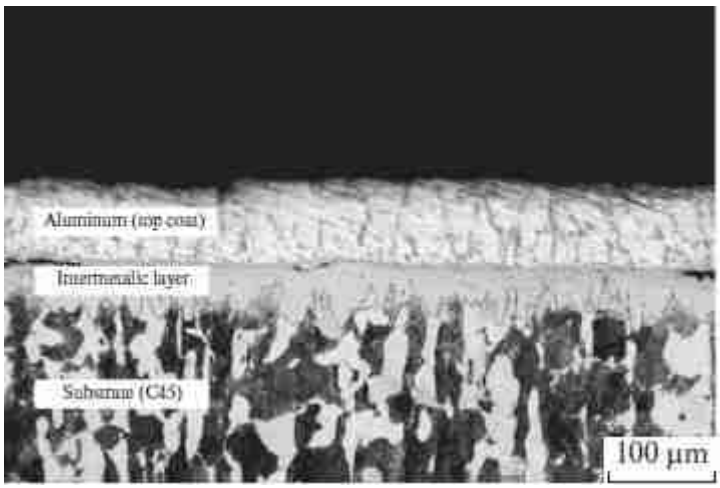

Figure 19. Optical microscopic image of microstructure of aluminized C45 highlighting grains of ferrite (white) and perlite (black) of the steel substrate.

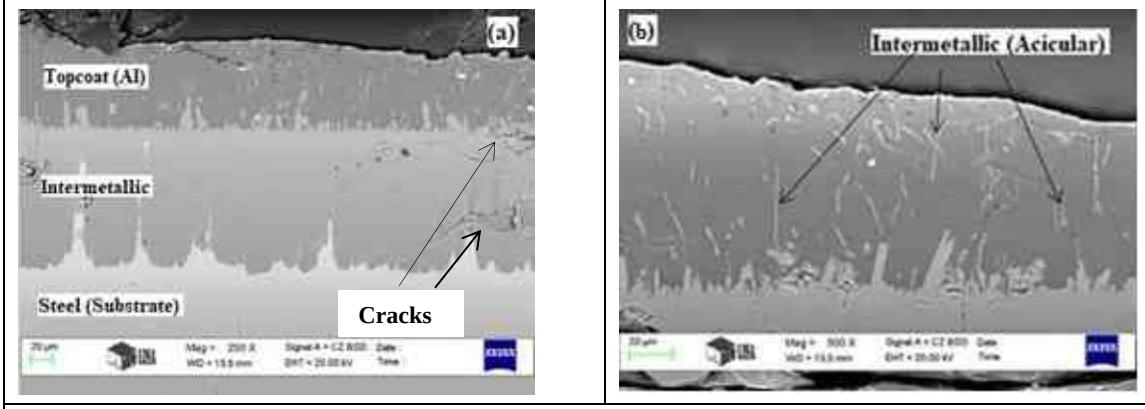

Figure 20. Top of the carbon steel C45 substrate with two distinct layers (a), traces of intermetallic phases in topcoat (Al) (b), for aluminizing temperature around 800 °C and dipping time 2.5 min.

3.1.2.3 Phase constituents and characteristics

The findings displayed in Figure 21 depict a comprehensive overview of the phases of Fe-Al intermetallics. These were formed due to the physical and chemical interactions between the liquid aluminum and solid iron base alloy C45 during the HDA experiment. The experiment was conducted at a temperature of 695 ± 5°C and with a dipping duration of 2.5 minutes. Figure 21(a) clearly shows that several minor-volume phases are slightly intermixed. However, two more uniformly formed intermetallics of Fe_4Al_{13} (blue colored) and Fe_2Al_5 (in yellow) can be observed between the top aluminum coat (in red) and the substrate steel (shown as ferrite in the phase mapping part in Figure 21(a)). Of the selected cross-section area shown in Figure 21(a), the largest portion of the EBSD mapping is metallic aluminum, occupying about 47%. The single-phase Fe_2Al_5 is also present in the Al top layer, making up a total of 23%. The sum of areas of the other three intermetallics (Fe_2Al_5, $FeAl_3$, and FeAl) is somewhat less than that of Fe_4Al_{13} (also seen in Figure 21(c)).

The needle-like phase Fe_4Al_{13}, which is relatively large, is found in the solidified Al top layer and verifies the significant dissolution and diffusion of iron into the liquid aluminum. This could induce crystallization and precipitation of aluminum-rich solid phases of Fe_4Al_{13}.

To reveal more details about their structures at their interfaces, a small area at the interface of the two dominant intermetallic phases of Fe_4Al_{13} and Fe_2Al_5 was also investigated by the EBSD phase mapping technique (Figure 21(b)). Percentage fractions of the identified phases are shown in Figure 21(d). The OIM software was used to calculate the grain size distribution values based on the input data shown in Figure 22(a) and presented in Figure 22(b). As evident from the figure, Fe_2Al_5 has a larger grain size compared to the other phases. The average grain size of Fe_2Al_5 is approximately 1.8 μm Std. around 0.38, while the Fe_4Al_{13} and FeAl phases have an average grain size of around 0.43 μm Std. around 0.075. The smallest grain size was

found for the $FeAl_3$ phase, which is finely dispersed mainly at the grain boundaries of the larger grains of Fe_4Al_{13} and Fe_2Al_5.

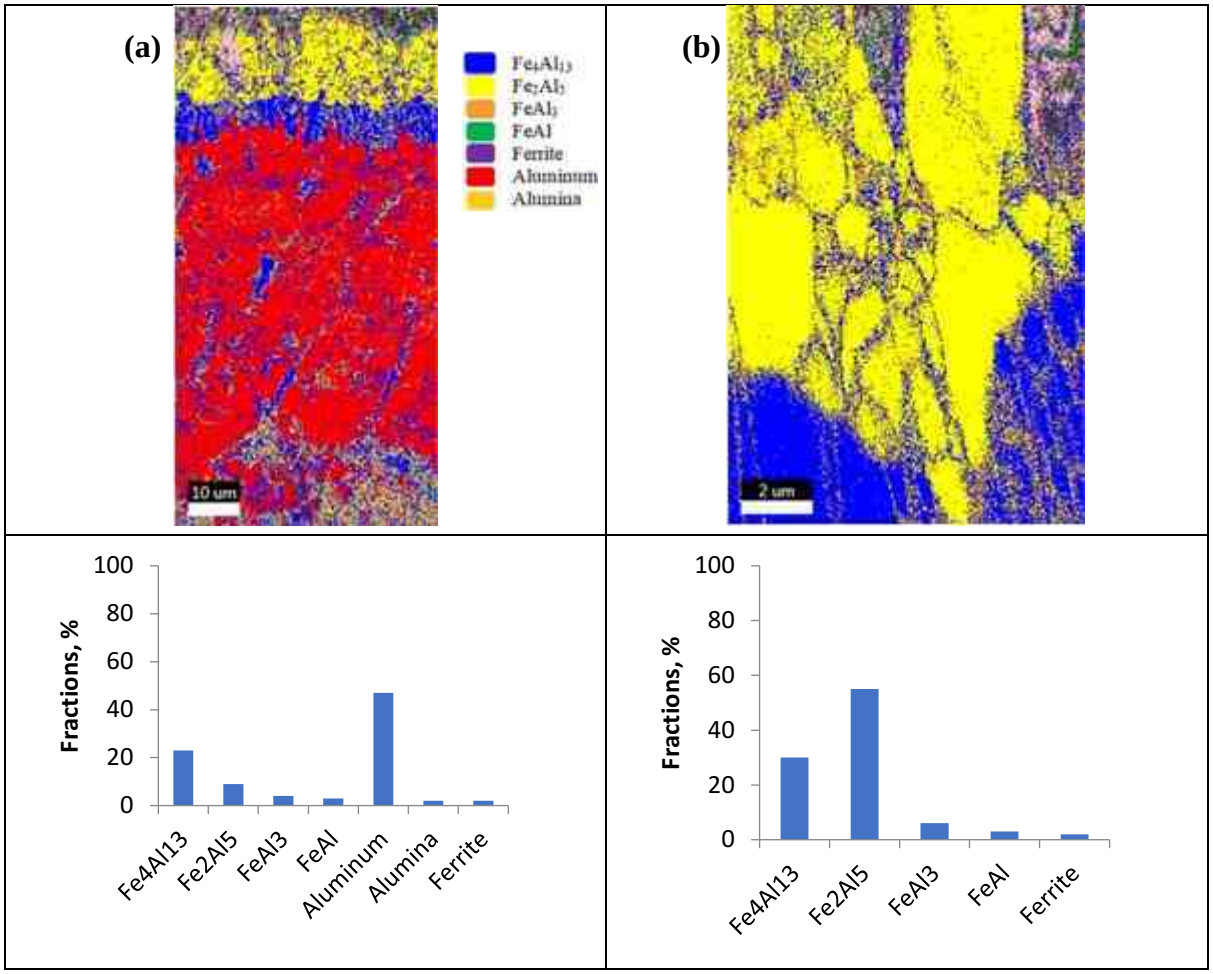

Figure 21. (a) Full cross-sectional EBSD phase mapping, showing different phases evolved during HDA of carbon steel C45. (b) The selected small area in the interface region reveals the phases formed during HDA. (c) Percentage fractions of phases identified in the investigated cross-section (a) of the HDA carbon steel C45. (d) Percentage fractions of phases identified in the investigated cross-section shown in (b) of the HAD carbon steel C45.

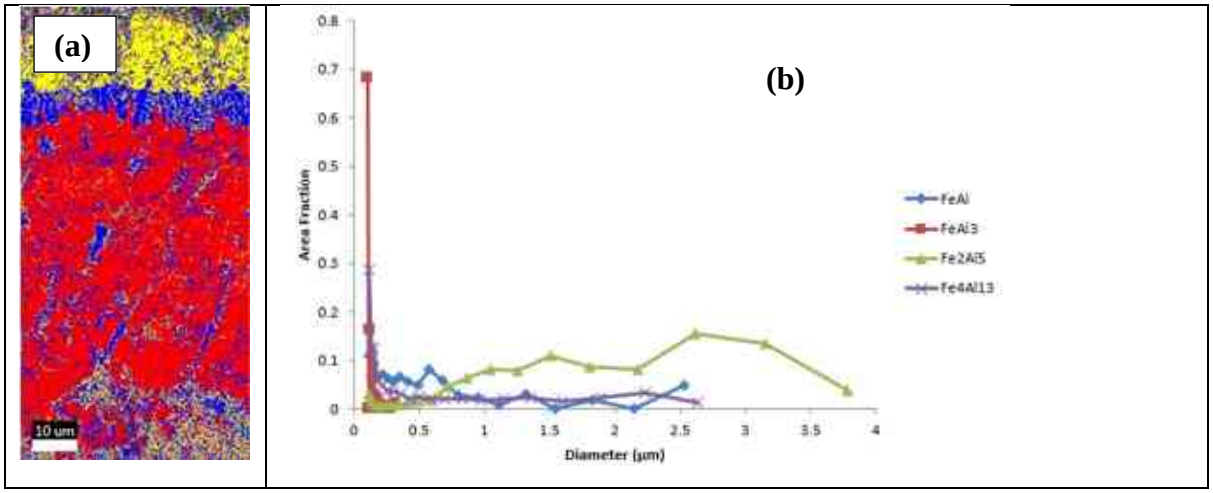

Figure 22. Phase map where the diameter size of grain has been determined (a), area fractions of the intermetallics grains versus their measured diameter size (b).

Figure 23 depicts inverse pole Figures for each intermetallic phase with their orientation direction; the Fe_2Al_5 and Fe_4Al_{13} are grown preferentially in normal direction [001], which is consistent with previous observation [97, 98] Both have the same orthorhombic structure with a slight difference in lattice distance parameters shown in Table 2. The c-lattice parameter of the orthorhombic structure in Fe_4Al_{13} is longer than that of Fe_2Al_5, which means the vacancy sites increase, which might be considered a reason for the development of such an aluminum-rich phase Fe_4Al_{13}. The differences in crystal orientation in the FeAl phase that can be seen in the pole Figure do not show any preferred growth direction, and the same is true for $FeAl_3$. All the phases that are formed in the HDA carbon steel C45 coating have different crystal structures with preferential lattice parameters in each.

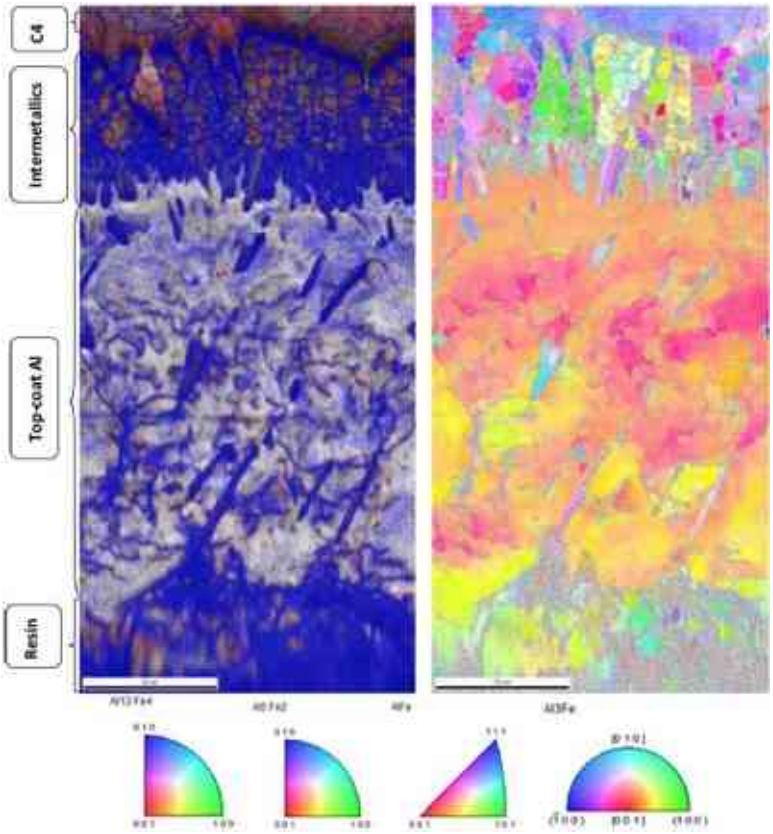

Figure 23. In (a) shows the image quality map, and (b) shows the Inverse pole Figure map of the Fe–Al phases formed during HDA carbon steel C45.

Figures 24 and 25 display the results of both line scan EDS and GD-OES measurements. The outermost layer shows high aluminum peaks that decrease towards the steel substrate. The EDS line scan results of Fe–Al are shown in Figure 24. The scan starts from the topcoat layer and goes down to the steel substrate on a cross-sectioned HDA sample, with 0.1 μm steps. The graph indicates that the aluminum-rich zone in the Fe–Al system starts within the range of aluminum content between 90 and 55 atomic percent, representing the two significant phases detected within the intermetallic area. The SEM image in Figure 21(a) shows this as different colors. The aluminum content in the Fe_2Al_5 phase ranges between 65 and 75 atomic percentages, while for Fe_4Al_{13}, it is above 75 atomic percent.

Before the GD-OES analysis, the aluminum top layer was removed by grinding with SiC particles to produce a smooth primary surface (Ra = 0.1 μm). This was done to ensure a more even removal of the sample material from the crater bottom during the Ar^+ ion sputtering. The high Si and C atomic percentages at the top few micrometers originate from the embedded SiC grinding material. As the sputtered area was quite large, about 12.5 mm^2, the intensities of the detected elements found in depth can be viewed as some average values in the function of the crater depth going inward deep into the substrate steel. This is shown in Figure 26(a).

In contrast, during an EDS line analysis (Figure 24), measurements were performed along a skinny band on the sample's cross-section. This is the main reason for seeing a sharp step-like profile for the Al and Fe concentrations in Figure 25(a). The GD-OES technique observed a slightly sloping intensity curve for the same two elements, as shown in Figure 25(a). Nevertheless, the GD-OES analysis revealed some interesting additional features about the distribution of the minor elements like carbon, manganese, silicon, and nickel (Figure 25(b)), indicating their involvement in developing the final microstructure of the HDA-treated C45 steel.

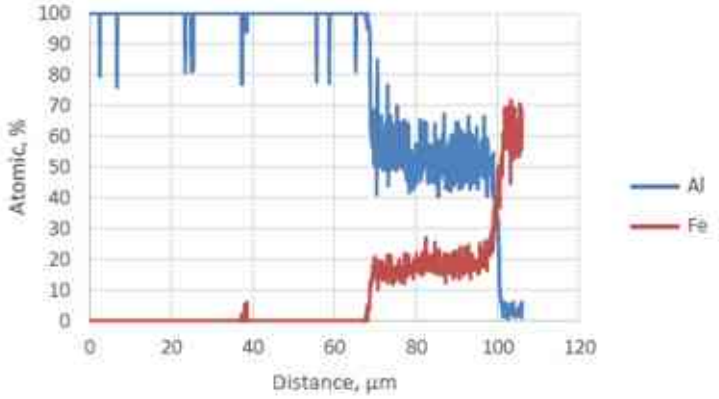

Figure 24. EDS line scan on a cross-section of HDA carbon steel C45.

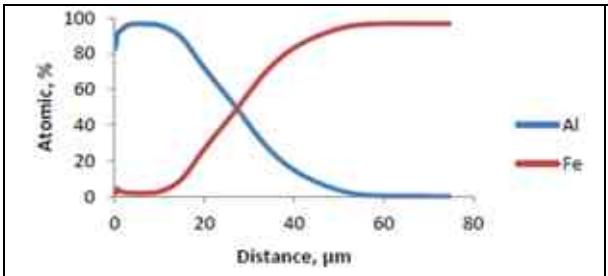

Figure 25(a) GD-OES profile measurement through the Fe-Al intermetallics layers.

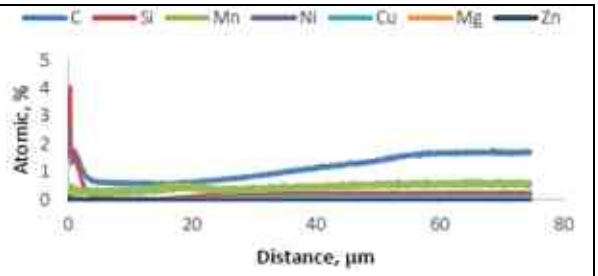

Figure 25(b) GD-OES profile measurement of the minor elements within the zone of intermetallics formed during the HDA experiment with pure commercial aluminum.

Lattice parameters for the different Fe–Al compounds had been determined previously, and the results were stored in the PFIB-EBSD databases. In addition, the crystal structures and lattice parameters for coatings and IM phases found in carbon steel C45 samples aluminized by hot dipping were also added to our database, given in Table 2.

Table 2. The crystal structure for each phase with their lattice parameters.

IM phase	Crystal structure	Lattice parameters	
Al	Cubic	a= 4.04 A°	α= 90°
		b=4.04 A°	β= 90°
		c=4.04 A°	γ= 90°
Al_2O_3	Trigonal	a=4.76 A°	α= 90°
		b=4.76 A°	β= 90°
		c=12.99 A°	γ= 120°
Fe_2Al_5	Orthorhombic	a= 7.66 A°	α= 90°
		b=6.42 A°	β= 90°
		c=4.22 A°	γ= 90°
Fe_4Al_{13}	Orthorhombic	a= 7.75 A°	α= 90°
		b=4.03 A°	β= 90°
		c=23.77 A°	γ= 90°
$FeAl_3$	Monoclinic	a= 15.49 A°	α= 90°
		b=8.08 A°	β= 107.7°
		c=12.48 A°	γ= 90°
FeAl	Cubic	a= 2.91 A°	α= 90°
		b=2.91 A°	β= 90°
		c=2.91 A°	γ= 90°

The standard formation Gibbs energies see Figure 26, were also calculated in the relevant temperature range up to 1000°C using the HSC software version 9.5. The results revealed that the highest negative values characterize the Fe_2Al_5 phase, e.g., $\Delta G° = -197.6$ kJ/ mol) at 700°C which temperature was the one where the C45 steel samples were dipped in the molten aluminum bath; hence, this Fe_2Al_5 phase must have formed preferentially under such circumstances.

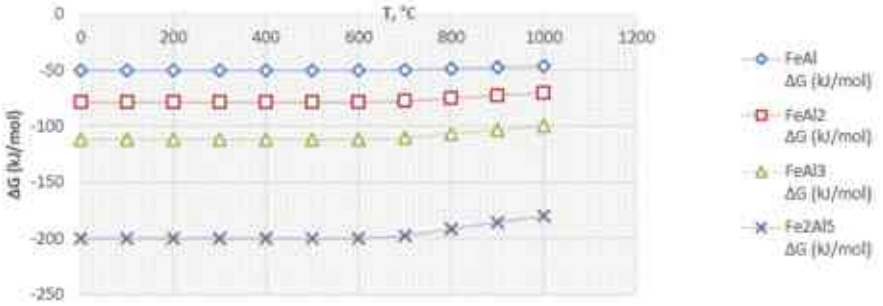

Figure 26. Standard Gibbs molar formation energies of the given four iron aluminides were calculated by the HSC-software version 9.5.

3.1.2.4 Effect of aluminizing temperature and dipping time

As the temperature of the aluminizing process increases, there is a corresponding increase in the thickness of both the intermetallic and topcoat aluminum layers. This relationship is directly proportional, as illustrated in Figure 27 (a)&(b) were kept with the same dipping time of 2.5 min. Therefore, higher aluminizing temperatures result in thicker intermetallic and topcoat layers. After conducting experiments on carbon steel C45, it was discovered that aluminizing the samples at 800°C resulted in an intermetallic thickness of approximately 47 µm at the lower root of the finger. The maximum thickness recorded was approximately 105 µm. The HDA performed at a temperature of 700°C revealed a minimum thickness of 33 µm and a maximum

thickness of 43 µm Figure 27 (b). These findings provide valuable insights into the behavior of carbon steel C45 under different aluminizing temperatures.

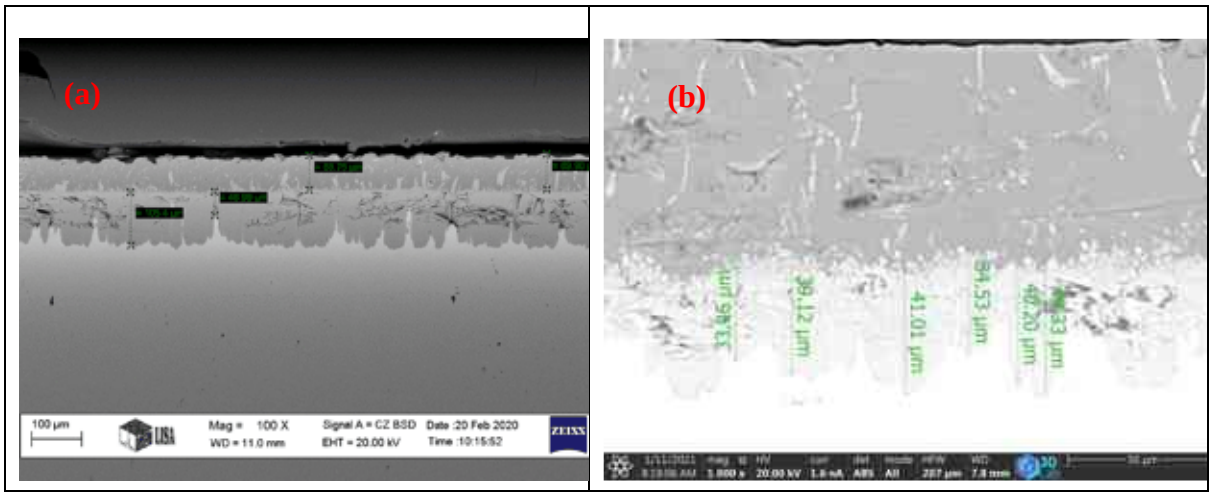

Figure 27. HDA carbon steel C45 aluminized specimen at 800 °C (a), and HDA carbon steel C45 aluminized at around 700 °C specimen (b).

In a mere 2.5 minutes of dip time, a formidable intermetallic layer with a rough thickness of around 105 µm was formed, as illustrated in Figure 28(a). Moreover, extending the dipping period by just one minute led to a remarkable increase in intermetallic thickness. In Figure 29(b), the thickness was measured to be approximately 129 µm, showing a difference of 20 µm. These findings highlight the incredible efficiency and potential of this process. The thickness of the intermetallic was found to be about 129 µm Figure 28(b), with a difference of around 20 µm.

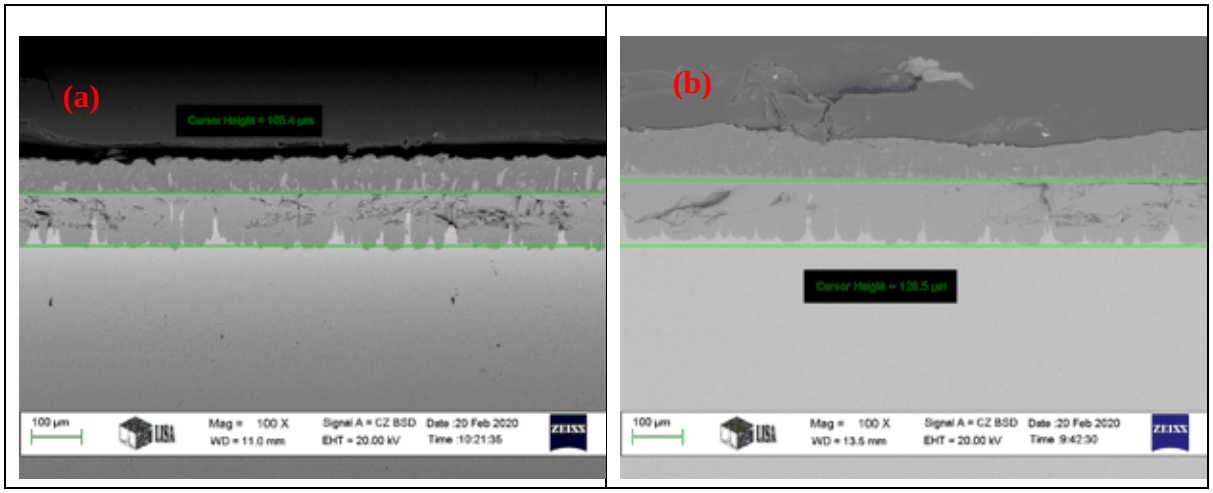

Figure 28. The HDA carbon steel C4 cross-section views were dipped for 150 s (a) and 210 s (b).

3.1.2.5 The role of carbon content in coating structure development

The structure of the hot-dip aluminized carbon steel C45 is shown in Figure 29, wherein the cross-section of the SEM image clearly shows three different layers. The topcoat consists of

solidified aluminum followed by the intermetallic layer formed at the interface of solid carbon steel C45 and molten aluminum during the HDA process.

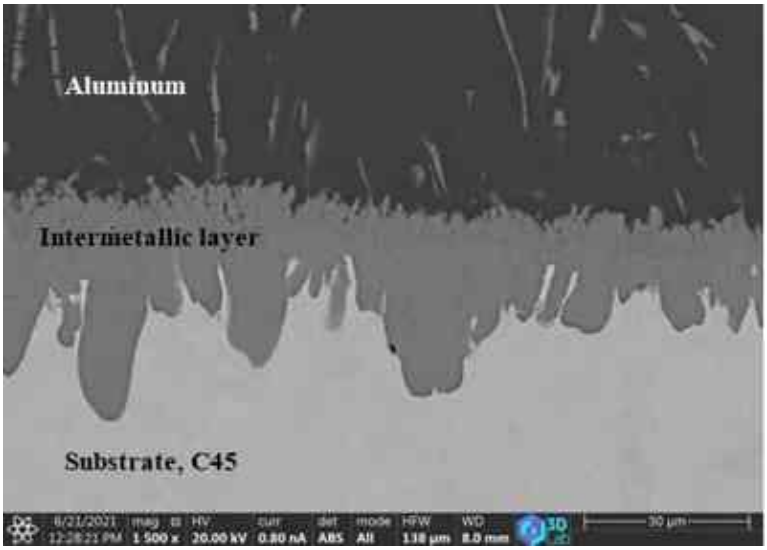

Figure 29. The PFIB-SEM image shows the hot-dip aluminized unalloyed carbon steel C45 structure when the HDA process temperature was around 695 °C and immersion time was 2.5 minutes inside a molten bath.

Elemental mapping was conducted to demonstrate the distribution of elements in the interdiffusion zone and topcoat aluminum, as shown in Figure 30. The intermetallic layer exhibited significant accumulation of carbon and nickel, with traces of these elements also detected in the topcoat aluminum. Specifically, Figure 30 (E) and (F) depict the role of carbon and nickel, respectively, in the formation of the intermetallic structure layer. The high carbon content in the intermetallic layer also resulted in the formation of aluminum carbide, which was observed at the outermost layer along with pure aluminum. As the distribution of the two tested minor elements, i.e., carbon and nickel (See Figure 30 parts (E) and (F)), could not be detected with high enough resolution by the applied EDS mapping technique, so the GDOES light spectrometric analytical technique was also employed to try to detect these two minor elements in the surface layers, viz. there is a unique feature of GD OES spectrometry that the elemental in-depth distribution of the constituting chemical elements in principle can be analyzed from hydrogen through carbon to high atomic number ones. Provided the sample's initial surface is flat and smooth, the GD argon ion sputtering will continuously detach and excite the sample's constituting atoms from a relatively large spot/area of several dozen mm^2. In this way, the detected intensities for the analyzed elements will present a close-to-average level of concentration in the given layer versus sputtering time. In Figure 31, for example, there is a quite pure aluminum top layer sputtered away (i.e., atomized and removed) in about 800 s. While in the sputtering range of ~800 – 1900 s, both major elements of the zone/interlayer of the iron aluminum intermetallics could be well detected, followed by the sputtering of iron (from about 2000 s) inside of the C45 steel substrate. Moreover, the presence of carbon and

nickel could also be well detected in the zone of intermetallics (Figure 31), revealing the result of the outward diffusion of these two alloying elements of the substrate steel during the HDA process.

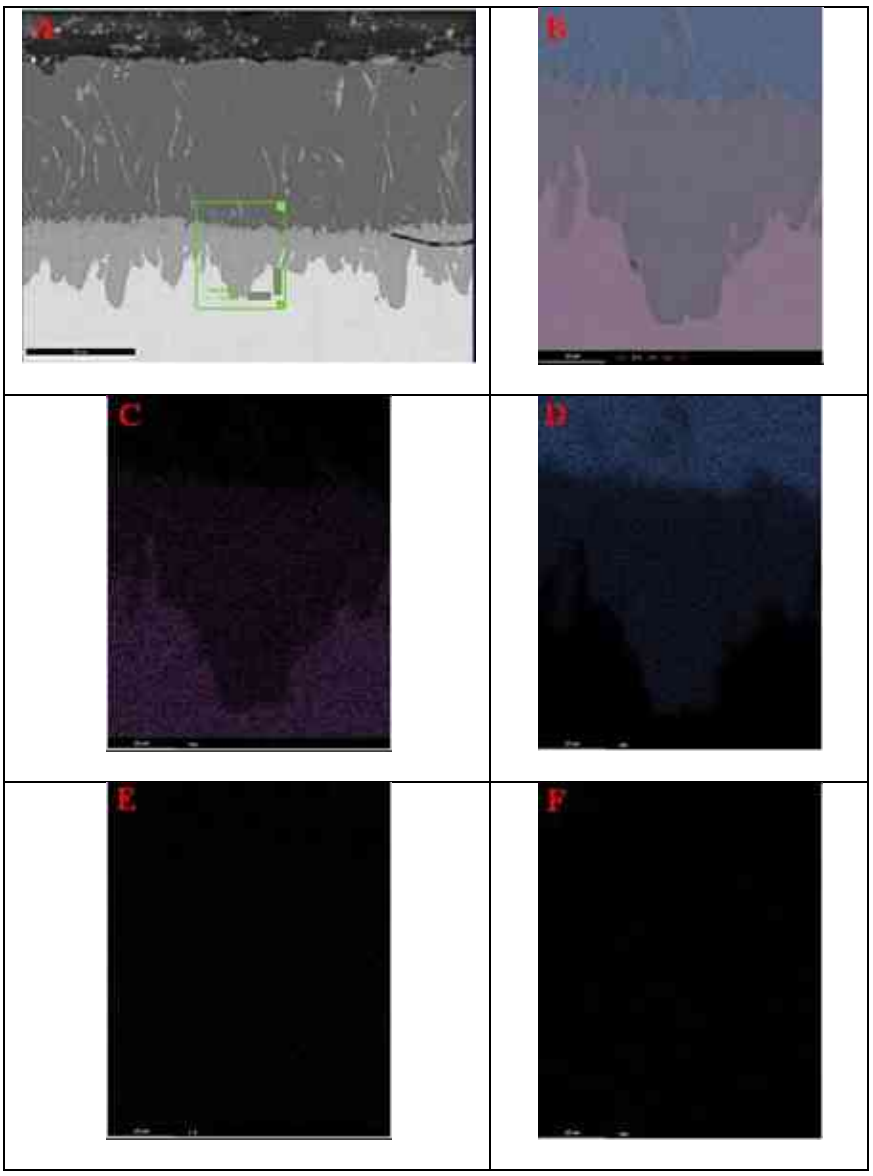

Figure 30. EDS elemental Mapping for the sectioned HDA sample showing the distribution of the elements within the intermetallic layer and outermost layer, (A) PFIB-SEM image shows the specified area where the elemental mapping was taken, (B) Overlay, (C) Fe, (D) Al, (E) C, (F) Ni.

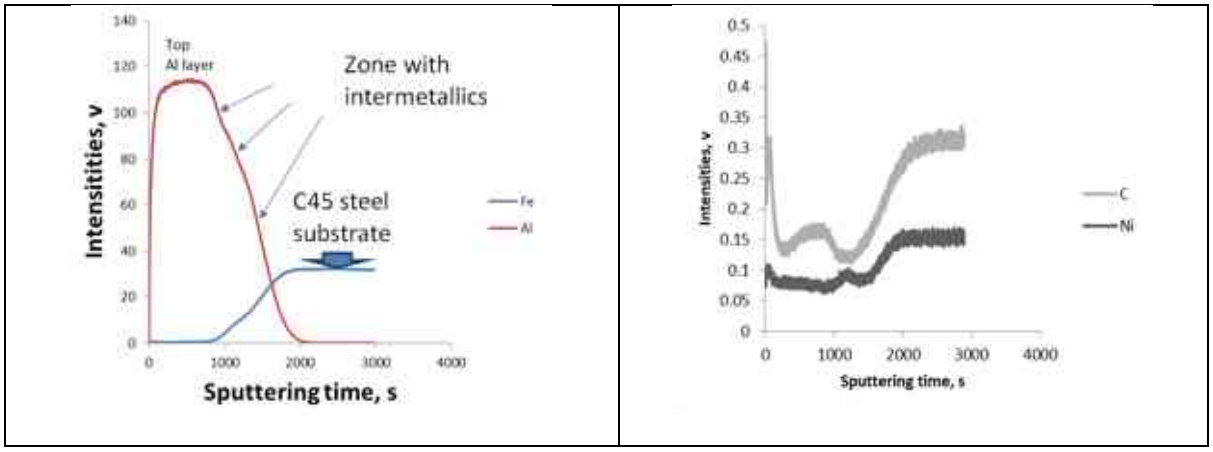

Figure 31. GD-OES profiles for Fe and Al, together with the two minor elements C and Ni vs. the argon ion sputtering time while forming a crater inwards the sample.

An EDS-line scan was also performed on the cross-sectioned HDA specimen shown in Figure 32. The scan with 0.1 µm steps was taken from the spot just beneath the upper portion of the outermost layer marked on the PFIB-SEM image (Figure 32), where the path of the line scan is also clearly indicated.

The results coincide well with the GD-OES in-depth elemental profiles (Figure 31), where high intensities of the sputtered minor elements carbon and nickel are apparent from about 70 µm in depth from the top. Carbon could also be detected in the Al topcoat layer, most probably forming aluminum carbides such as Al_4C_3 or Fe_3AlC within the interdiffusion zone [99]. The theory behind this phenomenon is attributed to the high chemical affinity of iron (Fe) toward aluminum (Al) (See the corresponding standard equilibrium thermochemical drawn in Figure 26), which results in the fast formation reaction and evolution of iron aluminides as a newly developing and growing surface layer. Both elements have different diffusivity within this solid surface layer, which might cause vacant places within the crystal lattice. As carbon has limited solubility in iron (Fe), it is gaining a higher driving force to diffuse outwards and re-occupy these vacant places (so-called vacancies) within the iron aluminide crystals. The effect of carbon presence in the substrate was studied by others [88-90] concisely to evaluate its impact on the structure appearance, layer thickness, and the diffusion of iron outward to the molten bath. It was also reported [88] that the increase of carbon content of the substrate steel could cease the iron (Fe) to diffuse out, and silicon and manganese would have the same role. However, the outward diffusion of carbon into the intermetallics layer and its role in forming the iron-aluminum layer and the topcoat layer's grains orientation and distribution are still ambiguous. The phase analysis results were employed via EBSD to identify the type of carbide formed; the outcomes reveal two types of carbides, Fe_3AlC and AlC, within the intermetallic layer and topcoat layer see Figure 33.

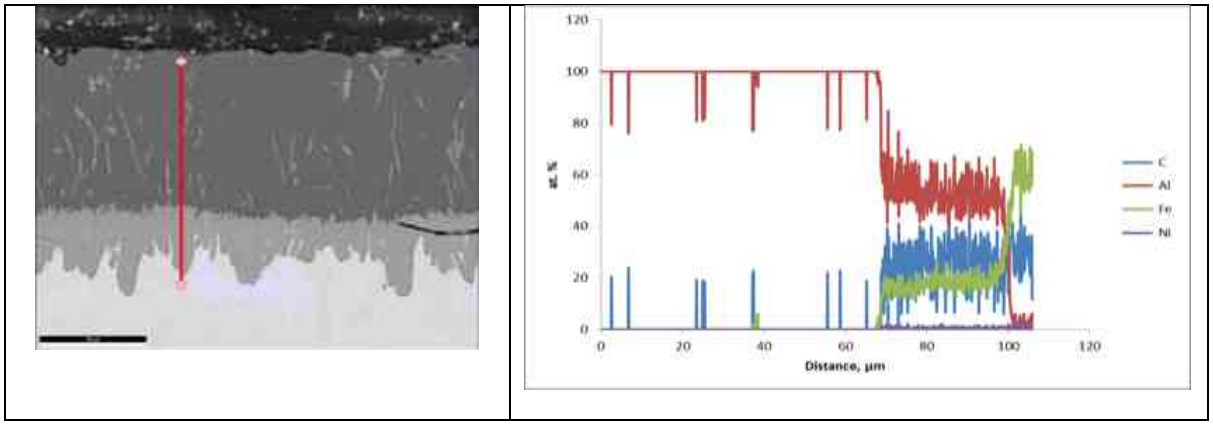

Figure 32. EDS line scan performed across the cross-section of the HDA sample also showing the atomic concentrations of aluminum, iron, carbon, and nickel elements vs. the measured distance inward down to the substrate steel C45.

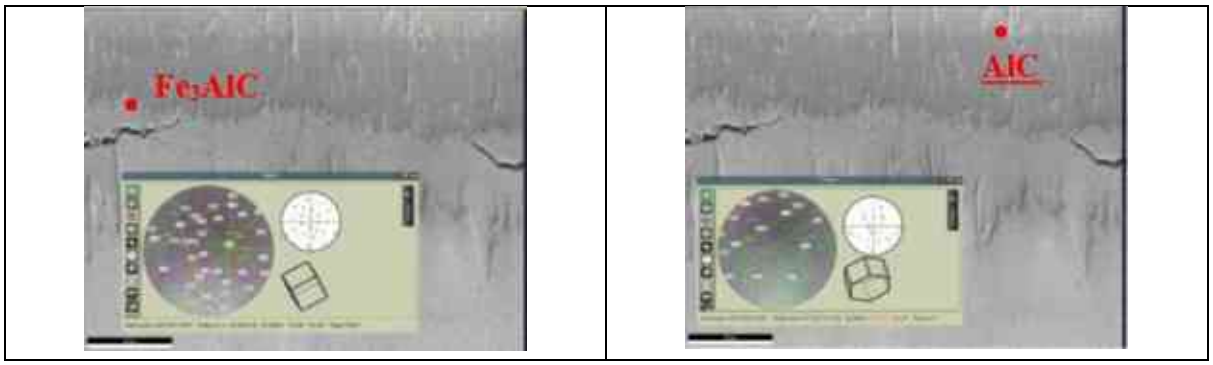

Figure 33. The EBSD spot analysis was examined to specify the type of formed phase during HDA.

The outcomes of all our laboratory tests are consistent with each other and in harmony with the relevant theories and the results of previous studies. During the HDA process, the carbon accumulates at the interface between the liquid aluminum and solid iron. It could also be detected in the topcoat aluminum, forming different carbides such as Fe_3AlC and AlC within the intermetallic layer and topcoat layer. Moreover, these phenomena might become critical when there is a strong requirement to avoid the carbon's presence within the topcoat and/or in the intermetallic layer due to any foreseeable severe corrosion attack when the HDA-coated sample is to be exposed to high-temperature environments. Hence, in such harsh environments, the increased tendency of the formation/precipitation of different carbides forming at the interdiffusion zone and topcoat layer might decrease the level of its protective nature.

3.1.2.6 Mechanical properties (Microhardness)

In order to better understand the behavior of the intermetallic, the mechanical properties of the HDA carbon steel C45 developed layers were thoroughly examined. The hardness measurement tester, Instron Tukon 2100B, was used to perform measurements on the cross-section of the HDA carbon steel C45, starting from the topcoat downward to the substrate (as shown in Figure 34). The results of the measurements revealed that the intermetallic zone,

particularly the finger-like structure, which represents the Fe_2Al_5 phase, had the highest level of hardness.

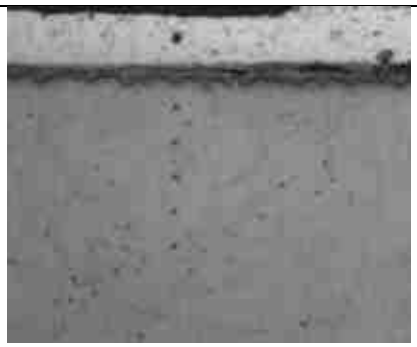

Figure 34(a). Image reference reveals the trace of hardness indenter.

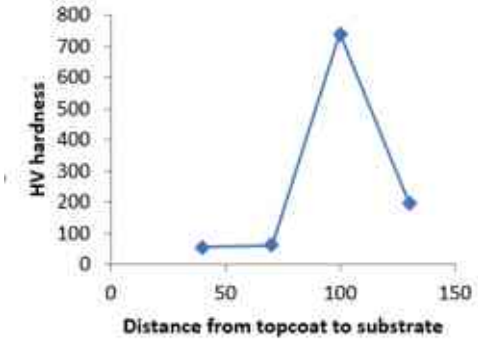

Figure 34(b). HV hardness measurement along the cross-section of HDA carbon steel C45.

3.2 Structural features of HDA carbon steel C45 pre-coated with copper

3.2.1 Experiments and methodologies

3.2.1.1 Materials and sample preparation

The materials used in this particular section are identical to those used in section 3.1 The specimens, which are featured in Figure 35, have dimensions of approximately 10x10x5 mm.

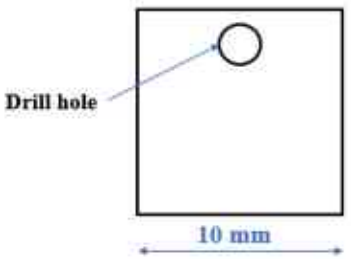

Figure 35. The carbon steel C45 sample shows the geometry and dimensions.

3.2.1.2 Copper deposition

Copper was electroplated onto carbon steel C45 specimens before HDA using a solution containing ($CuSO_4 \cdot 5H_2O$ + H_2SO_4) diluted in distilled water. After being degreased ultrasonically in an acetone bath for approximately 30 minutes, the specimens were cleaned with distilled water.

As shown in Figure 36, after the cell was set, the current density was adjusted to 1.8 $A.cm^{-2}$ with a constant voltage of 2 V and a constant duration of 3 minutes. Prior to electroplating, the specimens were activated using sulfuric acid for two minutes.

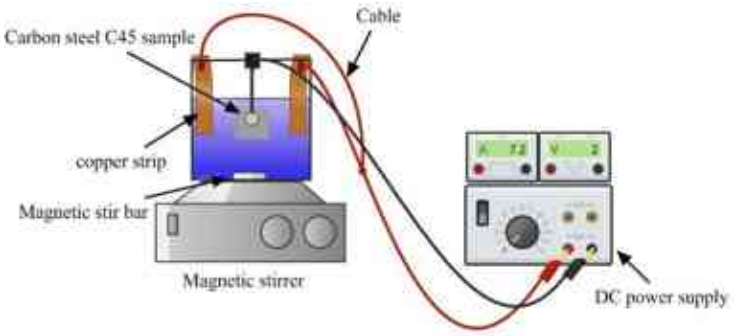

Figure 36. A schematic diagram shows the copper electroplating setup of carbon steel C45 specimens.

Upon electroplating copper onto carbon steel C45 specimens, heat treatment was carried out at 640 ± 10 ºC. In order to avoid any structural changes or transformation to the substrate, the temperature was below Ac1. Furthermore, to ensure that the deposited copper is compact and dense. The specimens were placed in a stainless steel tube inside an electric furnace under an Ar atmosphere.

3.2.1.3 HDA procedure

The aluminizing temperature was maintained constant throughout the experiment at around 700 ± 10 ºC, with a varied dipping time set at 45, 85, 150, and 300 s; then, the specimens were cooled in air.

The hot-dip aluminizing procedure is performed manually (herein, lifting and dipping). A molten flux consisting of salt mixtures of (CaF_2 + KCl + NaCl) was poured over molten aluminum; prior to dipping, the specimens were dipped in HCl solution for 5 to 10 s to ensure the removal of any oxide scale formed during the heat treatment and then rinsed in distilled water. The specimens were then covered with a solder flux paste type (EN 29454-1 1.1.2.C) to prevent contamination and improve wettability.

3.2.1.4 Intermetallic layer (IM) thickness measurement and growth kinetics

An open-source image processing software, namely ImageJ, has been used to measure the thickness of the intermetallic layers (IMs). In order to determine the average thickness of the total intermetallic layer and the thickness of each phase formed, a total of over 70 measurements were conducted for each distinguished layer based on colour contrast, and then the average measurement was computed see Figure (37).

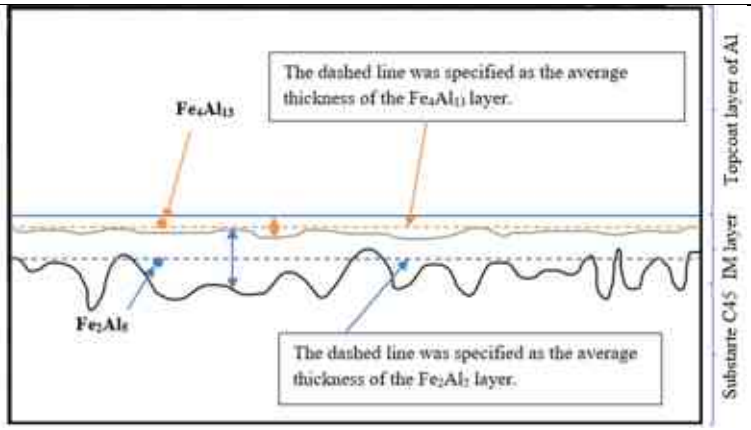

Figure 37. The scheme diagram displays the thickness measurements set up of the intermetallic layers.

3.2.2 Results and discussions

3.2.2.1 Surface morphology and structural characteristics of the electroplated copper carbon steel C45 before and after heat treatment.

As part of investigating the surface appearance and morphologies of copper electroplated carbon steel C45 specimens, elementary concentrations were determined before and after heat treatment. This is shown in Figure 38(a), which illustrates copper electroplated surface morphology. In addition, the surface's Cu, Fe, and O content was also measured with EDS-specified area analyzers for a sample size of approximately 10×10 μm. The outermost surface of the copper deposited has shown granular particles of copper adhered onto the substrate surface of carbon steel C45. The EDS analyzed copper concentration on the top was about 96.46 at. %, Fe 1.21 at.%, and O 2.33 at. %. The morphology after heat treatment partially starts to transform and displays a flatter appearance due to the coalescence of copper particles together, see Figure 38(b); granular particles with bigger sizes are also seen, the oxide layer developed on the surface, and the copper content was about 87.53 at. % and O 12.47 at. %, later the oxide was removed through pickling with HCl solution prior to aluminizing. The obtained thickness of deposited copper ranged from 20 to 25 μm.

The heat-treated copper-coated carbon steel C45 sample was ground and polished to examine the cross-sectional structure see Figure 39(a). It was possible to observe a few oxide spots at the interface. Figure 39(b) shows a closer view of the interface. At the interface, the substrate grain appears to be finer in size due to recrystallization. In the EDS spot analysis taken at position 2 μm beneath the interface see Figure 39(d), the copper diffused slightly into the substrate; it is difficult to detect a diffusion layer initiated at this temperature; copper diffusion is quite common at elevated temperatures [100] Further, the EDS map was also analyzed for the same area, and the results are consistent with common knowledge about the diffusion layer of copper into carbon steel, see Figure 39(c).

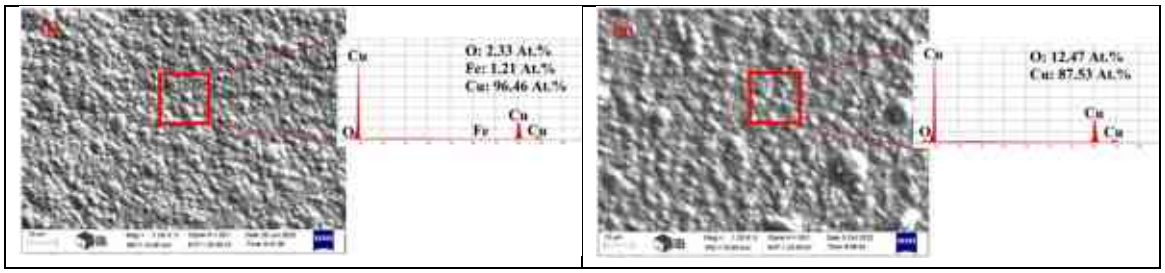

Figure 38. The SEM/ SE microscope images of the top surface of the copper coated carbon steel C45 depict the surface morphology as well as the EDS element analysis before (a) and after (b) heat treatment.

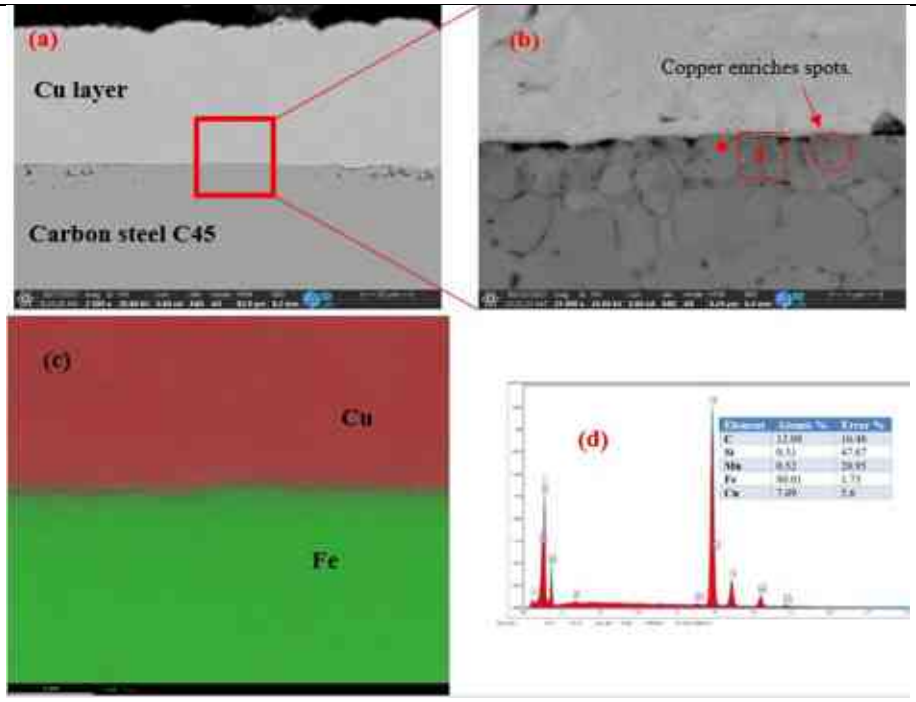

Figure 39. Cross-sectional view of electroplated copper on carbon steel C45 (a) and closer view at the interface (b) revealing the structure, (c) elemental map for the specified area, and (d) elemental spot analysis for spot number 1 in Figure 4(b).

3.2.2.2 Structure characteristics of HDA copper precoated carbon steel C45

The HDA carbon steel specimens were ground and polished for use in structural investigation. The cross-sectional view of each specimen dipped in molten aluminum at different times is shown in Figure 40 (a), (b), (c), and (d), respectively. Overall, the cross-sectional structures are similar, consisting of an aluminum topcoat layer at the top, solidified Fe-Al phases within the topcoat layer ranging in form from flake to acicular shapes, and an intermetallic layer in the middle, in addition to the substrate and its relevance with previous studies [34,35]. Two phases of the intermetallic layer can be distinguished by color contrast: light gray closer to the substrate and gray towards the topcoat layer. The EDS spot analysis on both layers has been conducted, and the results are tabulated in Table

3 (see Figure 40 for the identified number (1, 2)). Figure 40(a) shows that the structure of the sample dipped for 45 seconds shows consistent growth; even slightly, there are no indications of microcracks. In addition, no presence of copper could be observed within the intermetallic layer. However, its existence was confined to the topcoat layer of aluminum (see Figure 41), where it was trapped. With the dipping time of 85 seconds, as shown in Figure 40(b), the intermetallic layer's irregular growth finger-like morphology is observed with the initiation of microcracks. Copper could not be detected either in the intermetallic or topcoat layers. As the dipping time increases to 150 s, Figure 40(c), the irregular growth becomes dominant, and the intermetallic layer thickness increases. For a dipping time of 300 s, Figure 40(d), irregular growth becomes disorderly. Furthermore, copper was not detectable in either sample; cracks are clearly visible. The analysis of EDS spots involved measuring the percentage of two prominent species, Fe and Al, present in both layers for various dip durations. Table 3 displays the results, indicating that the presence of Al rises with longer duration periods. However, Fe content decreases slightly, implying that the interlayer suppresses the rapid inward and upward diffusion of species.

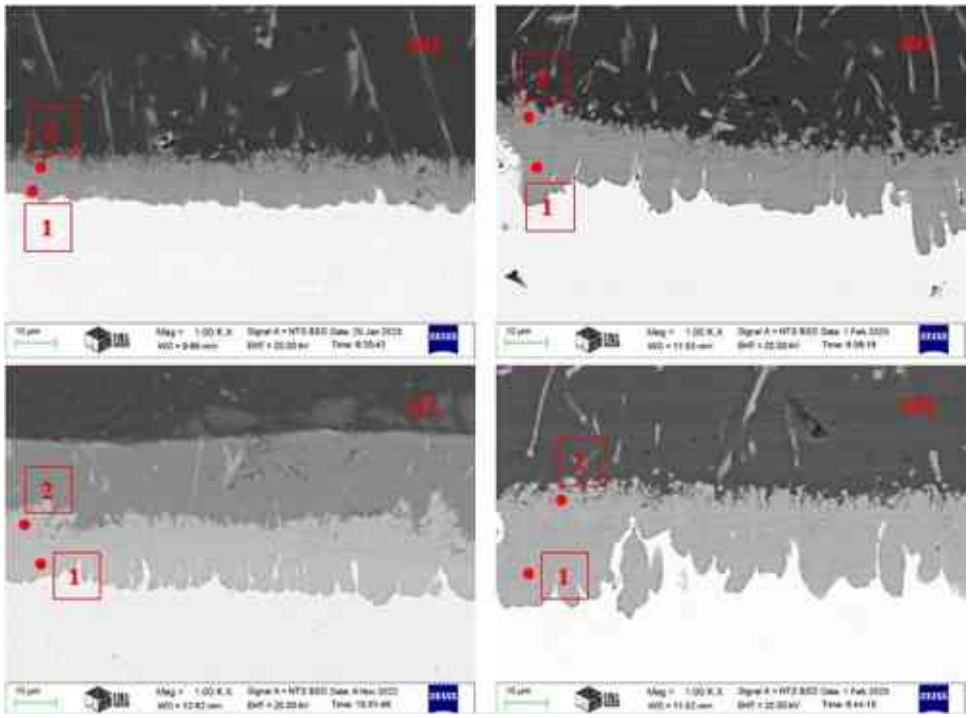

Figure 40. Cross-sectional view of HDA carbon steel C45 precoated with copper specimens were dipped in a molten aluminum bath for (a) 43 s, (b) 85 (c) 150 s, and (d) 300 s.

Table 3. The elemental concentration of Fe and Al in at. % within the intermetallic layer, which is composed of two phases; the identified spots were determined in Figure 40 (a), (b), (c), and (d) using an EDS spot analyzer.

Spot	(a)		Possible phase	(b)		Possible phase	(c)		Possible phase	(d)		Possible phase
	Fe	Al		Fe	Al		Fe	Al		Fe	Al	
(1)	26.84	73.16	Fe_2Al_5	26.3	73.70	Fe_2Al_5	25.81	74.19	Fe_2Al_5	25.46	74.54	Fe_2Al_5
(2)	23.08	76.92	Fe_4Al_{13}	22.88	77.12	Fe_4Al_{13}	21.83	78.17	Fe_4Al_{13}	21.10	78.90	Fe_4Al_{13}

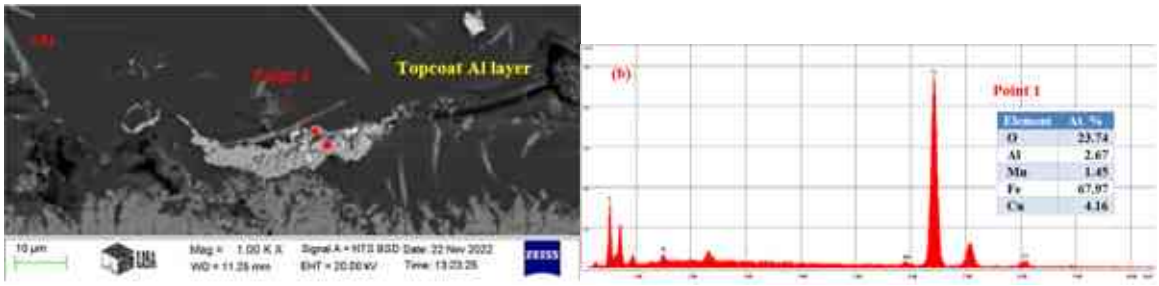

Figure 41. Cross-sectional view of HDA copper precoated C45 sample dipped for 43 s (a) and (b) EDS elemental spot analysis.

3.2.2.3 The intermetallic phase constituents

The EBSD was conducted on HDA carbon steel C45 pre-coated with copper samples to investigate phase-sorting within the intermetallic layer for two samples that were dipped for 45 s and 150 s, respectively. In both samples, there are two phases within the intermetallic layer: a phase of η-Fe_2Al_5 at the substrate interface and a phase of θ-Fe_4Al_{13} at the topcoat aluminum interface. The last phase at the substrate surface interfered with the θ-Fe_4Al_{13} as well. Figure 42(a), where an area around 30×30 µm has been captured for phase scanning, while in Figure 42(b), inverse pole figures show the different orientations of grains within the intermetallic layer for the captured area, the η-Fe_2Al_5 with preferentially oriented on [001] normal direction to the surface of the sample as reported elsewhere [16,17] having orthorhombic crystal structure while the θ-Fe_4Al_{13} has oriented on [001] parallel to the surface of the sample.

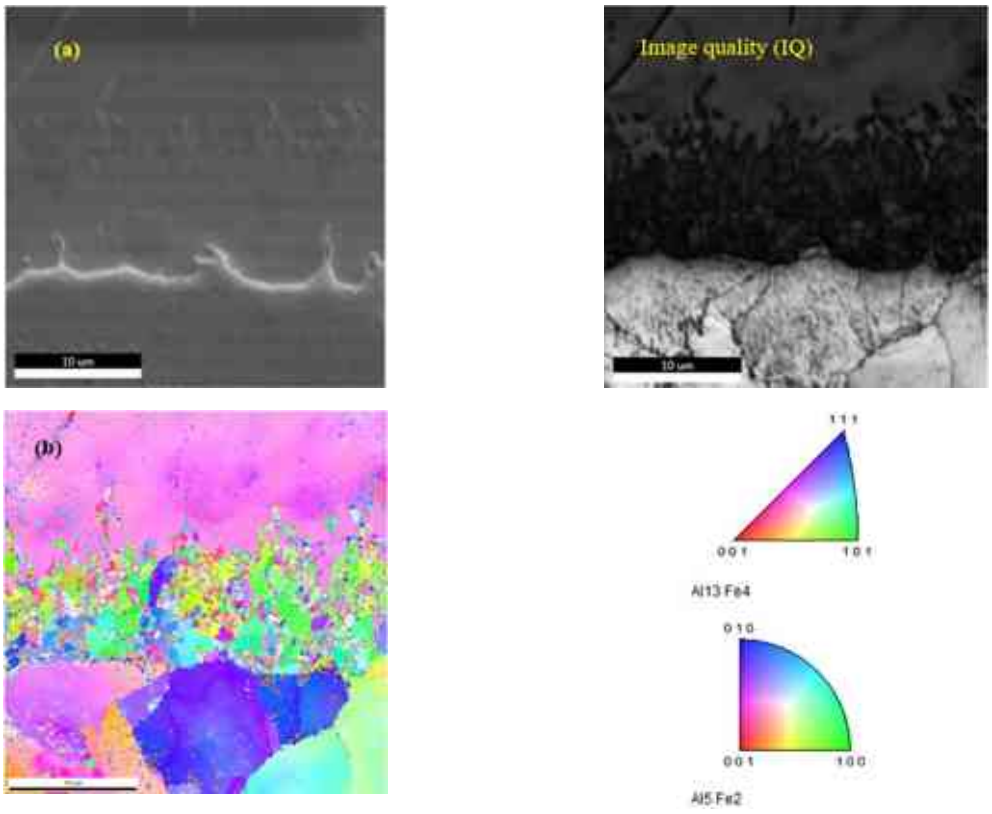

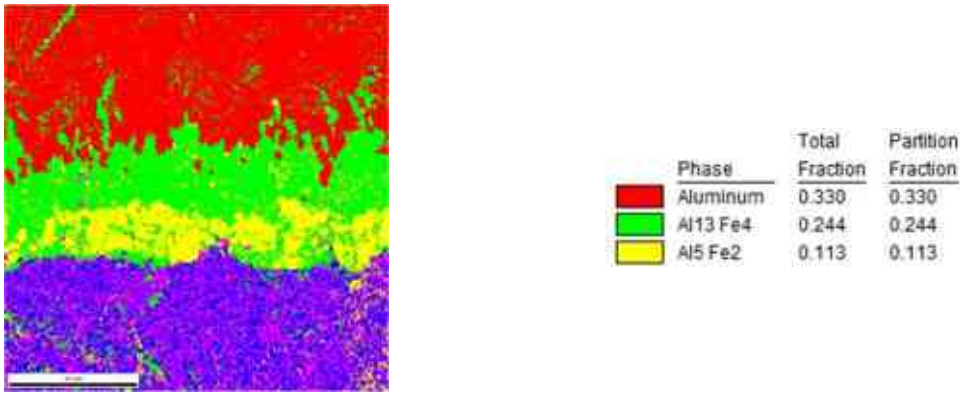

Figure 42. The SEM image where EBSD was conducted on (a) the inverse pole figure revealing different orientations of grains within the intermetallic layer and (c) the EBSD phase analysis.

After conducting an examination of grain evolution and size in both phases at two different dipping times, more attention has been given to these aspects. Figure 43 displays a sample dipped for 45 seconds, while Figure 44 shows a sample dipped for 150 seconds. To analyze the EBSD data, the TLS OIM analysis 8 software was utilized. Both phases show fine grains, as seen in Figures 43(a) and (b), with Fe_2Al_5 phase grains appearing slightly larger in Figure 43(a) compared to Fe_4Al_{13} grains. For both phases and dipping times of 45 s and 150 s, grain sizes in µm and respective area fractions are plotted in Figures 43(c) and 44(c). Additionally, there is a coarseness in grain size and irregular growth as dipping time increases, especially for the Fe_2Al_5 phase, as shown in Figures 44(a) and (b) for the Fe_4Al_{13} phase.

Presumint that the grain shapes are spherical with a diameter D in µm, and Equation (2) has been applied to calculate the average diameter of the grains, i.e., the arithmetic mean diameter of the measured grain size;

$$D_{mean}^{N} = \frac{\sum_{i=1}^{m}(N_i \times D_i)}{\sum_{i=1}^{m} N_i} = \sum_{i=1}^{m} f_i^N \times D_i \qquad (2)$$

where: (N_i) number of grains, (D_i) average diameter, (f_i^N) area fraction of each class (i)

As shown in Table 4, the data of the mean diameter of the samples for both phases as well as at two different dipping times, have been presented. The results show that the average grain size does not exceed one micrometer for both phases at 45 s dipping time, i.e., for Fe_2Al_5 is around 0.87 µm, while for Fe_4Al_{13} is about 0.49 µm, which indicates that the grain of Fe_2Al_5 is bigger in size, as can be seen in Figure 43 (a) and (b). Increasing dipping time results in an increase in grain size at a dipping time of 150 s; the average diameter for Fe_2Al_5 is 1.74 µm and doubled with the dipping time. On the other hand, the average grain diameter of Fe_4Al_{13} remains below one micrometer, about 0.75 µm.

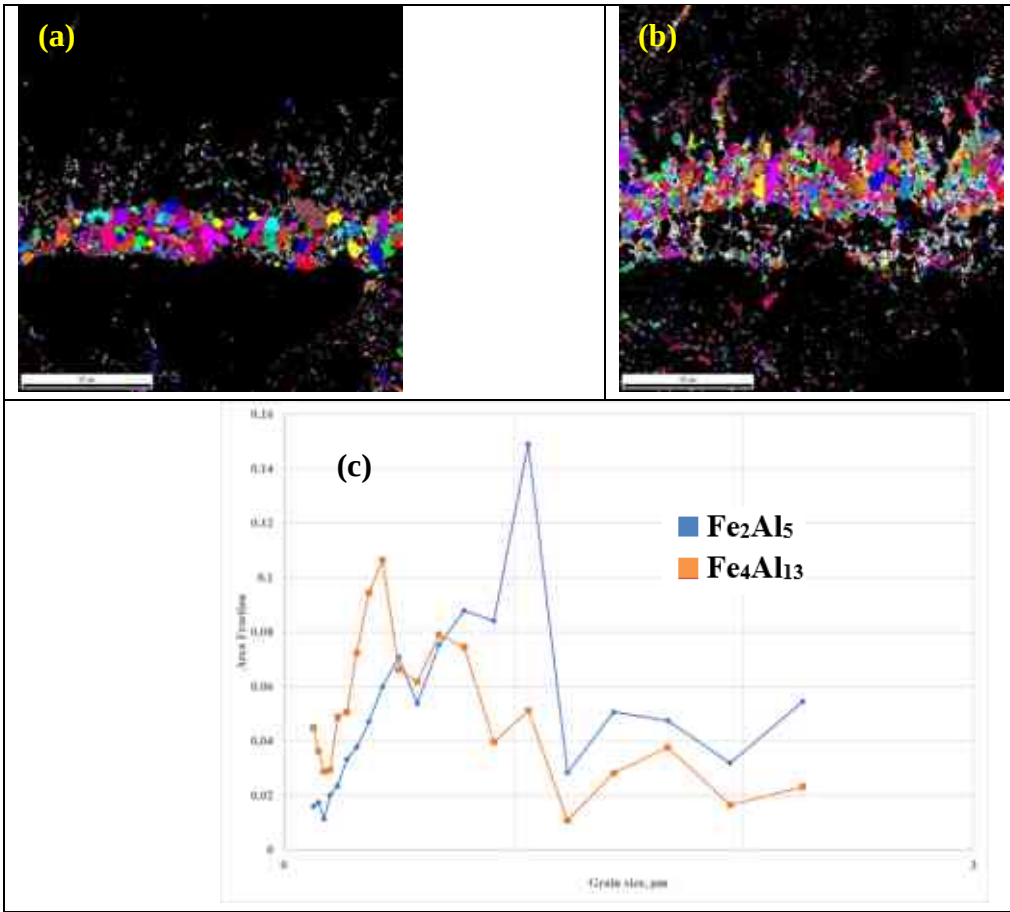

Figure 43. EBSD scanned the area that shows the grain and grain boundaries for the Fe_2Al_5 phase (a) and for the Fe_4Al_{13} phase (b); the grain size measurement, which includes grain edges, was processed using TSL OIM Analysis 8 software plotted as grain size vs. area fraction (c) for sample dipped for 43 s.

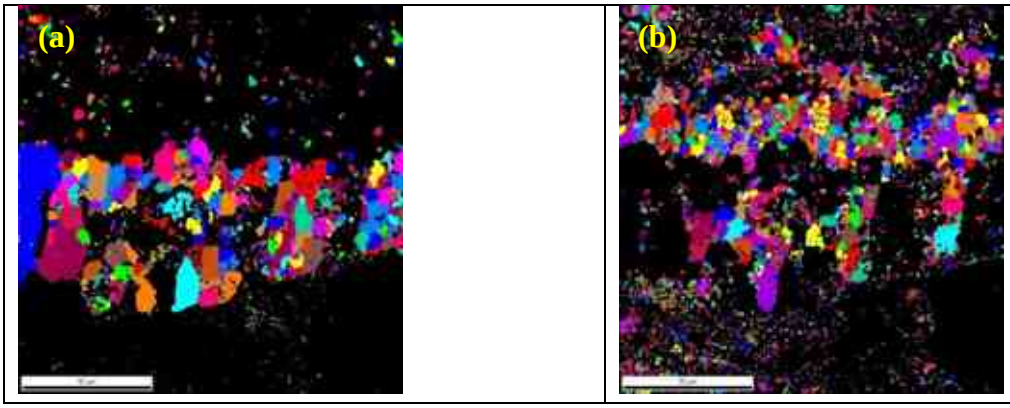

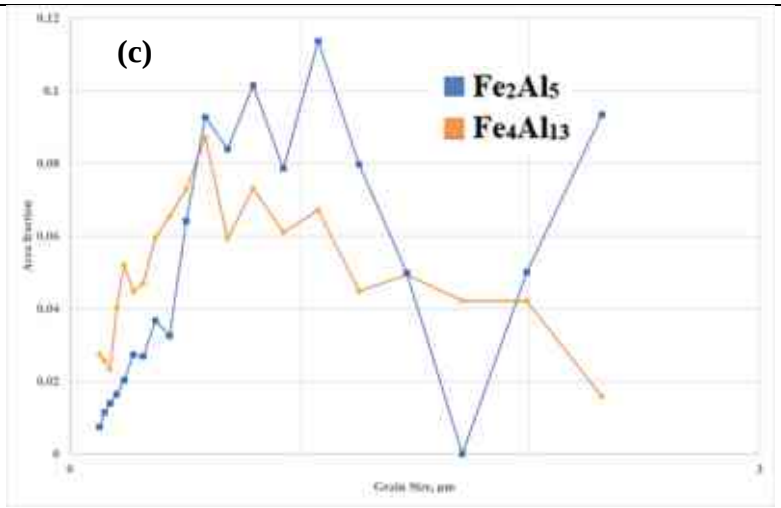

Figure 44. EBSD scanned the area that shows the grain and grain boundaries for the Fe_2Al_5 phase (a) and for the Fe_4Al_{13} phase (b); the grain size measurement, which includes grain edges, was processed using TSL OIM Analysis 8 software plotted as grain size vs. area fraction (c) for sample dipped for 150 s.

Table 4. The data analysis for the measured grain size for both phases, i.e., Fe_2Al_5 and Fe_4Al_{13}, and for the two dipping times are presented. Here is the mean diameter in µm along with the standard deviations.

	Sample dipped for 45 s		Sample dipped for 150 s	
	Fe_2Al_5	Fe_4Al_{13}	Fe_2Al_5	Fe_4Al_{13}
Average grain size (µm)	0.87	0.49	1.74	0.75
Standard deviation	0.27	0.15	0.43	0.2

3.2.2.4 Kinetic growth of intermetallic layer

The copper pre-coated carbon steel C45 specimens were immersed in molten aluminum for varying immersion times, and their cross-sectional structure is shown in Figure 40. As previously mentioned, the thickness measurements of the intermetallic layers were conducted on the cross-sections of the specimens. As shown in Figure 45, the results of the measurements were plotted as layer thickness in (µm) versus immersed time in (second).

From the plotted results, one can deduce that the θ-Fe_4Al_{13} has a linear and constant growth at the early stage of immersing the sample, and the thickness of θ-Fe_4Al_{13} set about thicker compared to the η-Fe_2Al_5 layer. With the passage of time, the growth line follows steady-state conditions that exhibit linear growth. In contrast, the η-Fe_2Al_5 demonstrates a tendency to parabolically increase in thickness, especially at immersion times of 45, 85, and 150 s. In the 150-300 s period, sharply inclined could indicate a significant increase in growth rate, where the thickness becomes almost twice that of the phase θ-Fe_4Al_{13}. The total thickness is the summation of both layers, i.e., θ-Fe_4Al_{13} and η-Fe_2Al_5 obeying the same growth condition as η-Fe_2Al_5 is parabolic growth.

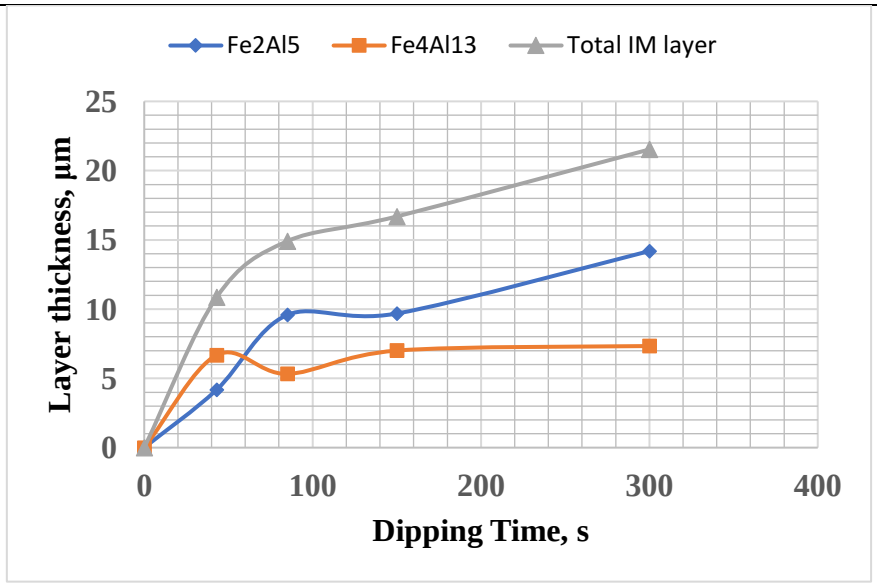

Figure 45. The growth of intermetallic layers in the function of the samples holding times in the molten aluminum bath.

In order to determine to what extent the measured thicknesses comply with the so-called parabolic growth rate function, Equation (3) was applied as;

$$y = (kt)^n \qquad (3)$$

where: (y) represents the measured thickness, (k) constant growth rate, (t) immersing time, and (n) time exponent.

For the purpose of determining the time exponent within each grown layer, a statistical linear regression analysis was conducted by calculating the natural logarithm (ln) of Equation (3) as follows;

$$\ln y = \mathrm{n} \ln t + \mathrm{n} \ln k \qquad (4)$$

Data of measurement results drawn from Equation (4) are illustrated in Figure 46, and the slope of the linearity that is measured as a result of the time exponent can be found in Table (5).

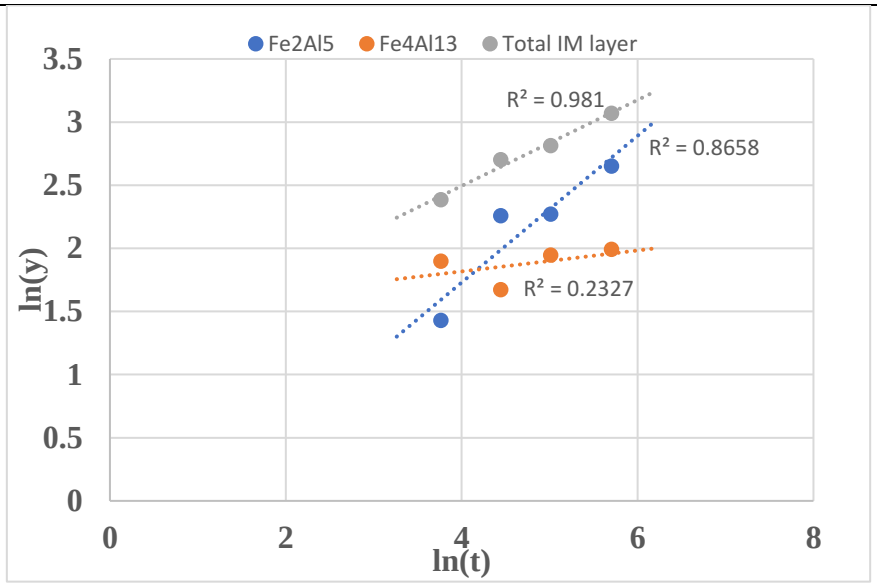

Figure 46. Linear regression lines drawn through the logarithms calculated from the measured data, ln(y) layer thickness vs. ln(t) immersion time.

Table (5). The time exponent obtained from the linear regression analysis for the data drawn in Figure (46).

Intermetallic Layer	**Time exponents, n**
Fe_2Al_5	0.58
Fe_4Al_{13}	0.08
Total IM layer	0.34

From Table (5), whereby the time exponent was presented accompanying the parabolicity behavior, the outcomes reveal that the θ-Fe_4Al_{13} layer has a value of n about 0.08, which indicates that the growth doesn't obey parabolic and improves what is presented in Figure (46), thereby the θ-Fe_4Al_{13} follows linear growth kinetic. Compared to the η-Fe_2Al_5, which has an n value found equal to 0.58, the layer strongly follows a parabolic growth kinetic.

Moreover, the parabolic growth rate kinetic is inversely proportional to the intermetallic layer thickness expressed by Equation (5).

$$\frac{dy}{dt} = \frac{k}{y} \qquad (5)$$

By integrating Equation (6), then.

$$y^2 = 2kt + c \qquad (6)$$

From Equation (6), the kinetic growth rate could be determined for the η-Fe_2Al_5 layer by plotting the square of measured thickness with various immersing times, see Figure (47).

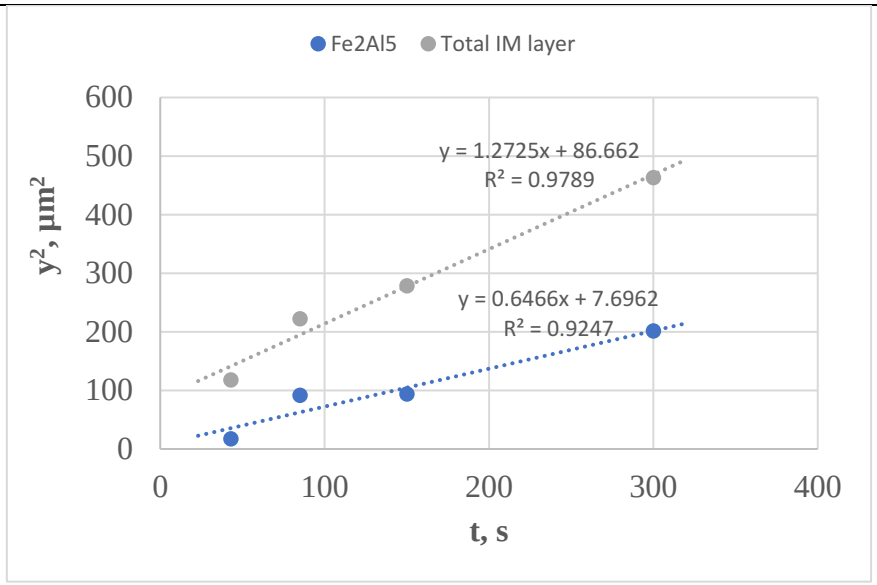

Figure 47. Kinetic growth rate diagram based on Equation (6); plotting the square of layer thickness y versus the immersion time, t.

Identifying the slop from Figure (47) represents the kinetic growth rate for the η-Fe_2Al_5 layer, which was found to be about 0.646 $\mu m^2 . s^{-1}$ or (6.46×10^{-13} $m^2 . s^{-1}$), and the total layer thickness of the intermetallic layer is about 1.27 $\mu m^2 . s^{-1}$ or (1.27×10^{-12} $m^2 . s^{-1}$). As a result of the obtained values, it is evident that copper pre-coating on carbon steel C45 before hot-dip aluminizing diminishes the growth of Fe_2Al_5.

Considering the growth mechanism of the θ-Fe_4Al_{13} layer, as previously determined, the growth is linear and follows a steady state condition. It's convenient with the finding obtained by Bouche' K. et al. [103]. Therefore, the rate of the reaction is directly proportional to the time. Equation (7) expresses the linear growth rate.

$$\frac{dy}{dt} = k \qquad (7)$$

After integrating Equation (7).

$$y = kt + c \qquad (8)$$

where: y represents the thickness of the layer here; θ-Fe_4Al_{13}, k; constant rate, and t; present time here; dipping time.

Equation (8) results are plotted in Figure (48); the best line fit for linear growth is obtained with a constant growth rate of k equal to 0.004855 µm. s^{-1} or (4.855×10^{-9} m. s^{-1}).

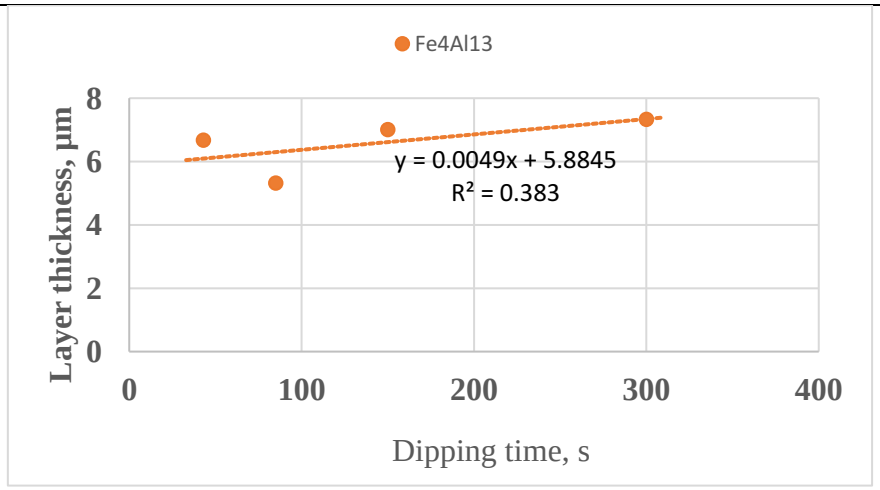

Figure (48) kinetic growth rate diagram based on Equation (7), i.e., layer thickness plotted vs. time of immersion.

Now, another question is arising: which phase is it primary and is the one that is initiated and settles at the interface, or is it the other phase that develops/grows from it or depletes from it? Some believed that the θ-Fe_4Al_{13} initiated directly from the liquid aluminum phase due to an eutectic reaction (liquid → θ-Fe_4Al_{13}). In contrast, others stated that the θ-Fe4Al13 would initiate due to a peritectic reaction (liquid+ η-Fe2Al5→ θ-Fe4Al13), where the last theory could be closer to reality. It's shown with a time-resolved X-ray experiment performed by Guillaume Pasche et al. [104] where they observed that blocks of η-Fe_2Al_5 nucleated at the solid surface and started to grow toward the substrate instantaneously θ-Fe_4Al_{13} start to initiate at the liquid Al surface close fitting to the (η) phase. To testify to the experimental observation, a dynamic molecular design combined with experimental data emphasizes consistency with the same approach [105]. Clearly, any phase's inception and growth are governed by the principle of thermodynamic driving forces, which means that the phase with a higher number of negative formations is more likely to form in the first stage. Pretorius R. et al. [106] developed a new concept of phase formation sequence based on effective heat of generation ($\Delta H'$) the model predicts the series of Al-(M) phases in the phase diagram of the targeted element (here (M) is any element combined with Al in the binary phase diagram).

$$\Delta H' = \Delta H^{\circ} \times \left(\frac{C_e}{C_c}\right) \qquad (9)$$

Where: ($\Delta H'$); is the effective heat of formation in kJ/mol, (ΔH°); standard heat of formation (enthalpy) in kJ/mol, (C_e); the effective concentration of the limiting element: Taking the limiting element at the lowest eutectic temperature as the element that is consumed first during the formation of one phase at the interface in at.%, and (C_c); is the concentration of the limiting element in the compound.

It is crucial to determine the development sequence or initiation of the Fe-Al phases due to the reaction between solid metal and liquid metal using the effective heat of generation model by

Jung-Moo Lee et al. [107]. This model clearly establishes that the Fe_4Al_{13} first phase forms, and the Fe_2Al_5 grows inward due to the reaction of Fe_4Al_{13} with the Fe (Fe_4Al_{13}+Fe→Fe_2Al_5).

3.2.2.5 Thermodynamic considerations of Fe-Al and Al-Cu compounds at the interface

In this section, concise discussions are presented about reorganizing and evaluating the thermodynamic equilibrium firstly, with regard to Al-Cu, where the heat-treated carbon steel C45 pre-coat with copper is in contact with the liquid aluminum, and secondly, with regard to Fe-Al, as the outcomes of HDA copper precoated carbon steel C45 indicated that the intermetallic compounds are located within the Fe-Al phase diagram. Several compounds are produced at various temperatures in accordance with the Al-Cu equilibrium phase diagram [108]; the present study conducted the experiments at 700 ± 10 ºC so that most of its attention will be focused on these compounds developed at 700 ºC. In addition, based on the literature whereby HDA was performed on copper/brass, according to the metallographic examinations, the constituents of the intermetallic phase are Al_2Cu [109], AlCu, Al_2Cu_3, and the Al_4Cu_9 [110] compounds are also observed.

There is a possibility that the following reactions will take place at the interface between liquid aluminum and solid copper in HDA of copper, where interaction between the solid copper and the liquid aluminum is most likely to occur.

$$2Al_{(l)} + Cu \rightarrow Al_2Cu \qquad (10)$$

$$Al_{(l)} + Cu \rightarrow AlCu \qquad (11)$$

$$4Al_{(l)} + 9Cu \rightarrow Al_4Cu_9 \qquad (12)$$

$$2Al_{(l)} + 3Cu \rightarrow Al_2Cu_3 \qquad (13)$$

The thermodynamic formation enthalpies of the aforementioned compounds at different temperatures, are based on previously conducted research. Table (6) summarizes some of the related work.

Table 6. The effective heat of formation of the Al-Cu compounds.

Compound	Temperature, ºC	Effective heat of formation, EHF ($\Delta H'$), kJ/mol.	Ref.
AlCu	400-500	-6.68	[111]
Al_2Cu		-6.76	
Al_2Cu_3		-5.84	
Al_4Cu_9		-5.61	

The EBSD analysis indicates that the intermetallic layer is composed primarily of Fe_2Al_5 and Fe_4Al_{13}, thus indicating that Fe-Al phases are predominant in the intermetallic layer. Based on the previous investigation presented in Table 6 of the effective heat formation of some Al-Cu compounds in comparison with results obtained from previous study [107] for the Fe-Al phases, it has been established that Fe-Al phases exhibit higher negative values in contrast to Al-Cu phases, explaining the absence of Al-Cu compounds.

3.2.2.6 Nucleation and grain structure of the IM layers

In Figure 39(b), the highlighted structural details in the cross-section of the heat-treated copper precoated steel specimen provide clear evidence of the compositional and textural changes that happened in the steel substrate's upper layer just below the copper coating. Moreover, the EDS spot analysis revealed the presence of Cu just 2 µm beneath the interface with an atomic % of (7.09). As the solubility of Cu into solid Fe is limited and varies with temperature, the existence of Cu suggests a high probability of solid solution initiation below the interface. This is accompanied by tiny Cu-rich precipitates, as indicated inside the circle in Figure 39(b). Therefore, it can be inferred that the refinement of carbon steel C45 just below the interface must have happened concurrently with the development of the Fe-Cu solid solution phase during heat treatment at 640 ± 10 ºC of the copper electroplated steel specimen.

When the copper coated carbon steel C45 comes into contact with molten aluminum, the Al-Cu intermetallic compounds likely begin to form at the interface of the solid copper and liquid aluminum once a certain saturation level of dissolved Cu atoms is reached in the hot liquid Al surface layer. On the other hand, it is supposed that these solid nuclei of Al-Cu compounds primarily form at the solid-liquid interface of the HDA sample. In that case, they may also affect the nucleation of iron aluminides, which, otherwise, have higher negative formation Gibbs energies than the Al-Cu intermetallic phases.

Therefore, it can be theorized that during the HDA process, the thin and solid copper coating will first start dissolving physically in the hot molten Al, followed by the precipitation of the mentioned Al-Cu phase. This can delay the later nucleation and formation of a more significant amount of iron aluminides originating from the two main constituents of the solid iron base substrate and liquid Al. Finally, the minimal amount of Cu will fully decompose and diffuse away, probably mostly into the molten Al bath. Nonetheless, the initial surface presence of Cu will interfere with the number of nucleation sites and also the growing phenomena of the thermodynamically more favorable and more stable iron aluminides appearing with smaller average sizes at short dipping time, as clearly shown in Figure 39(b).

Upon prolonged dipping, more Fe-Al intermetallics will nucleate at the liquid/solid interface and cluster together; as a result, the thicker intermetallic layer then appeared on the SEM images as two distinct layers by color contrast, mainly composed of Fe_4Al_{13} and Fe_2Al_5 between the carbon steel and the aluminum topcoat. At the short immersing time, both phases have finer grain with small size, as previously determined that the θ-Fe_4Al_{13} has constant

growth. It's also reflected in the grain refinement, which has the same steady growth. On the opposite, the η-Fe_2Al_5 concurrently with the increasing dipping time the grain size also increased, and coarse grain clearly observed and is relevant to most studies, where the growth occurs in the direction of the C-axis of the crystal structure [112] where the most diffusion of Al atoms occur in this direction.

From the above discussion, the formation of the Al-Cu compounds could hinder rapid diffusion (at the very beginning stage of the dipping process), which led to a reduction in the growth kinetic of the iron aluminides. Consequently, this intermetallic layer appears with a minimal thickness, i.e., the copper pre-coating could indeed help diminish its total thickness with the formation of less unfavorable cracks.

CHAPTER 4: Oxidation and corrosion resistance investigation

4.1 Cyclic oxidation resistance of HDA carbon steel C45

4.1.1 Experiments and methodologies

Cyclic oxidation tests were performed on the samples in an electric resistance furnace. The specimens were heated from the room temperature to 700°C in air for 8 hours, and then they were kept inside a furnace, which was switched off for 16 hours to allow it to return gradually to the ambient temperature. This cycle was repeated thrice.

4.1.2 Results and discussions

4.1.2.1 Characterization of aluminized samples after exposure to hot cyclic air

The samples exposed to hot air were sectioned and prepared for SEM, EDS, and elemental mapping analyses. A rather thick-coated segment of the HDA specimen surface is shown in Figure 49(a). Several observations can be drawn through the SEM images: with heating, the peak of the tongue or finger-like structure reaching toward the steel substrate became coarser (wider) rather than needle-like. A narrow emergent layer (marked in Figure 49(b)) can clearly seen between the finger-like structure and the steel substrate (a lighter grey zone). This also fills in the interstices between the finger-like areas and is free of cracks and pores. In Figure. 50, it is also seen that the original top aluminum layer was fully transformed into a Fe–Al intermetallic material. EDS determined the approximate elemental chemical compositions of the material at five separate spots Figure 50(a) are presented in Table 7. In addition, the EDS analysis was also carried out in the lighter boundary areas marked in Figure 50(b), and the results are presented in Table 8. For this specimen, the EDS spot analysis also revealed a few Mg-silicate-like inclusions (E.g., spot no.3 in Figure 50(a)), most probably originating from the molten aluminum bath itself and encapsulated in the solidified aluminum layer.

At 700°C in air, the aluminized surface zone still resists fast oxidation, i.e., oxide scale formation, which would otherwise exclude its advantageous application in such environments. As long as the top aluminum coating is in a direct contact with hot air, thermodynamically, its preferential oxidation to Al_2O_3 or some mixed oxides is the most favorable conversion reaction, which is also dependent on the actual local alloying or contaminating elements in the outermost layer. It is also worth mentioning here that alloying aluminum with manganese will also improve the room-temperature wet corrosion resistance properties of aluminum [113].

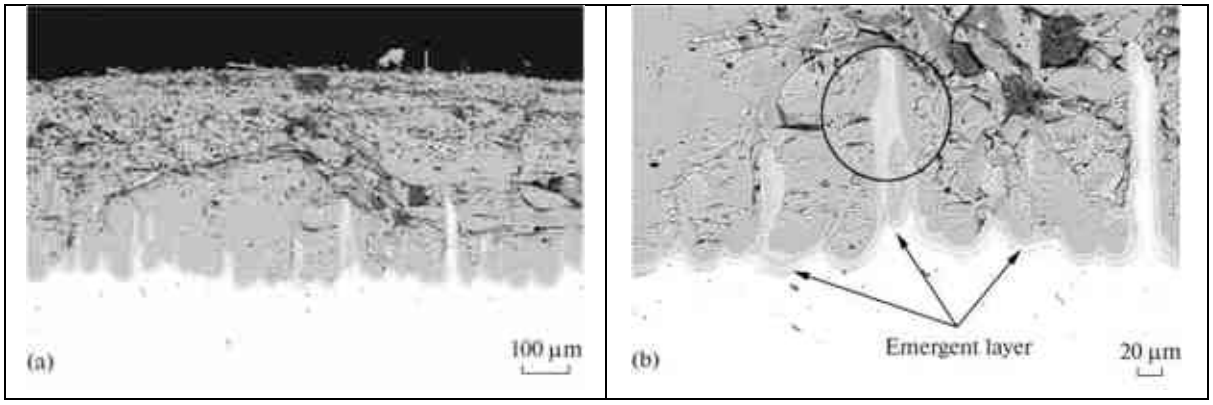

Figure 49. SEM of the aluminized sample after exposure to hot air: (a) cross-section and (b) emergent layer between finger-like structure and steel substrate.

Based on the composition data summarized in Table 8 and the corresponding SEM image in Figure 50(b), it has been found that the emergent region initiated and developed during the high-temperature exposure period is structurally sound and free from oxides. The calculated atomic ratios revealed that this phase is likely to be FeAl, and it is most probably grown from the neighboring zones of $FeAl_2$ – Fe_2Al_5 [114].

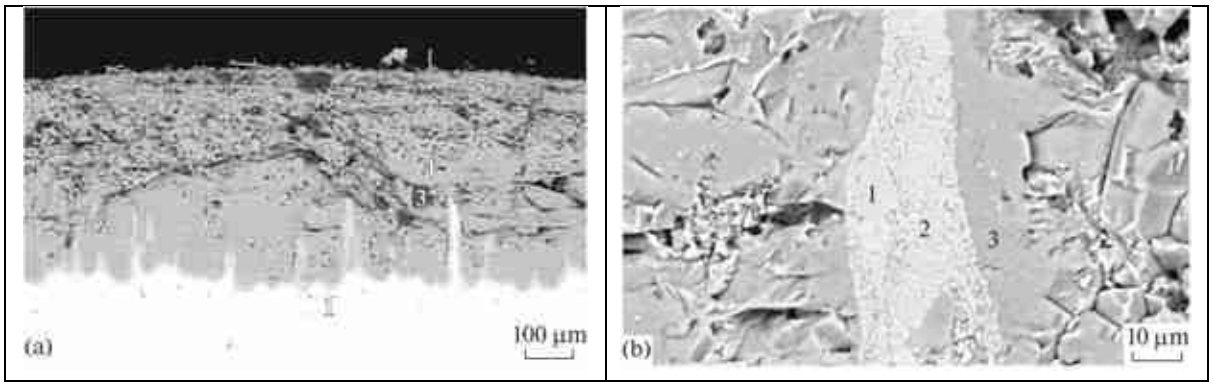

Figure 50. (a) SEM images showing specified spots via EDS analysis, (b) specified spots in the initiated bright region marked in Figure. 6b by inside circle.

The effect of after heat-treatments of similar HDA specimens for several minutes only was studied and reported elsewhere [115], and it was found that the inner FeAl and Fe_3Al layers have structures without oxidation. Although, in general, this statement might be accurate for cases when the high-temperature hot air exposure periods are relatively short, the cyclic oxidation experiments described here proved that after long periods of hot exposures at 700°C in air, a few at % oxygen in the inter-metallics zone could be detected by EDS (see Tables 7 and 8). Otherwise, the upper part of the intermetallic zone became almost fully converted to the Fe_2Al_5 phase (see the molar ratios in Table 7), and this latter observation of the present study coincides well with the conclusions in [115].

From the SEM-EDS mapping (Figure 51), it is seen that some minor oxide inclusions are also formed in some portions of the aluminized surface layer. As they always contain silicon and

magnesium as well, their origin might be linked to a high chemical affinity of these elements to oxygen infiltrated and diffused into the aluminized zone.

Table 7. Chemical elements detected by EDS spot analysis at different points (Figure 50(a))

Points No.	Al, at %	Fe, at %	Atomic ratios, Al/Fe	O, at %	Mn, at %
5	64.7	24.0	2.70	4.6	0.6
4	67.3	25.3	2.66	1.9	0.3
3 (inclusion)	*1.5*	*2.0*	*Si: 29.4 at % Mg: 15.3 at %*	*40*	–
2	62.8	31.3	2.01	1.5	0.3
1 (steel)	0.81	94.8	–	–	1.0

Table 8. Chemical elements detected by EDS spot analysis at different points (Figure 50(b))

Points no.	Al, at %	Fe, at %	Atomic ratios, Al/Fe	O, at %	Mn, at %
1	45.6	46.6	~1	–	0.42
2	46.51	44.8	~1	–	0.79
3	66.13	28.44	~2	1.58	0.31

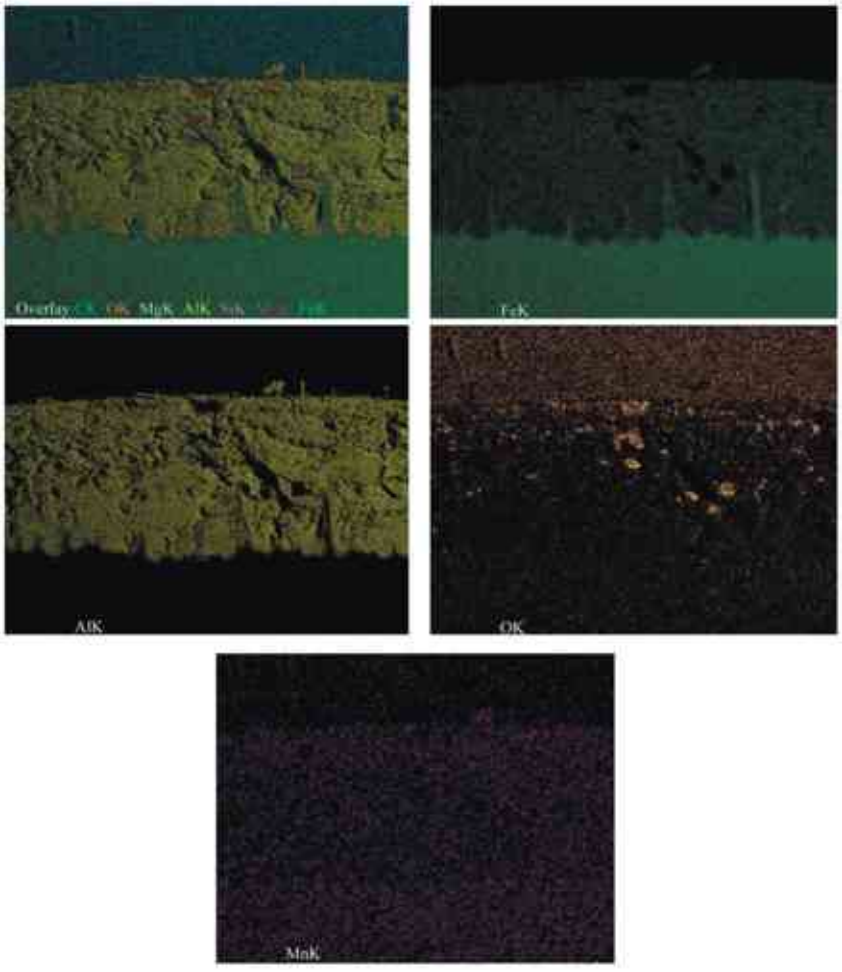

Figure 51. EDS elemental mapping of heat cycled HDA coated specimen: overlay of all detected elements, Fe, Al, O, and Mn.

4.2 Corrosion resistance of HDA carbon steel C45 half immersed in molten salts

4.2.1 Experiments and methodologies

The specimens were polished, degreased in an ultrasonic bath with acetone for about 20 min, and then aluminized. The immersion time and temperature were maintained constant while dipping samples into the molten aluminum bath. The cross-section SEM images of the close-to-surface structure of the hot-dip aluminized specimens were investigated.

A salt blend containing NaCl and Na_2SO_4 was prepared in a mass ratio of 1:3; the salt blend was ground using a pestle and mortar to ensure homogeneity. To verify that the melting temperature of the salt mixture would be less than 700 °C, the mixture was subjected to differential thermal analysis (DTA), measuring approximately 650 °C. A certain quantity of salt mixtures was added to the HDA sample inside the crucible to ensure that half of the HDA sample is immersed in the salt mixture after melting. Various exposure times (8, 24, and 72 h) were set inside the electric furnace at 700 °C for the sample exposure. All the time intervals designed include the melting time of the salt's mixture to become a liquid and the target temperature, around 40 min across each range. The sample is settled in a small crucible afterward filled with sufficient amounts of salt mixture to obtain a meniscus line at the middle of the HDA sample, resulting in the test setup shown in Figure 52.

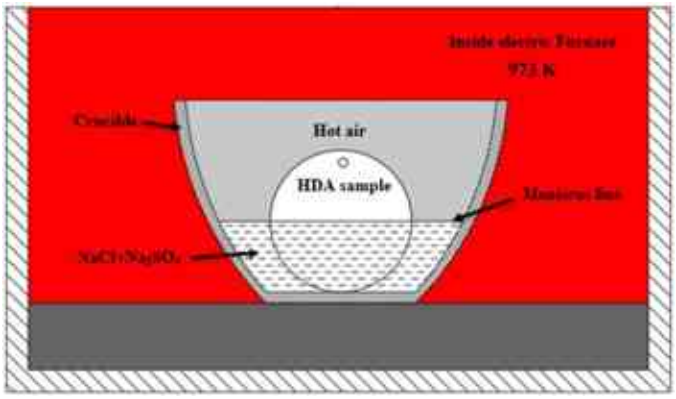

Figure 52. Schematic cross-view of test setup.

HDA carbon steel C45 and corroded samples were examined with sophisticated metallographic techniques to characterize the surface appearance and morphology and determine the elemental distribution; both halves of the HDA steel specimen were analyzed. A ZEISS EVO scanning electron microscope was used to visualize the sample's surface morphology and topography after different exposure times using electron backscattering (BSD) imaging provided by a ZEISS EVO scanning electron microscope. Using energy dispersive spectroscopy (EDS), the distribution of elements across the surface was measured along with changes in its appearance caused by the chemical interaction between the molten salts and furnace air. To observe any changes that occurred during the exposure periods, the samples were sliced and observed for the cross-sectional structure; in addition, the elemental map over the cross-section, as well as the in-depth elemental distribution, were scanned and analyzed by a PFIB-SEM equipped with an EDS based HeliosTM G4 PFIB CXe Dual Beam and TSL OIM Analysis 8. The SEM image

resolution was set at 1536_1024, and the EDS spot diameter size was 0.5 mm. Moreover, an optical microscope ZEISS Axioscope was used to show the substrate structure, intermetallic layer, and interdiffusion layer after exposure.

4.2.2 Results and discussions

4.2.2.1 Surface appearance and morphology after exposure

The surface topography appearance and morphology were examined using the backscatter (BSD) imaging technique across the top surface of the sample regions, and these data were combined with elemental analysis using EDS spots to gather all the variations in morphology and composition associated with time. Figure 53(a) shows a half section of the non-immersed sample, which was exposed to hot air for 8 h in a furnace. There are several tiny pores on the surface, and the corrosion product appears compact and well-adhered to the carbon steel C45 sample, i.e. no cracks or cavities are visible. Various contrast colors were visible scattered over the top surface, resembling rounded particles. During the EDS analysis, some iron (Fe) was detected diffusely at the top surface, as indicated by the mention of (Fe–Al) at a particular spot (1) in Figure 53(a) with a molar ratio (1:2). Conversely, the immersed part shows crystals of (Fe–Al) with a ratio close to (1:1). Carbon and sulfur were also detected at Spots 2 and 3 in Figure 53(a) and Spots 2 and 4 in Figure 53(b). The protective layer of alumina (Al_2O_3) is rarely seen alone, rather, it is combined with a blend of aggressive substances. The sample after 24 h of exposure is shown in Figure 53(c,d). There are two different, grayish-colored spots (3) in Figure 53(c) that are associated with forming fern-like to dendritic-like structures, where the aluminum oxide is highly contaminated with Na and S, whereas the aluminum oxide molar ratio is lower than Na and S with Cl added. Over the area of the non-immersed region, the aluminum oxide was identified with an atomic ratio of (2:1) approximately in conjunction with Fe, Na, and S at Spots 1, 4, and 5 in Figure 53(c). In addition to colonies and tiny pores in the nonimmersed region, small cracks can also be observed. Although a compact corrosion product layer, it adheres to the base carbon steel C45 metal. The half immersed in

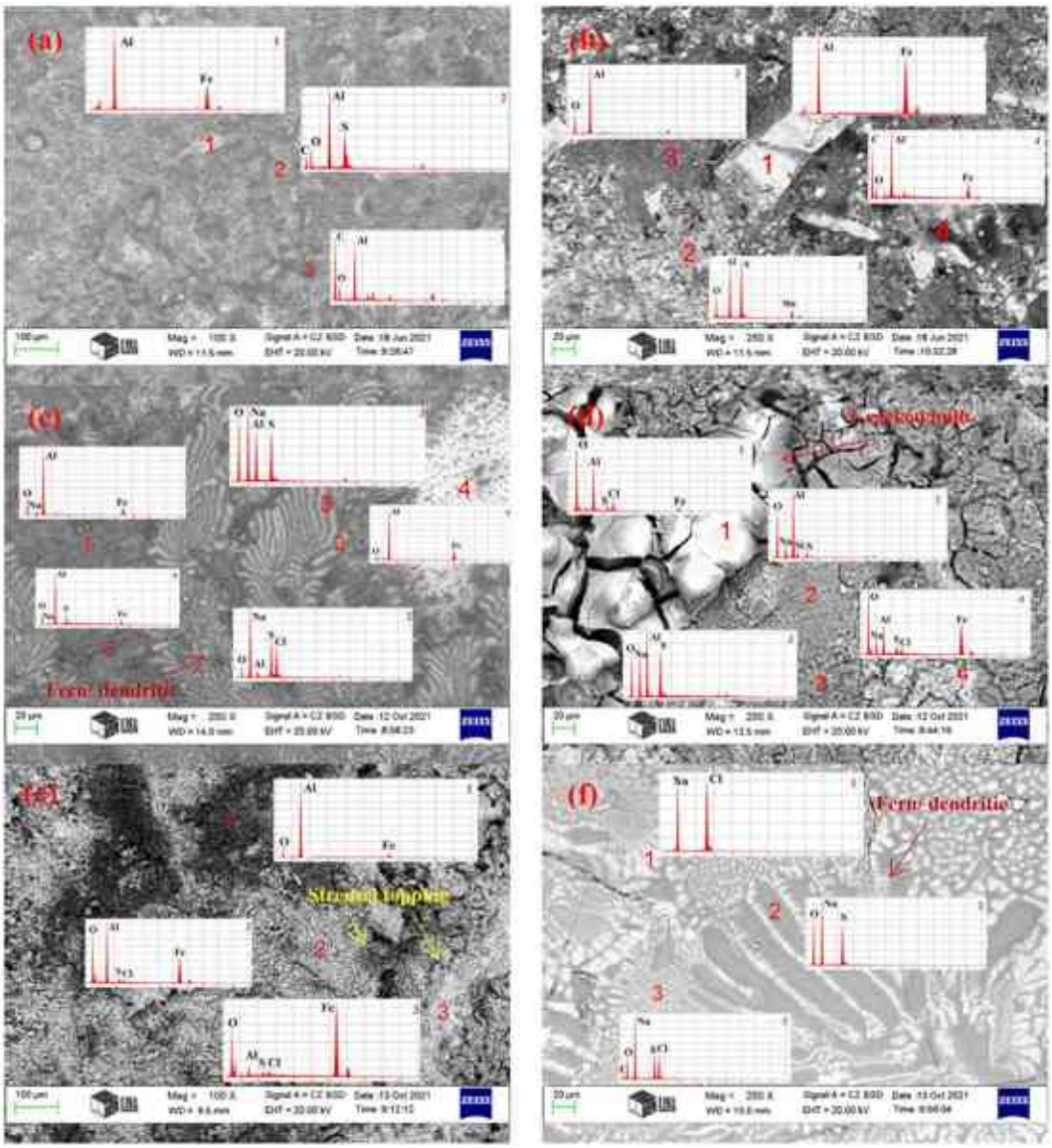

Figure 53. Backscatter SEM images revealing the phases formed at the surface for both halves (lefthand column: non-immersed; right-hand column: immersed), during exposure periods of (a) & (b) 8 h; (c) & (d) 24 h; (e) & (f) 72 h.

molten salts for 24 h exhibit a morphology of cracked bulbs initiated at the top surface, where pores can also be observed in Figure 53(d). It was found that there were high levels of O with an Al ratio (2:(3/2)), as well as some contaminants such as Fe at Spot 1 Figure 53(d). On the surface, aluminum oxide in various molar ratios is observed, along with impurities at Spots 2, 3, and 4 in Figure 53(d). The sample exposed for 72 h displayed severely altered regions at the upper part kept in hot air and at the lower part immersed in molten salts, as illustrated in Figure 53(e,f), respectively. Cracks, pores, and cavities are found in the non-immersed part region; these sections have morphologies reminiscent of streusel toppings, while the other part exhibits a unique shape resembling ferns, with cracks and pores as well. There is the detection of aluminum oxide along with low to high contents of Fe, and corrosive species are observed at Spots 1, 2, and 3 in Figure 53(e,f), showing the main corrosive substances that dominate the

top surface detected via EDS spot analysis. It was also observed that Fe is present on the surface, which may contribute to the formation of oxides or the formation of intermetallic compounds (Fe–Al). Furthermore, the latter phases may serve as aluminum-containing reservoirs (i.e., sources of aluminum) to heal the deteriorating aluminum oxide layer [116]. Increasing the exposure time may also accelerate oxidation/corrosion by increasing the chances of aggressive species diffusing through gaps, cavities, and pores. It is possible to observe this phenomenon as the exposure period changes. There is also the possibility that some elements in the steel matrix may diffuse outwards and form new compounds on the surface. The chemical affinity of species as they encounter each other, coupled with the characteristics of species transport and the activation energy required to form new compounds, determines the outcome of these reactions. According to Equation (14), aluminum in contact with air will form a thin layer of

aluminum oxide (i.e., Al_2O_3) on its surface. It is assumed that this protective oxide scale will prevent further oxidation even if some parts are occasionally detached or spalled because it will be formed repeatedly to repair the damage.

$$4Al + 3O_2 = 2Al_2O_3 \qquad (14)$$

In the studied system, however, several factors prevent the formation of an ideal protective aluminum oxide layer over the entire surface area of the given HDA steel exposed to the highly corrosive environment tested. Due to this, improving the level of corrosion protection in such systems remains a very challenging task. Therefore, a more comprehensive discussion is presented after briefly describing these factors and processes. A longer exposure time will result in more reactions between the species; at that point, condensed reaction products can settle on the top surface of the samples, thereby altering their morphology and appearance.

4.2.2.2 Structural characterization of cross-sectioned HDA after exposure

In addition, the specimens were sliced to determine the cross-sectional structural characteristics of both non-immersed and immersed regions; the elemental distribution was also determined from the top surface down to the substrate. The gradual disappearance of the original finger-like structure of the HDA specimens was observed during high-temperature exposures and after the exposure periods presented in Figure 54(a–f), the distinct surface layers (aluminum topcoat and intermetallic layer) could be no longer observed (as in all cases, it transformed to intermetallics of different kinds). Figure 54(a,b) illustrates the non-immersed and immersed parts of a sample that was exposed for 8 h at 700 °C. In the non-immersed part, many tiny pores are spread throughout the section, whereas in the immersed part, they are mostly concentrated at the top surface in contact with the molten salts (see red arrows). For the samples held for 24 and 72 h, the pores coalesce and produce cracks and grooves that appear to separate two separate layers (see the red arrows in Figure 54(c–f). There is a distinct color development in the outermost layer for both the 24 and 72 h exposure periods (see the white arrows); this layer has a weak adhesion to the main coat, of course, so parts of it have separated and are easily falling off. It can be seen in Figure 54 that over time, the interface between the coating layer and the carbon steel substrate C45 becomes nearly flat, as the intermetallics have occupied the

gaps within the finger-like structure. Furthermore, as time progressed, the thickness of the coat decreases due to continuous reactions with molten salts or hot air at its outermost layer. The emerging layer (shown in Figure 54 as a light gray zone at the inner interface between the steel and outer intermetallics) also increased in thickness. Furthermore, surface alloying aluminum was also depleted, as part of it was consumed to heal the top protective layer of passive aluminum oxide.

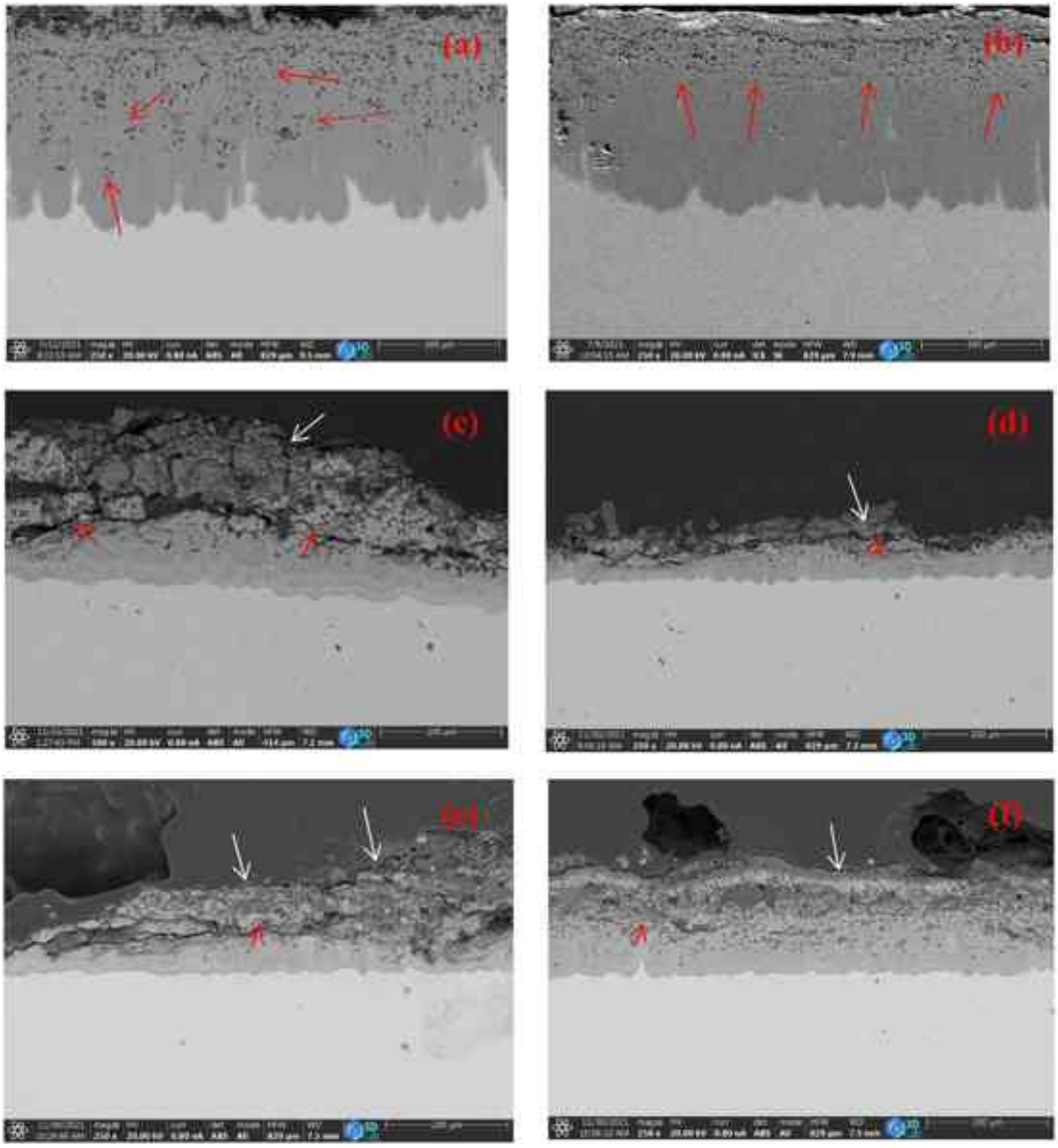

Figure 54. PFIB-SEM cross-section images for both regions in all three samples with different exposure periods of 8 h (a) non-immersed (b) immersed; after 24 h (c) non-immersed (d) immersed, and after 72 h (e) non-immersed (d) immersed.

In Figure 55, a closer inspection of some small interfacial regions reveals more intriguing details regarding the influence of exposure period on structural changes and elemental distribution in depth on both sections over cross-sections. For example, the SEM image displays an interdiffusion layer (Layer B) between the substrate (Layer A) and the intermetallic

layer (Layer C). The intermetallic layer (Layer C) adjacent to the new emergent layer (Interdiffusion layer B) also displays a tiny flake structure, as shown in Figure 55(b), representing the enlarged area marked with a circle in Figure 55(a). The results of the EDS spot analysis performed at selected points shown in Figure 55(b) are presented in Table 9. Two different contrast colors were observed among the flake-like structure (See Points 2 and 3 in Figure 55(b)), but the oxygen content of these two points also differs. The structure of the immersed section exhibits the same characteristics as those of the non-immersed part in Figures 55(c,d); results of the EDS spot analysis taken at the marked spots in Figure 55(d) are given in Table 9. The precipitates in the emergent layer (Layer B) display a needle-like or flake-like structure and appear in two black contrasts. In the blackish one labeled No. 2 in Figure 55(b), and No. 1 in Figure 55(d), the oxygen content in the immersed part is highly apparent compared to the non-immersed section. Even though C and O were present in the non-immersed area, the emergent layer can be regarded as potential phases of FeAl and Fe_3Al based on the measured and detected molar ratios. However, layer C in both areas should be $FeAl_2$ except for the immersed section, where the ($FeAl_2$) is combined with the presence of C. This could suggest a phase like FeAl(C) in the immersed half-section.

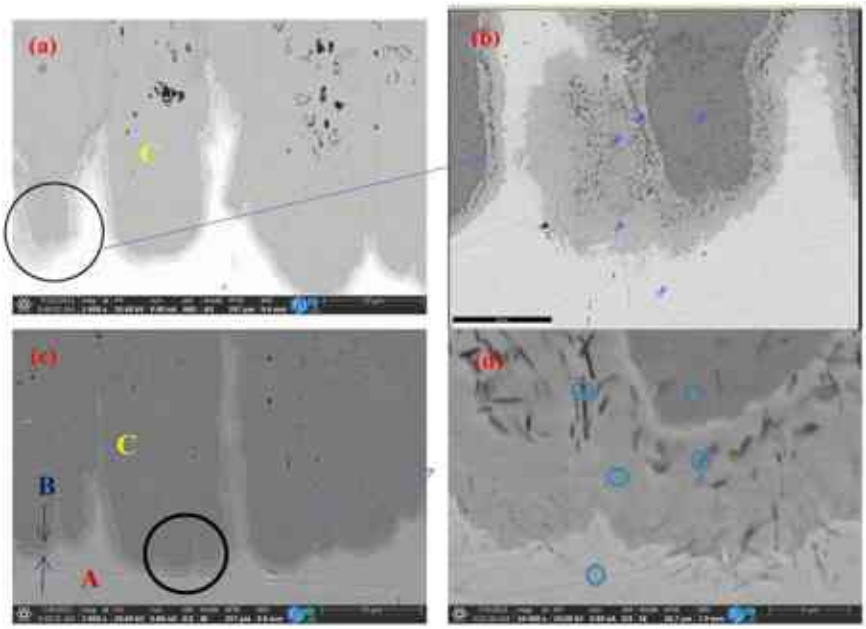

Figure 55. PFIB-SEM images showing the structure that appears at the interface between the substrate and the intermetallics layer after the exposure period of 8 h. The enlarged light grey areas (b) & (d) represent the newly formed (during the 8 h exposure) layer with a thickness of around 5 to 7 mm in average. The (a) and (b) non-immersed sections exposed were to hot air, while (c) and (d) were immersed in the molten salts.

Table 9. Data measured by EDS analysis at the spots depicted in Figure 55(b,d).

	Sample with 8 h exposure									
	Non-immersed Points					Immersed Points				
Elements in At. %	1 (Err. %)	2 (Err. %)	3 (Err. %)	4 (Err. %)	5 (Err. %)	1 (Err. %)	2 (Err. %)	3 (Err. %)	4 (Err. %)	5 (Err. %)
Fe	36.34 (2.13)	49.35 (2)	49.37 (1.97)	74.19 (1.9)	95.47 (1.79)	43.11 (1.75)	70.32 (1.67)	50.43 (1.72)	37.12 (1.76)	96.79 (1.63)
Al	63.23 (4.35)	47.41 (5.06)	46.92 (5)	23.42 (6.08)	0 (99.99)	45.93 (4.67)	27.49 (5.54)	42.6 (4.89)	60.51 (4.27)	0 (99.99)
C	0 (99.99)	0.62 (80.04)	0.94 (73.44)	0.73 (76.28)	1.3 (68.45)	10.96 (11.62)	0.83 (67.84)	5.35 (13.66)	0.5 (73.23)	0.75 (67.16)
O	0.12 (79.61)	2.23 (10.75)	1.23 (15.26)	0.86 (22.64)	2.07 (10.05)	0 (99.99)	1.17 (13.25)	0.92 (14.13)	0.93 (14.15)	2.09 (8.6)
S	0 (99.99)	0 (99.99)	0.14 (67.71)	0 (99.99)	0 (99.99)	0 (99.99)	0 (99.99)	0.23 (32.08)	0.11 (53.3)	0 (99.99)
Na	0.31 (66.83)	0.39 (67.74)	1.27 (16.8)	0.8 (37.88)	1.15 (29.04)	0 (99.99)	0.19 (75.23)	0.22 (68.15)	0.71 (15.19)	0.37 (74.65)
Cl	0 (99.99)	0 (99.99)	0.12 (61.07)	0 (99.99)	0.01 (91.17)	0 (99.99)	0 (99.99)	0.26 (12.68)	0.11 (58.95)	0 (99.99)
Possible phases*	$FeAl_2$	FeAl	FeAl	Fe_3Al	Substrate	FeAl(C)	$Fe_3Al(O)$	FeAl(C,O)	$FeAl_2(O)$	Substrate

*The possible phases were estimated according to the EDS elementary spots analysis.

Furthermore, the black flake/needle-like structure is located in two locations within the two layers; in the B1 layer, it accumulates at the interface with the substrate, while in the B2 layer it accumulates in the middle of the layer, as shown in Figure 56(a). Approximately 10 mm in thickness of the new layer in the adjacent area immersed in melt salt is shown in Figure 56(c) with only one layer of light gray color (Layer B). Additionally, the layer exhibits a flake-like structure within the layer shown in Figure 56(d). Small circles are used to identify these spots in the EDS spot analysis, and the recorded data are presented in Table 10. Based on the EDS spot analysis, the different emergent layers are composed of the system Fe-Al–C–O, which dominates the region outside the immersion zone. In contrast, the system Fe–Al–C–O–Na dominates in the immersed part, although the constituent elements vary slightly, and C is more abundant in the submerged section. On the other hand, Fe is less significant in the submerged area and slightly more in the non-immersed section.

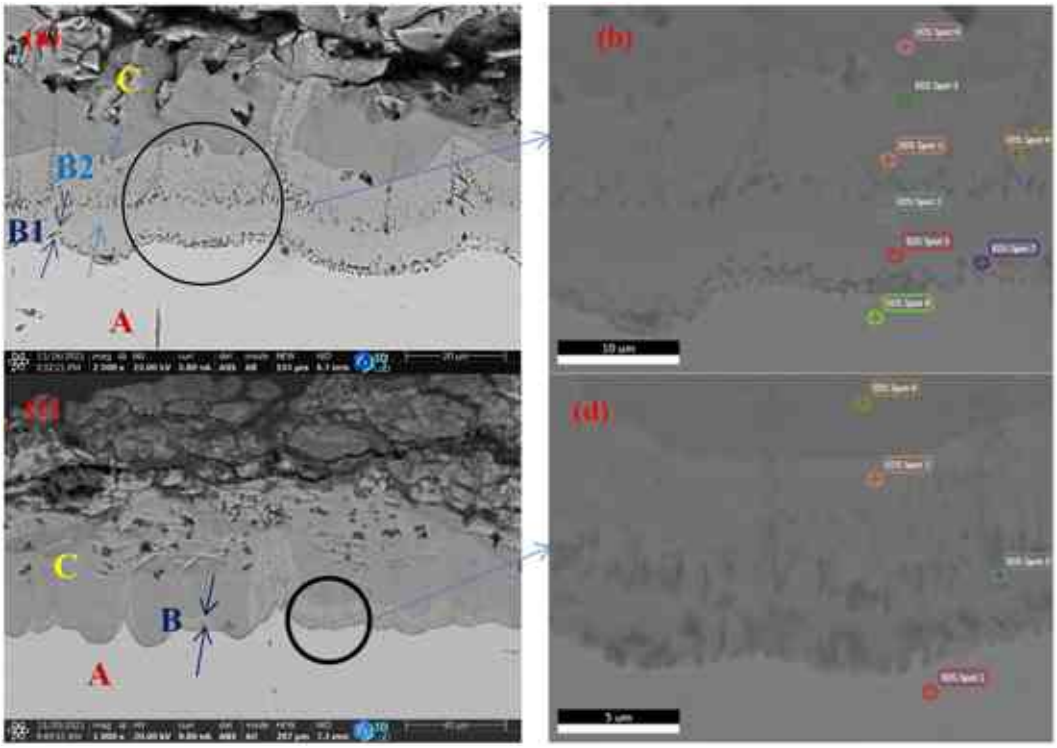

Figure 56. PFIB-SEM images showing the structure that developed at the interface between the substrate and the intermetallics layer during the exposure period of 24 h; (a) and (b) non-immersed sections exposed to hot air; (c) and (d) immersed in the molten salts.

Table 10. Data measured by EDS analysis at the spots depicted in Figure 56(b,d).

Elements in At. %	Non-immersed								Immersed			
	Points								Points			
	1 (Err. %)	2 (Err. %)	3 (Err. %)	4 (Err. %)	5 (Err. %)	6 (Err. %)	7 (Err. %)	8 (Err. %)	1 (Err. %)	2 (Err. %)	3 (Err. %)	4 (Err. %)
Fe	**31.93** (1.75)	**28.43** (1.80)	**24.93** (1.82)	**20.70** (1.87)	**21.93** (1.84)	**16.35** (2)	**37.60** (1.75)	**55.74** (1.77)	**42.89** (1.77)	**15.36** (2.01)	**19.50** (1.89)	**12.50** (2.04)
Al	**13.62** (7.23)	**26** (6.65)	**27.15** (6.42)	**28.21** (6.12)	**28.59** (6.21)	**34.28** (5.58)	**13.15** (7.53)	**0.21** (66.15)	**0.25** (36.29)	**24.11** (5.73)	**21.85** (6.19)	**25.96** (5.36)
C	**48.69** (10.04)	**40.47** (10.81)	**43.06** (10.76)	**46.42** (10.52)	**44.06** (10.76)	**45.30** (10.85)	**43.66** (10.40)	**39.26** (10.22)	**52.17** (9.64)	**57.11** (10.24)	**53.57** (13.66)	**56.92** (10.26)
O	**2.80** (13.25)	**2.43** (13.58)	**2.43** (13.60)	**2.50** (13.68)	**2.80** (13.30)	**2.11** (14.05)	**2.47** (13.53)	**1.17** (53.93)	**1.64** (18.03)	**2.10** (14.42)	**3.04** (12.02)	**2.94** (12.24)
S	**0.02** (78.61)	**0** (99.99)	**0.02** (83.71)	**0.02** (87.71)	**0.04** (71.89)	**0.01** (99.99)	**0.01** (99.99)	**0.03** (74.99)	**0.04** (72.19)	**0** (99.99)	**0.02** (81.49)	**0.03** (76.29)
Na	**1.82** (14.60)	**1.87** (13.79)	**1.52** (13.85)	**1.36** (13.59)	**1.82** (12.42)	**0.83** (14.84)	**1.88** (16.18)	**1.55** (21.63)	**1.40** (19.12)	**0.45** (22.47)	**1.48** (13.59)	**0.85** (14.35)
Cl	**0.01** (82)	**0.02** (75.42)	**0.03** (71.22)	**0.02** (71.33)	**0.03** (69.37)	**0.02** (78.24)	**0.02** (73.38)	**0.01** (99.99)	**0.02** (81.61)	**0** (99.99)	**0.02** (77.32)	**0.01** (86.18)
Possible Phases*	**FeAl(C_2,O)**	**FeAl(C,O)**	**FeAl(C_2,O)**	**FeAl(C_2,O)**	**FeAlC_2**	**FeAl(C_2, O)**	**FeC (Al,O,Na)**	**Substrate**	**Substrate**	**FeAl(C_3,O, Na)**	**FeAl(C_3,O, Na)**	**$FeAl_2$(C_3,O, Na)**

* The possible phases were estimated according to the EDS elementary spots analysis.

The cross-sectional structure of HDA carbon steel half immersed in the molten salt mixture for 72 h is shown in Figure 57(a,c). Both sections exhibit similar characteristics. Reaction products accumulated at the outermost layer appear in black-grey and are indicated by black arrows. A light, gray-colored zone (Layer B) emerges at the interface in both regions. Its thickness varies in both sections, non-immersed and immersed, from approximately 12.4 mm on average to approximately 12.45 mm. The flake-like structure is observed in both regions (see Figure 57(b,d)). There is also an apparent cracked line, as highlighted in Figure 57(b,d) and reported in Table 11. An EDS spot analysis was also conducted.

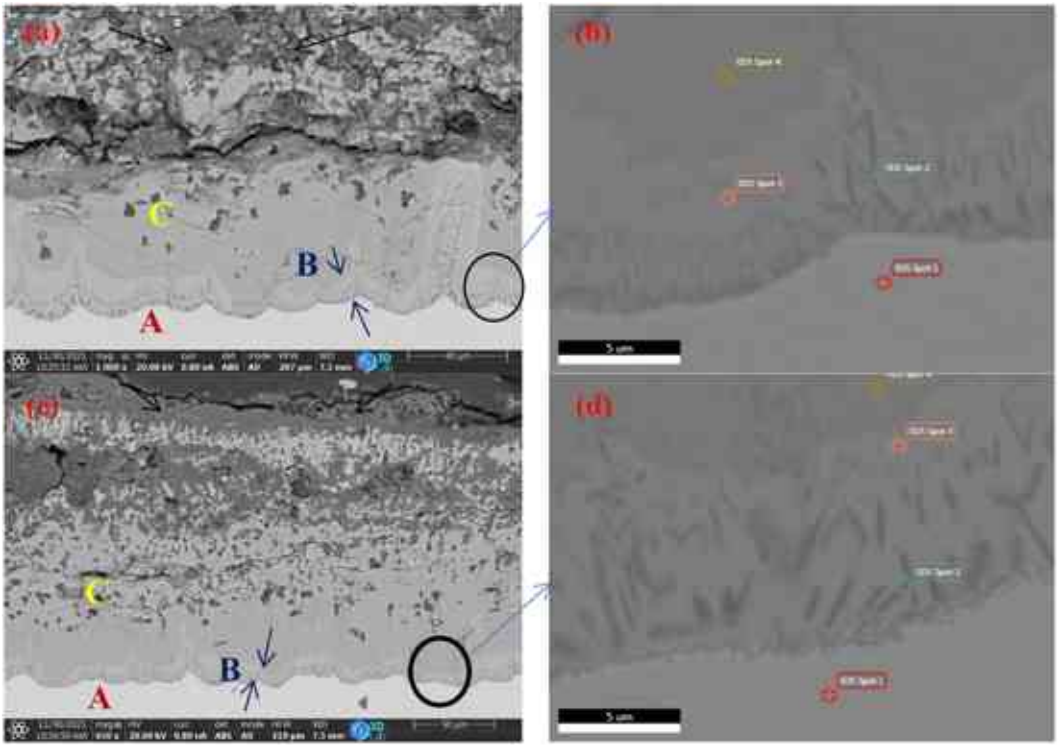

Figure 57. PFIB-SEM images showing the structure that developed at the interface between the substrate and the intermetallics layer during the exposure period of 72 h (a) and (b) non-immersed section exposed to hot air; (c) and (d) immersed in the molten salts.

Table 11. Data measured by EDS analysis at the spots depicted in Figure 57(b,d).

Elements in At. %	Non-immersed				Immersed			
	Points				Points			
	1 (Err. %)	2 (Err. %)	3 (Err. %)	4 (Err. %)	1 (Err. %)	2 (Err. %)	3 (Err. %)	4 (Err. %)
Fe	**68.02** (1.89)	**23.74** (2.17)	**35.72** (2.10)	**24.29** (2.19)	**59.24** (1.88)	**15.94** (2.22)	**23.90** (1.99)	**16.25** (2.15)
Al	**1.25** (16.28)	**38.08** (6.12)	**38.20** (6.72)	**49.01** (5.96)	**0.67** (23.69)	**31.62** (5.62)	**26.88** (6.42)	**33.25** (5.65)
C	**20.34** (12.87)	**32.60** (12.30)	**20.24** (13.79)	**23.06** (13.63)	**32.52** (11.32)	**49.12** (11.03)	**42.79** (11.10)	**45.99** (11.09)
O	**3.31** (13.23)	**2.66** (14.51)	**0.87** (38.10)	**1.01** (27.43)	**1.70** (18.57)	**1.33** (19.74)	**2.68** (14.05)	**2.25** (14.63)
S	**0.11** (67.98)	**0.13** (64.85)	**0.17** (63.84)	**0.05** (80.73)	**0.01** (99.99)	**0** (99.99)	**0.05** (72.58)	**0** (99.99)
Na	**4.34** (16.14)	**0.36** (67.32)	**0.92** (26.97)	**0.77** (22.96)	**3** (16.87)	**0.33** (31.16)	**1.89** (13.77)	**1.11** (14.78)
Cl	**0.03** (85.65)	**0.01** (99.99)	**0.10** (65.63)	**0.02** (96.90)	**0.02** (91.47)	**0.02** (82.80)	**0.01** (93.18)	**0.01** (92.56)
Possible Phases*	Substrate	$FeAl_2$ (C,O)	FeAlC	$FeAl_2$ (C,Na)	Substrate	$FeAl_2$ (C_2,O)	FeAl (C_2,Na)	$FeAl_2$ (C_3,O, Na)

* The possible phases were estimated according to the EDS elementary spots analysis.

Considering the error values, it can be stated that the EDS measurements were conducted primarily in the gray emergent layer (Layer B) of both sections to represent the Fe–Al–C–O system. Although atomic percentages of the constituent elements vary in both areas, the C content in parts kept in contact with molten salt is higher than in other regions. As for O, the

concentrations are similar, but the concentrations of Fe and Al are significantly lower than in the section in contact with molten salt.

Moreover, the structure of carbon steel C45 (substrate) is also evaluated to reveal the influence of substrate components, such as the high carbon content. Therefore, the probability of C diffusion outward is high during elevated temperature exposure, which can negatively impact the protective layer. As seen from the optical microscope image in Figure 58 of the HDA sample after 24 h in molten salt at 700 °C, the pearlite structure expanded in size when the cementite disintegrated.

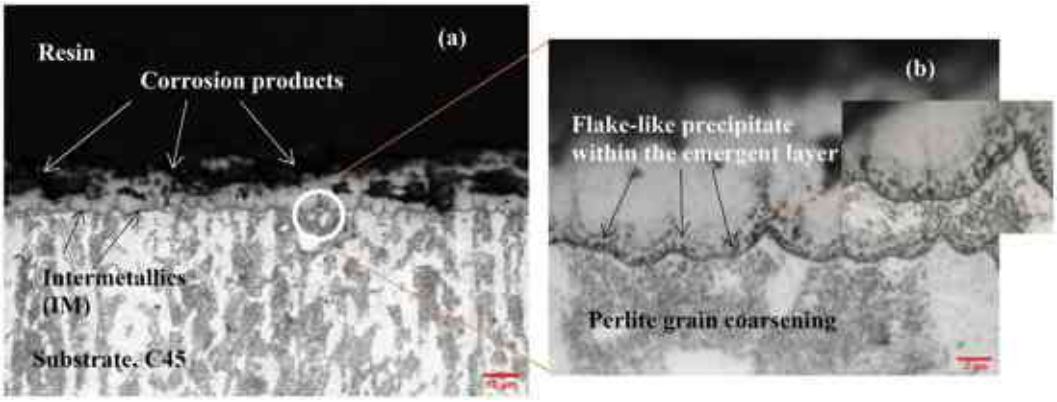

Figure 58. Optical microscope image of HDA half immersed at 700 °C in molten salt with exposure time equals of 24 h; (a) cross-sectional view of the HDA after exposure, (b) the marked portion enlarged to highlight the precipitate of flake-like structure within the emergent layer and the pearlite grain growth/coarsening.

Afterward, the dissolution of the cementite will be followed by outward diffusion of carbon, which contributes to the formation of the flake-like structures that appear within the emergent layer.

The HDA carbon steel specimens were exposed to melted salt electrolytes in this experimental investigation. In comparison to high-temperature corrosion in air, corrosion processes in the presence of molten salts will become increasingly complex and will incorporate some electrochemical processes along with many physical processes and direct chemical reactions. Furthermore, corrosion exposures of this complexity involve different and changing combinations of phases (solids, liquids, gases) with varying chemical compositions. In our extensive experimental study, we made important observations about a system closely related to reality. It was evident that our HDA carbon steel C45 samples held at 700 °C for 8, 24, and 72 h half immersed in molten salts (NaCl, Na_2SO_4) suffered more serious surface degradation as a result of physical attack (such as dissolution, penetration, stress generation, etc.) coupled with quite complex chemical and electrochemical reactions with the highly corrosive constituents of the tested molten salt mixture and those of the hot air.

In such a situation, under continuous exposure to those highly corrosive substances at high temperatures, the formation or regeneration of a highly protective aluminum oxide scale must

have been considerably hindered. Moreover, the adherence and partial detachment of the scale layer were influenced by many factors. For example, pores and discontinuities appeared on the top surface exhibited in Figure 52, which could originate from several factors, like stress generation and propagation within the scale layer, this being also controlled by creep deformation [117,118]. Based on the results of the EDS spot analysis displayed in Table 11, it can be concluded that the formation of a sound and protective Al_2O_3 scale was greatly impeded. As reported elsewhere [118,119], thermal expansion differences can cause internal stresses leading to cracks developing between the substrate and the intermetallic phases (FeAl, $FeAl_2$, and Fe_2Al_5). According to Wang and Badaruddin [120], hydrogen dissolution into alumina can increase Al^{+3} cation vacancies, allowing Fe^{+2} to diffuse out and form iron oxide due to the high mobility of metal cations [121-123]. The presence of Fe at the top surface could also be detected via EDS in our case. Similarly, Na^+ cations from the salt melt could migrate through vacancies in the scale, followed by other elements (such as S and Cl), presumably replacing hydrogen or moving through interstitial defects. And, indeed, it was possible to detect all of these elements even in the inner Layers B and C, as shown in Figure 58 and recorded in Table 11 for the corrosion exposure period of 72 h. In our studied system a chloride-sulfate-type molten salt can be characterized by the formation and/or dissolution of some metal oxides, which will increase the melt alkalinity [122,123], and influence both the physical and chemical aggressiveness of the melt in contact with the protective alumina scale, which, otherwise, is constantly changing in its chemical composition and physical characteristics. Iron diffused from the HDA substrate can form iron oxides and dissolve in the melt, which was also detected in the testing crucible. Moreover, the hygroscopic property of NaCl combined with the dissolution of O_2 in the melt will also increase the corrosion rate [17] by enhancing the chemical dissolution rate of the alumina scale through the formation and migration of the of O^{2-} ions in the salt melt, followed by converting the Al_2O_3 scale to more soluble aluminates, as demonstrated by Equation (15).

$$Al_2O_3 + O^{2-} \rightarrow 2AlO_2^- \qquad (15)$$

This means that the chemical dissolution attack of the O^{2-} ions present in the melt can destroy the solid alumina protective film at the 'weakest' local points. All in all, the molten salt blend triggering such or similar heterogeneous reactions and converting and dissolving portions of the protective layer did indeed bring about the formation of different surface corrosion products seen as dispersed all over the surface in Figure 53.

The carbon content of steel C45 is high, and this carbon may likely diffuse outward with iron (Fe) during the HDA process [88,89]. It has been reported that carbon diffusing outward can interstitially exist within the iron aluminides solid solutions (Fe–Al, IM zone) and can form carbide precipitates within the IM zone and even within the aluminum topcoat. In addition, at the given higher temperatures, the perlite grains in the substrate steel C45 can also begin to grow and thus expand, resulting in the decomposition of the cementite (Fe_3C) phase followed by the same type of carbon diffusion as happens during certain heat treatments of steels known

as surface decarburization [124]. Cementite decomposition was also observed in our case (see Figure 58), and the outward diffused carbon formed flake-like precipitates within the emergent layers throughout all three exposure periods, shown in Figures 55, 56, and 57. A further outcome of the outward diffusion of carbon is that it can react with diffused oxygen, forming different types of carbon oxides (Table 12) and causing inner cracks and holes. In addition to oxygen, as the aggressive environment contains chlorine and sulfur compounds, this also potentially increases the corrosion rate [125,126].

The induced degradation mechanism can start with the formation of tiny surface discontinuities, cracks, holes, and cavities at the top, opening migration routes for the aggressive substances, e.g., for the chlorine to diffuse inward and produce chloride compounds of, for example, iron and aluminum chlorides (Table 12). As these chloride compounds are volatile, they can migrate also to the external surface where the partial pressure of O_2 is high (in the hot air) and the thermodynamic probability of forming oxides is also high, presuming, for example, the action of the so-called oxychlorination corrosion cycle [127]. As in our studied system the EDS results confirmed the presence of iron even in the outermost layers, it is possible that stable spinel-type compounds (like FeO-Al_2O_3, Table 12) could also form after more prolonged exposure of the aluminized steel C45. In addition, the EDS map showed that sulfur was present deep inside the corroded HDA samples as time progressed. Finally, the aluminized inner zones also exhibited low chlorine levels, most likely due to the high volatility of chlorides (Table 12).

Table 12. Selected fundamental thermochemical data for the given system's most relevant simple oxide and chloride compounds.

Substance	Melting point, K	Boiling point, K	[a]ΔG° at 973 K, kJ/mol	[a]ΔG° kJ/ per one mol of O or Cl
CO	Gas at ambient temp.	–	−197.9	−197.9
CO_2	Gas at ambient temp.	–	−395.8	−197.9
FeO	1646	3687	−200.8	−200.8
Fe_3O_4	1870	–	−800.6	−200.1
Fe_2O_3	1838	–	−565.9	−188.6
Al_2O_3	2327	3273	−1370.0	−456.6
FeO·Al_2O_3	2073	–	−1618	−404.5
$FeCl_3$	577	589	−229.2	−76.4
$AlCl_3$	466	720	−511	−170.3

[a]The formation of standard Gibbs energies of the given chemical compounds was calculated based on the HSC Chemistry 5.11 software package database.

In connection to the above discussion, as shown in Table 12, the standard Gibbs energy results obtained with HSC software at 700 °C are in accordance with the EDS elemental spots results. However, the overall examination results show that the oxygen appears to be the dominant non- metallic element found in the corroded samples. Therefore, the focus was also placed on the possible formation reactions of the oxide compounds and the compilation of the standard Gibbs energies of some other relevant compounds at 700 °C (Table 12). Among the oxides is aluminum oxide (see data in the right-side column in Table 12), which is the most stable. Therefore, its protective feature is maintained as long as its formation and regeneration (the so-called self-healing effect) is not much impeded. But as has been presented and discussed above,

such a protective feature does not mean zero rates of material degradation in such extremely harsh environments. Still, the aluminum content in the surface layers (in the form of aluminides and top Al) can effectively mitigate this hot air and/or molten salt type high-temperature corrosion, many important characteristics and details of which could be explored and highlighted in this research.

4.3 Oxidation resistance investigation of HDA carbon steel C45

4.3.1 Experiments and methodologies

The HDA carbon steel C45 samples have been evaluated by means of two approaches to test their suitability for use at high temperatures as structural materials. Temperature and time are altered throughout the examination, and corrosion kinetics and activation energy are determined according to the weight change before and after the exposure period and for each specific temperature. Following that, the samples were metallographically examined.

4.3.1.1 Corrosion test

The corrosion experiment was conducted in hot air. Prior to placement in the electrical furnace, the sample was weighed and exposed to temperatures ranging from 700 to 1000 °C for 8, 24, and 72 h. All procedures were strictly followed in accordance with ISO-17245-2015. The corrosion rate was determined based on the mass change using non-continuous exposure, high-temperature testing. A precise electronic scale balance was used to weigh the specimen before and after the exposure period.

$$\Delta m = m - m_i \qquad (16)$$

Where: m = mass of the specimen after exposure (g); m_i = initial mass of the specimen before exposure (g).

Moreover, the mass difference (Δm) is divided by the surface area to find the mass change per unit area and plotted versus each time set for every single temperature. According to the parabolic law Equation (17)

$$(\Delta m)^2 = K_p * t \qquad (17)$$

Where: K_p = parabolic rate constant ($\frac{g^2}{cm^4} * h^{-1}$); t = time of exposure in hours.

The activation energy been calculated based on the square weight change and parabolic rate constant used elsewhere [128].

4.3.2 Results and discussions

4.3.2.1 Oxidation kinetics

Oxidation resistance tests were conducted on HDA carbon steel C45 specimens at high temperatures between 700 to 1000 °C for three different exposure periods: 8, 24, and 72 h. The

evolution of the oxide scale was charted in Figure 59, displaying the change in weight per surface area versus exposure time.

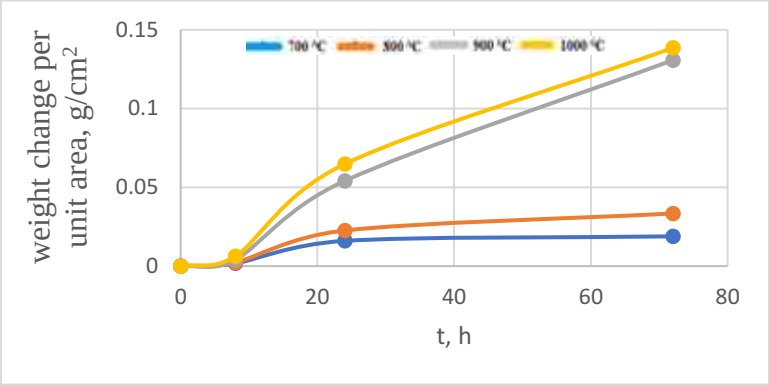

Figure 59. Evolution of oxide scales as a function of weight change per unit area versus time between 700 to 1000 °C.

Between 24 and 72 hours of exposure at 700°C, the scale formation appears to follow a steady state condition without any significant changes. The same pattern is observed for the 800°C exposure, with a slight change in the straightness. At these two temperatures, the HDA specimens exhibit proper resistance to hot air. However, at 900°C and 1000°C, a sharp increase in weight gain is observed between 24 to 72 hours. This indicates that at high temperatures, the aluminized carbon steel C45 is more likely to experience weight gain, suggesting a higher probability of degradation.

During the initial exposure periods, the growth of oxide scale follows a parabolic kinetic, where diffusion behavior plays a crucial role. The oxidation rate at different temperatures during exposure periods is presented in Table (13) as (g^2/cm^4) versus exposure duration in hours (see Figure 60), which was determined using Equation (17).

Table 13. Growth oxidation kinetic rate for the HDA carbon steel C45 at different temperatures.

Temperature, °C	700	800	900	1000
K_p, $g^2/cm^4 . h^{-1}$	4.73914×10^{-6}	0.00176985	0.004203541	0.00408665

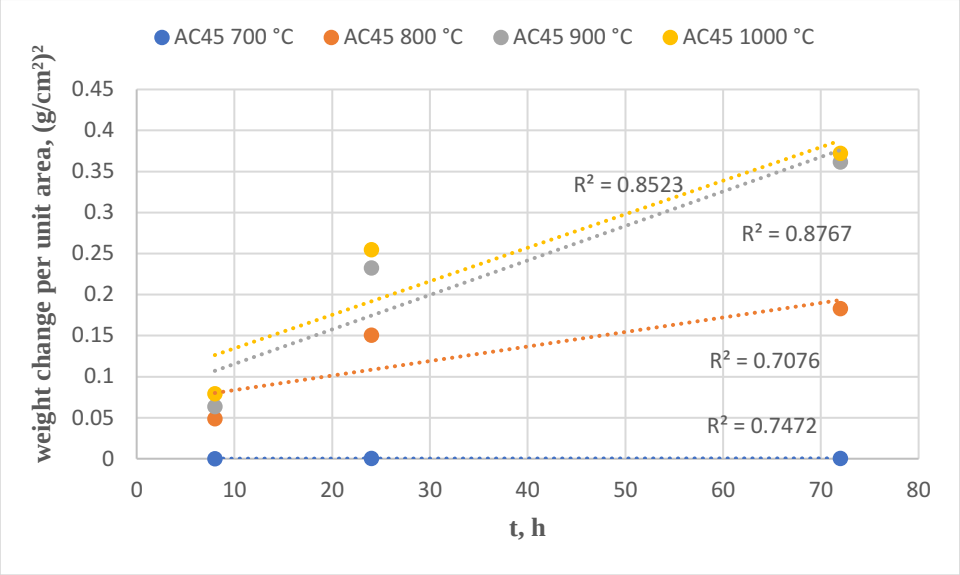

Figure 60. Oxidation kinetics as a function of weight change per unit area versus time according to equation 17.

It can be inferred from the results that the oxidation kinetic rate at 900 and 1000 °C is significantly higher than that at 700 °C for HDA carbon steel C45. Additionally, the activation energy of the steel has been determined using the Arrhenius relation (as shown in Figure 61) and has been reported in Table 15.

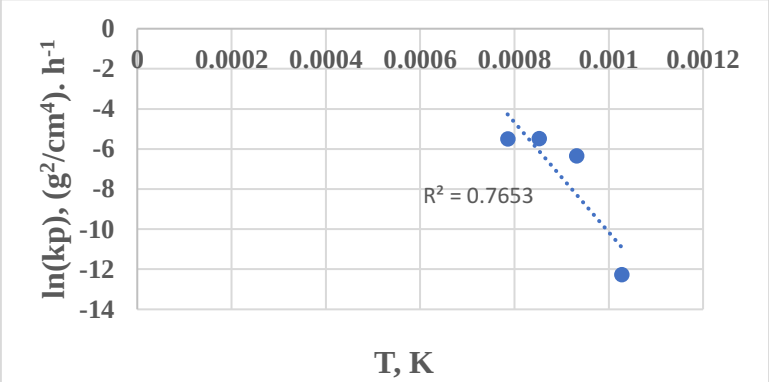

Figure 61. Activation energy as a function of square weight change per unit area vs. temperature used.

Table 14. Activation energy of aluminized C45.

Corrosion Conditions	Activation energy, E_a (kJ/mol) ≈
HDA Carbon steel C45 exposed to hot air between 700-1000 °C	**228**

4.3.2.2 Surface morphology

During the first 8 h of exposure, HDA carbon steel C45 samples showed various surface appearances that changed with the temperature. Figure (62) displays these distinct

morphologies. At 700°C, the top surface displayed a crystal-like structure consisting of silicon oxide and a nodule-like morphology (Cu-Si-Al-Fe-O), while the base was mainly aluminum oxide with very little iron content. As the temperature increased to 800°C, most of the morphology changed into a thin crust spread over the sample's surface, mainly composed of aluminum oxide. However, the coating surface remained compact with no cracks even after exposure to hot air at 700 and 800°C. At 900°C, a whisker-like morphology appeared on the outermost surface of the HDA sample, embedded and parallel to the surface. Nearly all of these were aluminum oxides dispersed across the surface with minor amounts of iron.

When the surfaces of HDA carbon steel C45 were heat-treated at 1000°C, a whisker-like pattern formed perpendicular to the surface. The analysis of the EDS spots confirmed that the predominant component was aluminum oxide containing a few variable amounts of iron. No cracks were detected at 900 or 1000°C, and the surfaces still maintained their compactness.

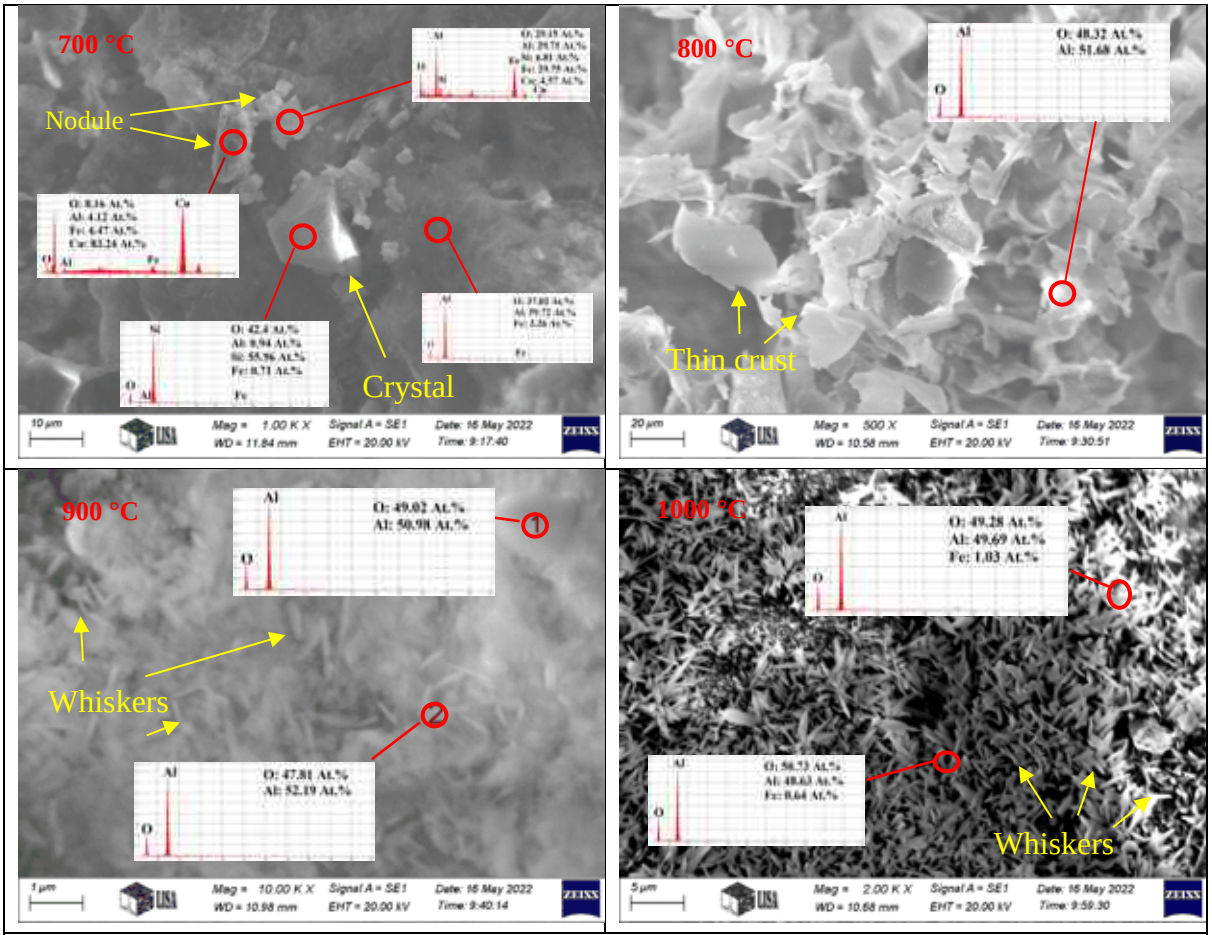

Figure 62. HDA carbon steel C45 surface morphology after being held inside an electric furnace for 8 h at four different temperatures, the EDS spots were conducted on the identified locations.

For the 24 h exposure periods, please refer to Figure (63) for the results at different temperatures. At 700°C, the surface morphology shows a whisker-like form made up of aluminum oxide. At 800°C, the morphology changes to dense nodules clustered together with

some cracks and grooves appearing on the surface. A small amount of iron was detected. At 900°C, a higher concentration of iron was detected, appearing as white particles spread along the top surface. Iron is also present as tiny nodules creating colonies combined with Al and O and spread along the top surface. Cracks and cavities were also detected. At 1000°C, the concentration of iron significantly increased and reacted with aluminum and oxide, resulting in the formation of distinct, white particles with a thorn-like morphology that spread extensively over the surface.

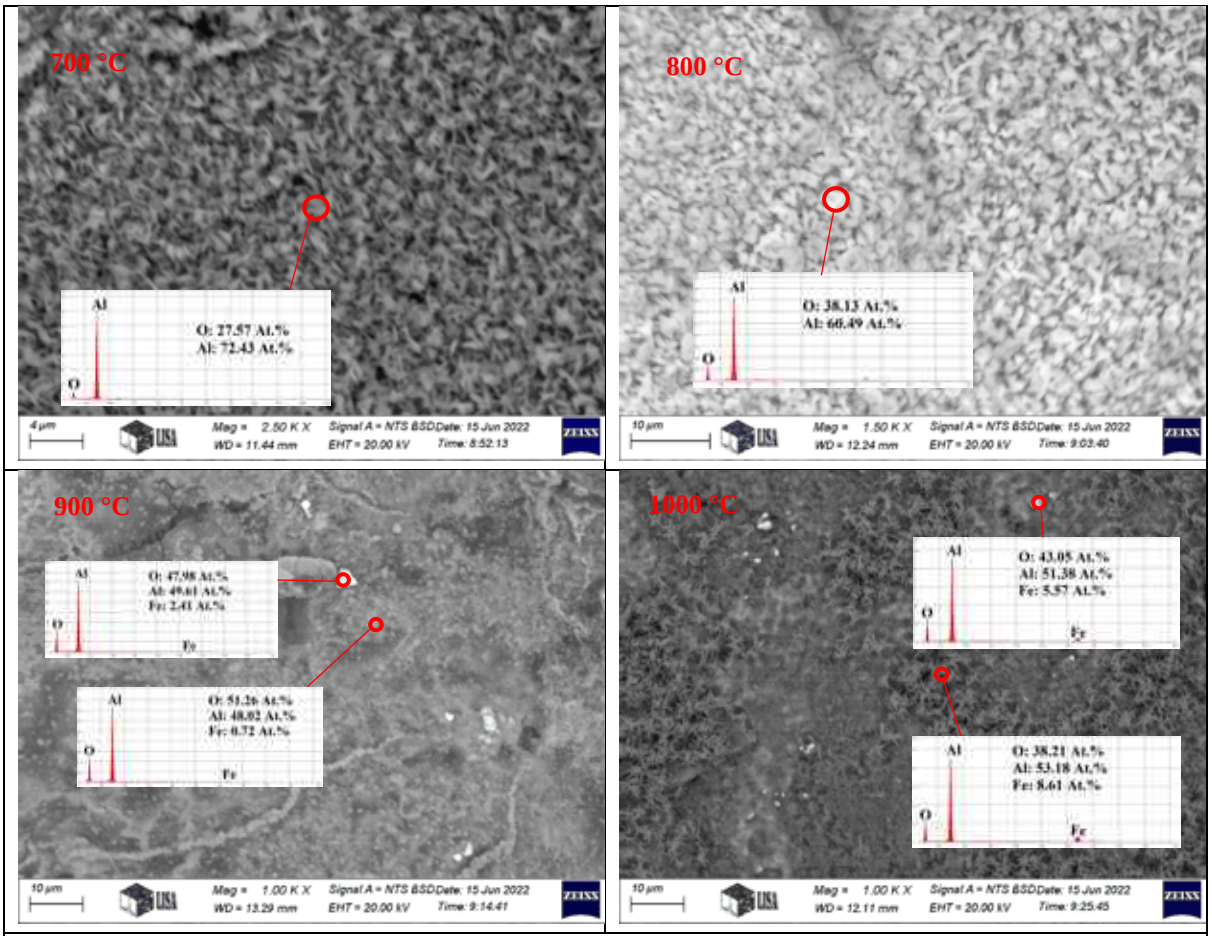

Figure 63. HDA carbon steel C45 surface morphology after being held inside an electric furnace for 24 h at four different temperatures, the EDS spots were conducted on the identified locations.

Figure (64) illustrates the surfaces of samples held inside an electrical furnace for 72 hours at a temperature of 700°C. The sample surfaces show fine particle dispersion, with aluminum as the dominant element (approximately 68-74 At. %) and iron with a range of 10-28 At.%, and a small content of silicon. Porosity is visible in the samples.

The HDA sample at 800°C exhibits finer particles compared to previous samples, which change to coarser ones that spread over the surface. Iron is represented in high oxygen and manganese content, while the pores are still visible.

After 72 hours of exposure to high temperatures (1000°C), the surface of HDA carbon steel C45 shows a unique reef-like structure dispersed over its surface. The severe temperature exposure is evident from cracks and pores distributed over its surface, and spalling scale can be seen too. The magnitude of iron content is high, and oxygen is present. Only a small amount of manganese content could be detected.

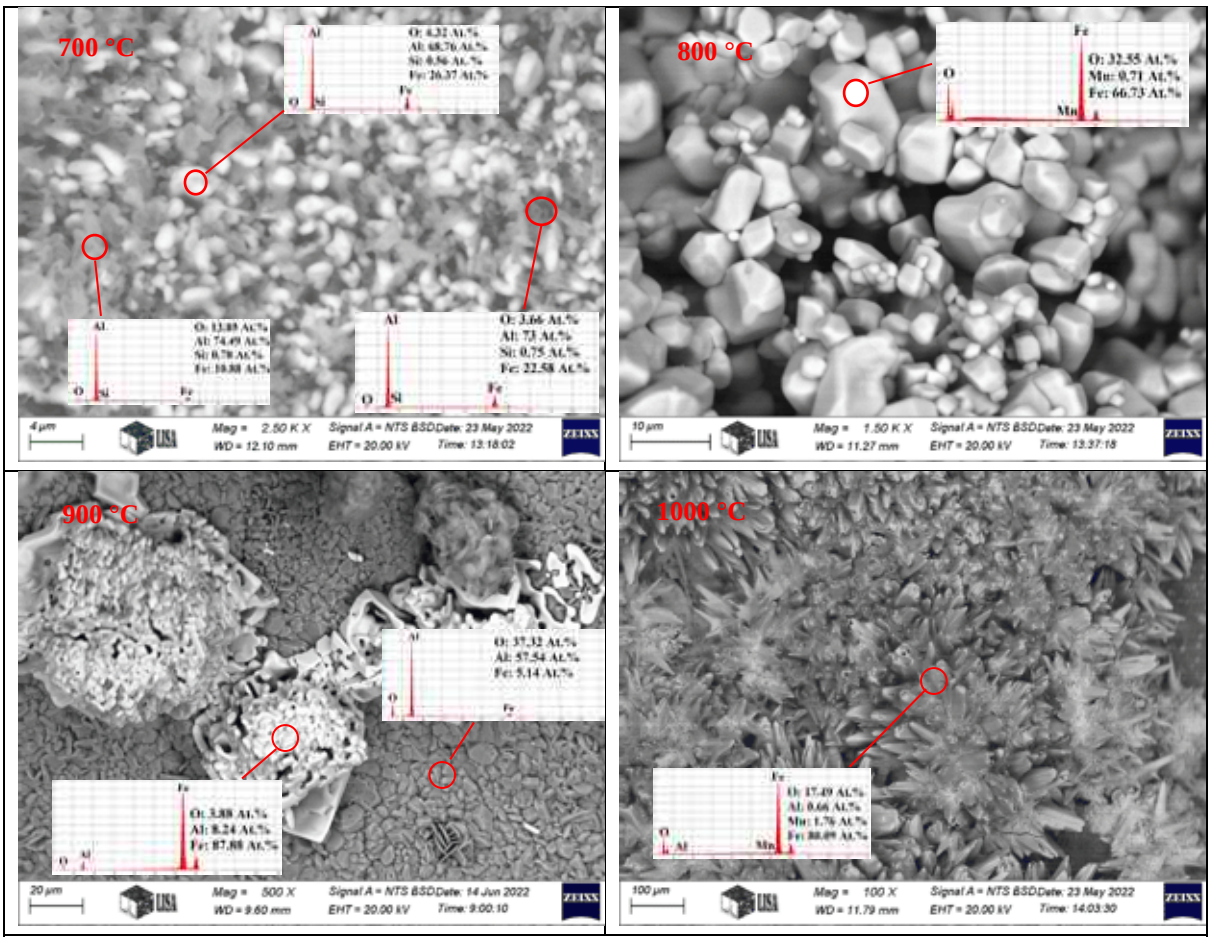

Figure 64. HDA carbon steel C45 surface morphology after being held inside an electric furnace for 72 h at four different temperatures, the EDS spots were conducted on the identified locations.

4.3.2.3 Structure characteristics

The samples were ground and polished for cross-sectional investigation. The first set was subjected to different temperature ranges for 8 h, as shown in Figure (65). It is well-known that heat treatment of hot dip aluminized induces further interdiffusion between the chemical species. The finger-like structure no longer exists and more pores are seen near the surface. In contrast, a new interdiffusion layer is developed at the substrate and coating interface. The selected area A and B in Figure (65), exposed to 700°C, have been enlarged and shown in Figure 66. A black spot appears, trapped at the upper part close to the surface, as depicted in Figure 66(A). The EDS spot analysis reveals that it is a kind of Fe-Al-C system, a type of carbide surrounded by a matrix of Fe-Al grey color. According to the EDS results, the possible phase could be $FeAl_2$. Figure 66(B) shows the lower section where the oxide couldn't be

detected at the substrate. The new interdiffusion layer probably consists of FeAl phase with a flake-like structure dispersed in it. EDS analysis of the layer above the new interdiffusion layer shows approximately the same content percentage as depicted in Figure 66(A). Therefore, the same phase, $FeAl_2$, is likely present.

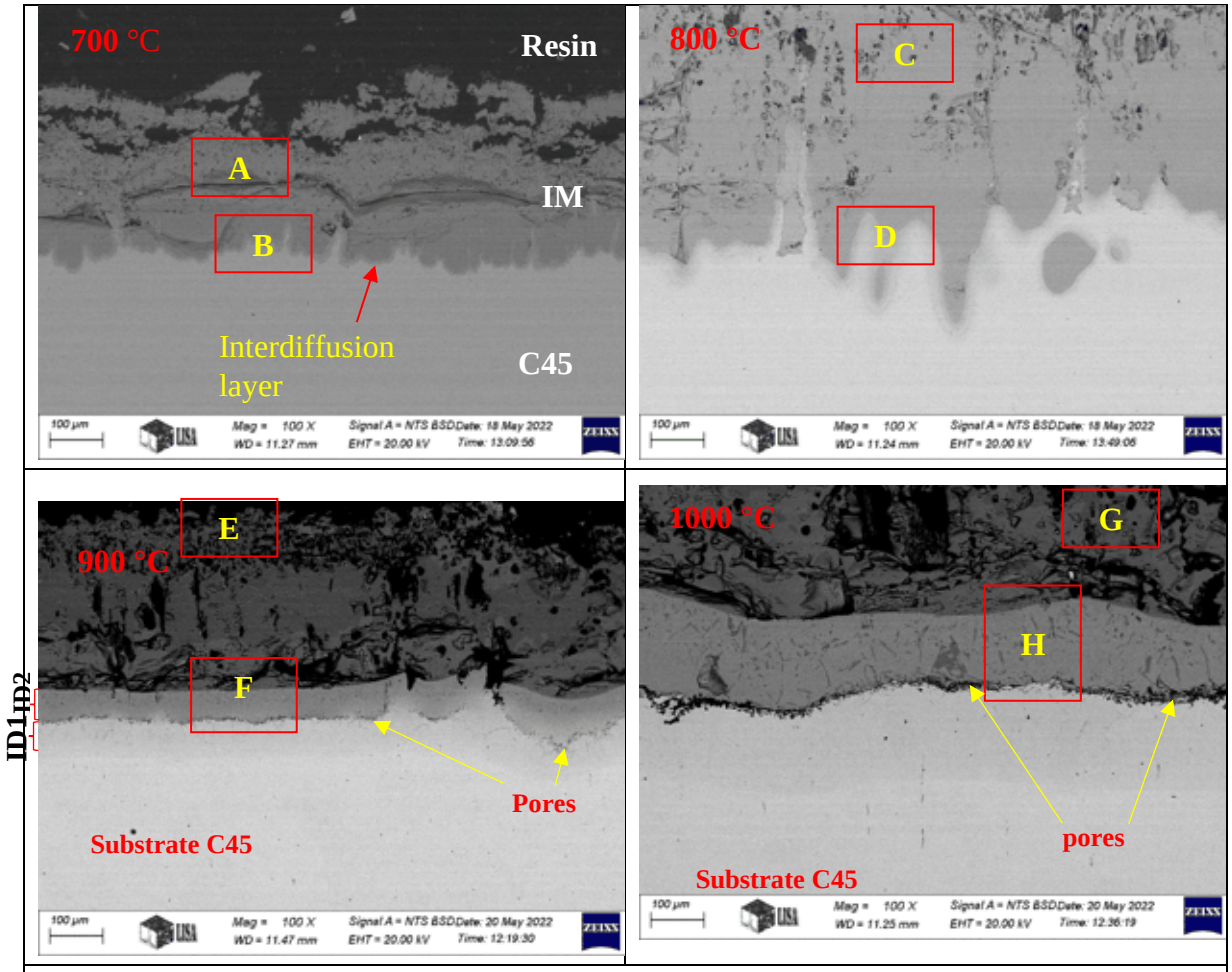

Figure 65. The SEM images show the cross-sections of the HDA samples held for 8 h inside an electric furnace at different elevated temperatures as indicated in the images.

In Figure (65), the sample held at 800 °C has the same structure as the one held at 700 °C. The closer views in Figure 73 (C) and (D) have approximately the same compositions. However, at 900 °C, due to the high temperature, depletion is clearly visible. The structure consists of three distinct layers: interdiffusion layer one (ID1), interdiffusion layer two (ID2), and the outer/topcoat layer. A closer look at the topcoat layer in Figure 66 (E) reveals a base matrix consisting of Fe-Al, represented by the possible phase $FeAl_2$, appearing in gray and light gray colors. Spread along this layer is a dark spot-like feature consisting of Fe-Al-O, with visible pores. A closer look at the interfaces of the interdiffusion layers (ID1), (ID2), and the top layer in Figure 66(F) shows the Fe-Al-O system detected in the top layer close to the ID2 layer. In the ID2 layer, Fe-Al-Mn-O is detected as a matrix with black flakes spread across the upper part of this layer, which is comprised of Fe-Al-C. At the interdiffusion layer (ID1), the

aluminum content increases to around 20 At.% with an increase in oxygen content. Vessel-like structures can also be seen, representing a possible phase of FeAl with a one-to-one ratio.

At 1000 °C, as shown in Figure 65, the (ID1) and (ID2) layers become thicker compared to the 900 °C exposure temperature. The pores also become larger. In the top layer, a closer look in Figure 66(G) shows more and larger pores/cavities. The EDS spot analysis shows that this layer consists of Fe-Al with possible phase $FeAl_2$. Figure 66(H) at the interface between the top layer and (ID2) shows the presence of Fe-Al-C. The ID2 layer consists of two systems: Fe-Al-O as a matrix and Fe-Al represented by possible phase $FeAl_2$ spread in a particle/flake-like shape. The ID1 layer completely becomes Fe-Al-Mn-O, with aluminum content less than 20 At.% and an increase in oxygen content.

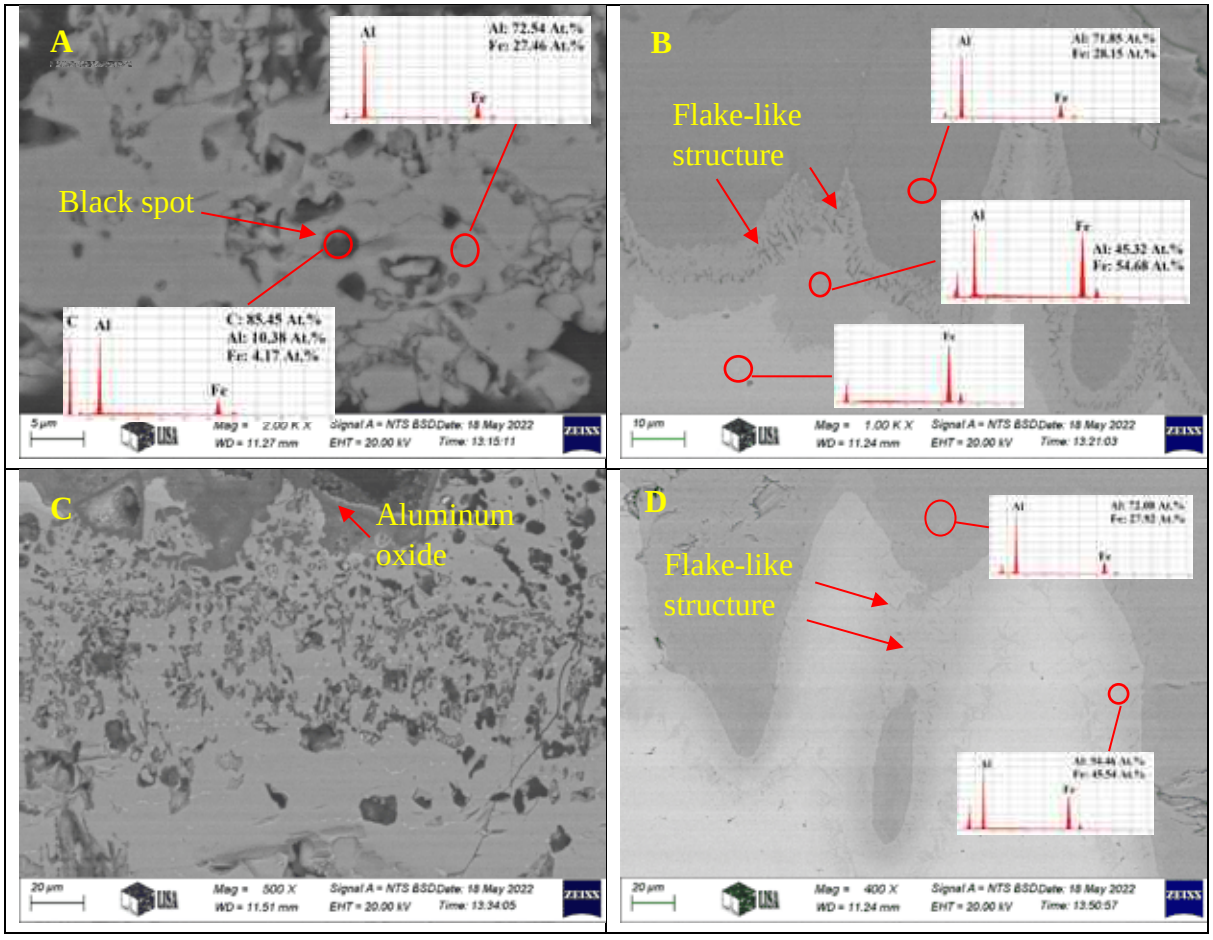

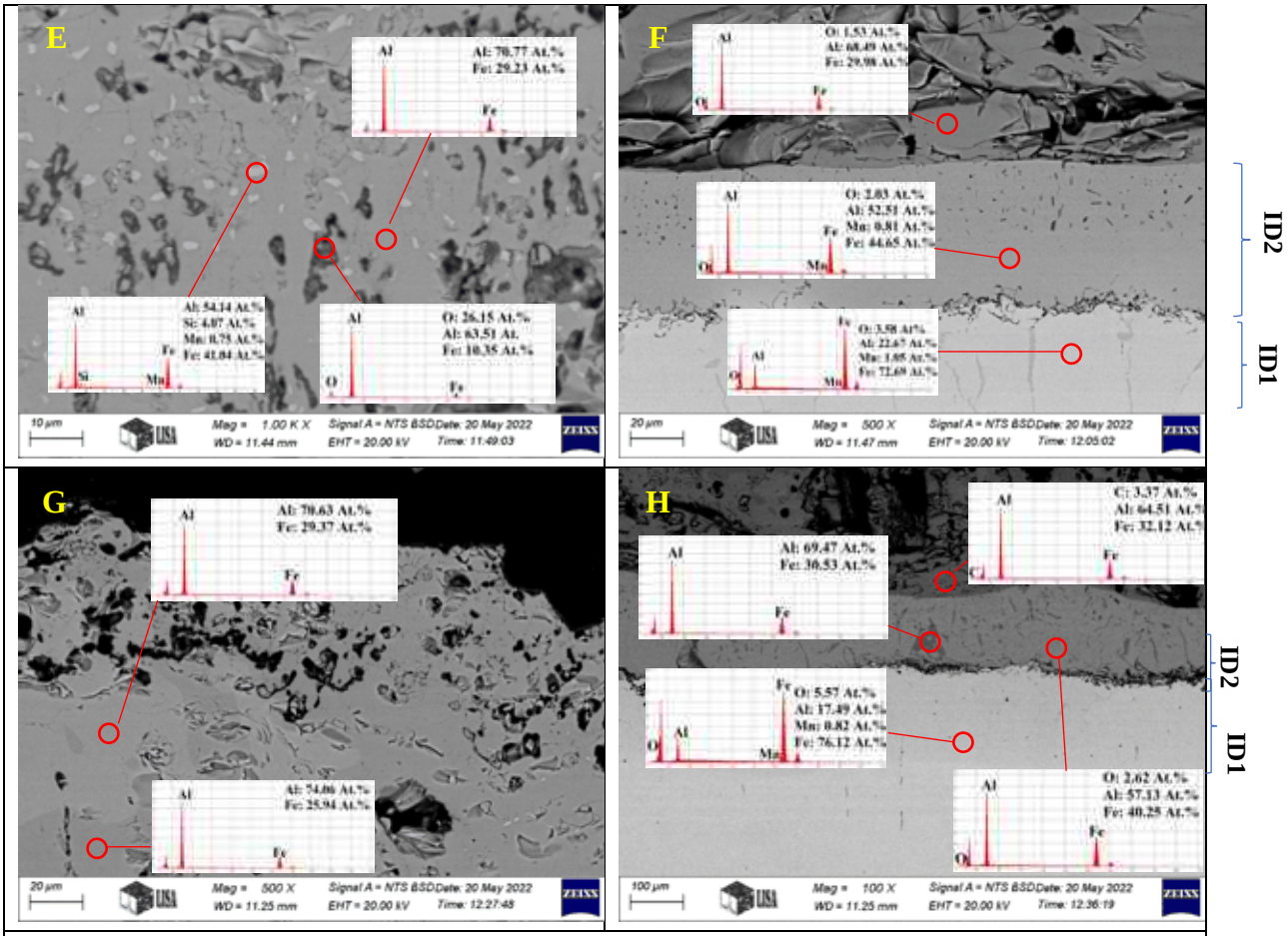

Figure 66. Represent the identified area in figure (72) for a period of 8 h and the four temperatuers combined with EDS spot analysis.

Figure (67) displays the cross-sectional view of oxidized samples held for 24 hours at different temperatures. It is evident that the structure of the sample held at 700°C for 24 hours is almost identical to the one held at the same temperature for 8 h. Upon closer examination of Figure 68(A), it is indisputable that the top layer consists of Fe-Al-O, with a discernible phase $FeAl_2$ and a minute amount of oxygen content. Figure 68(B) irrefutably shows that the emerging layer consists of Fe-Al-C, with pores initiated at the top layer. Meanwhile, the sample held at 800°C Figure 67 is the same as the one held for 8 h, except for more cavities or pores. On closer inspection of Figure 68(C), it is crystal clear that the top layer consists of Fe-Al-O, with Si and Mn, while Figure 68(D) demonstrates that the composition of the interdiffusion layer consists mainly of Fe-Al, with minor content of (C, Ni, Mn). A vessel-like shape can be undeniably seen, extending toward the substrate, with the composition of the interdiffusion layer entrapped between the vessel-like shape consisting of (Fe-Al-O) and the composition of the vessel-like shape comprising of Fe-Al-C.

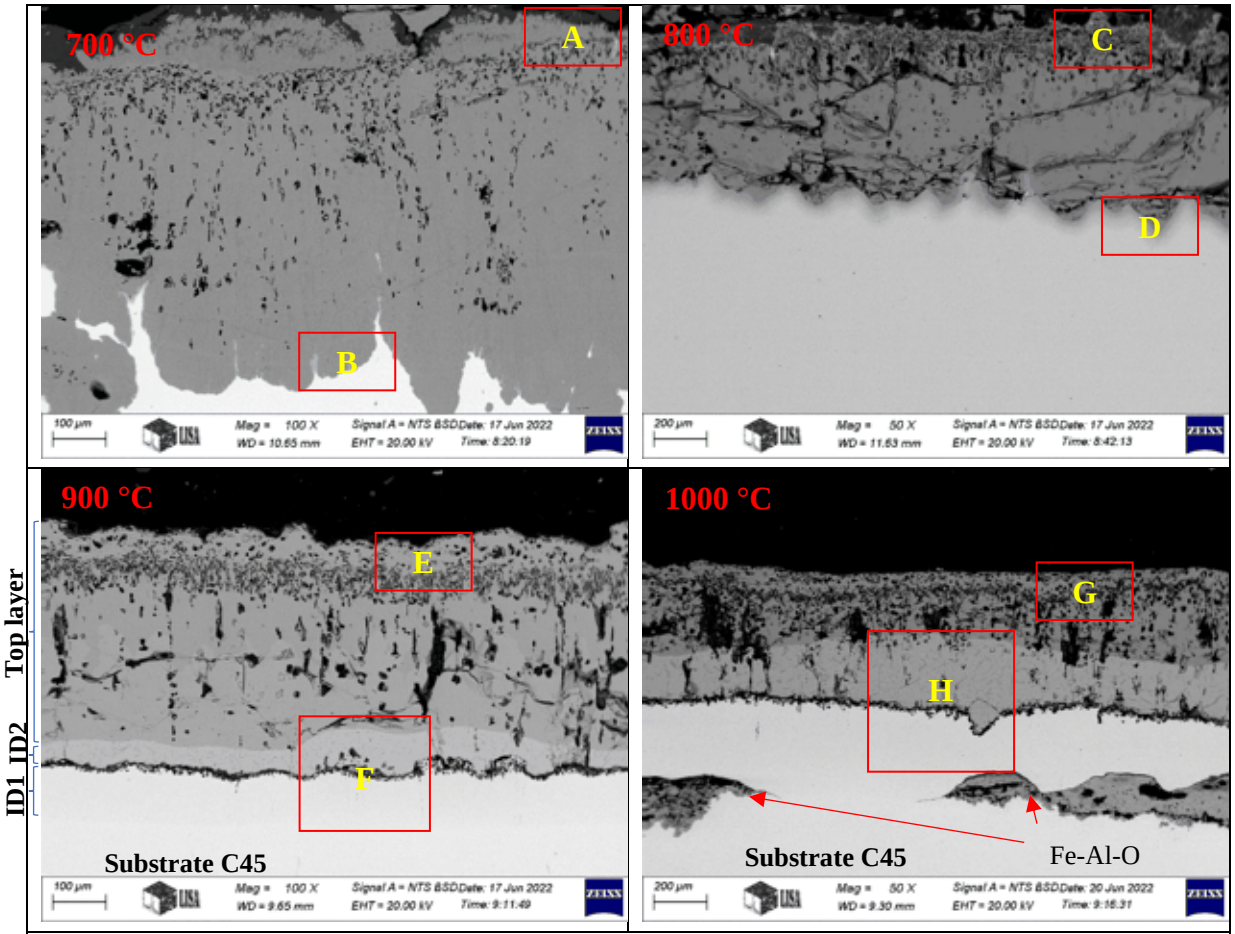

Figure 67. The SEM images show the cross-sections of the HDA samples held for 24 h inside an electric furnace at different elevated temperatures as indicated in the images.

In Figure 67, where the sample was held at 900°C for 24 h, there was a possibility of more degradation, which could appear as cracks at the top layer, as shown in Figure 68(E). The structure also displayed two interdiffusion layers, ID1 and ID2. A closer view of the selected area shown in Figure 68(F) revealed that the EDS spot analysis of the top layer adjacent to the ID2 layer consisted of a 1 to 2-mole ratio of Fe-Al, representing the possible phase of $FeAl_2$. The ID2 layer is comprised of a Fe-Al-C system with pores at the interface with the ID1 layer, while the ID1 layer itself consists of a base of Fe-Al with an Al content of around 17 At.%. Moreover, it had a vessel-like shape with a content of Fe-Al-C-O.

The cross-section of the sample held for 24 h at 1000°C is shown in Figure (67), revealing more severe deterioration at this temperature. The cross-section also displayed three distinct layers, namely the top, ID2, and ID1 layers, with a new island initiated at the interface between ID1 and substrate comprised of the Fe-Al-O system. A closer view of the top layer in Figure 68(G) showed more pores/cavities. The composition of the layer consisted of Fe-Al with a 1 to 2-mole ratio, most probably representing the $FeAl_2$ phase, while the ID2 layer consisted of Fe-

Al and a small amount of oxygen. Pores were seen at the interface with the ID1 layer, and the ID1 composition comprised Fe-Al with an Al content of around 10 At.%, and little Mn.

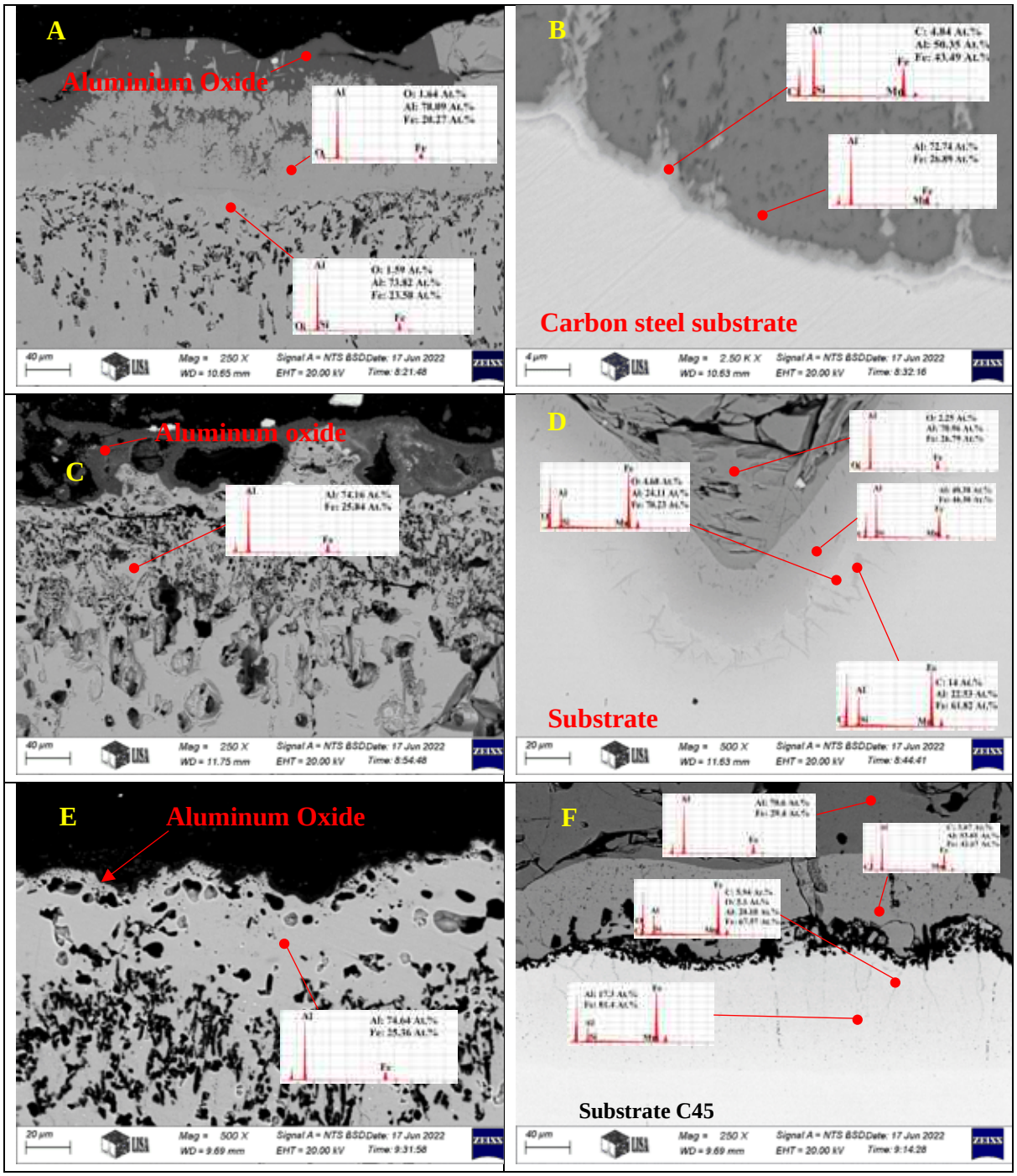

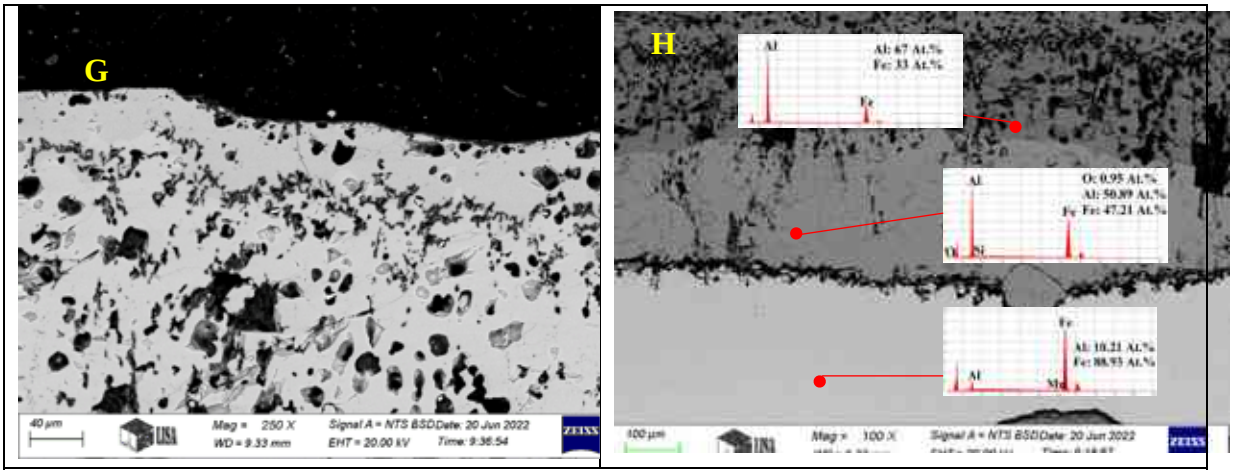

Figure 68. Represent the identified area in figure (9) for a period of 24 h and the four temperatuers combined with EDS spot analysis.

In Figure 69, we can see the cross-sectional view of the samples that were held for 72 h at different temperatures. The sample held at 700°C has a similar structure to the previous two samples that were held at the same temperature for 8 and 24 h. Figure 70(A) provides a closer look at the top layer of the sample. It consists of Fe-Al and a small amount of Si. The composition content indicates the possible phase of $FeAl_2$. There are tiny spots of light color along the top layer with a composition of Fe-Al-Si and a small amount of Mn.

In Figure 70(B), the interdiffusion layer appears in two distinct colors. A light gray color appears as an entrapped spread island with a composition of Fe-Al-C and a few Mn and Al contents around 23 At.%. It is within a base of Fe-Al and has a possible phase of $FeAl_2$. At 800°C, as shown in Figure 69, most of the aluminized coat layer transferred to an oxidized layer with islands of Fe-Al compounds spread along the oxidized layer, as shown in Figure 70(C). A closer view of the interface between the oxidized layer and substrate reveals a tiny vessel-like structure in Figure 70(D). It comprises Fe-Al-O.

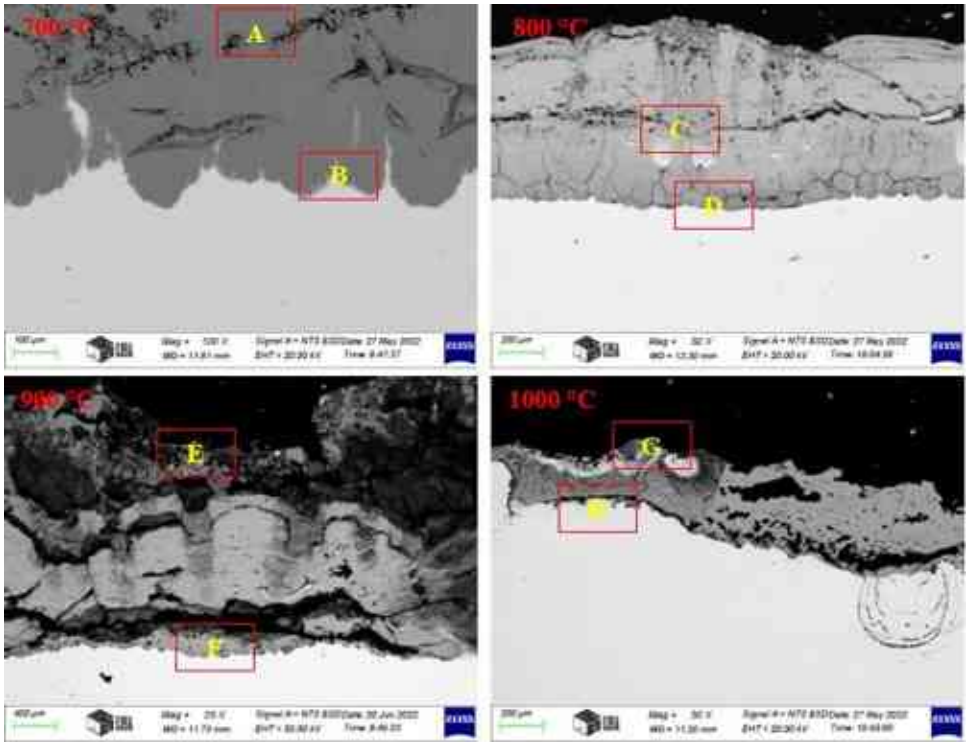

Figure 69. The SEM images show the cross-sections of the HDA samples held for 72 hours inside an electric furnace at different elevated temperatures as indicated in the images.

In Figure 69, the HDA sample that was held for 72 h at 900°C had the same structure as the one held at 800°C for the same duration. Upon closer inspection in Figure 70(E), we could see spots of Al mixed with iron or pure spots of Al. At the interface with the substrate, some spots were analyzed via EDS, which showed some substrate composition. We also found that Si, Mn, Ni, and Cu, which existed in the molten aluminum during hot dip aluminizing, started to oxidize.

When we increased the temperature to 1000°C, the HDA carbon steel specimens were mainly oxidized, as shown in Figure 69. In the upper part of the oxidized layer, Al could still be detected by the EDS, even though it was dispersed. In the lower part of Figure 70(H), we observed that the oxidized layer was about to split, where continuous cavities developed at the interface with the substrate. Moreover, iron oxide was detected on the boundary layer of the grains of the substrate below the interface.

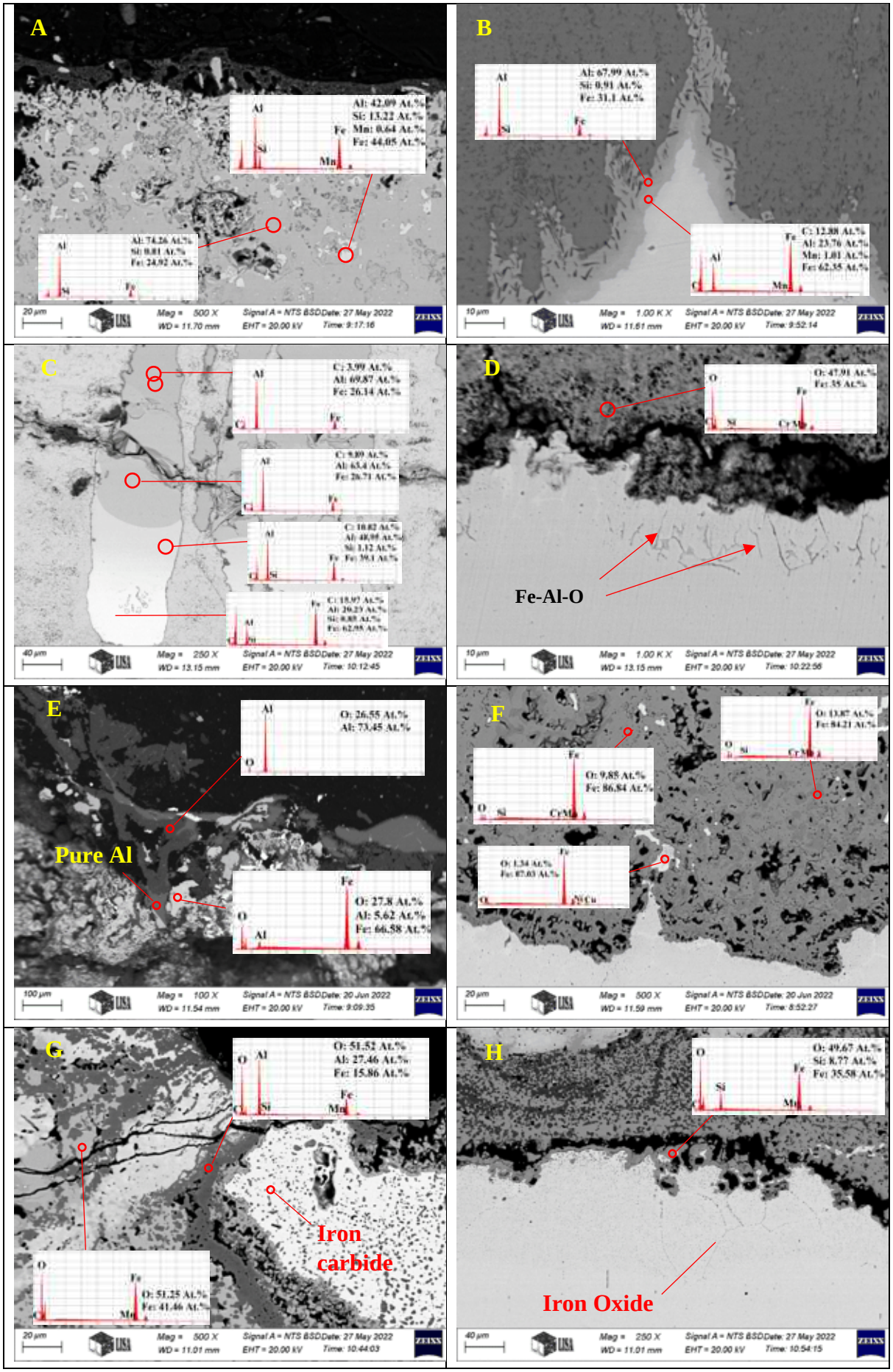
A
B
C
D
Fe-Al-O
E
Pure Al
F
G
Iron carbide
H
Iron Oxide

Figure 70. Represent the identified area in figure (76) for a period of 72 h and the four temperatuers combined with EDS spot analysis.

The study aimed to investigate the oxidation resistance of HDA carbon steel C45 at different temperatures, specifically 700, 800, 900, and 1000 °C, for three periods of 8, 24, and 72 hours each. The results of the weight change measurement showed a steady-state condition of the HDA samples exposed to hot air at 700 °C for 24 to 72 hours, as indicated by Figure 59. The cross-sectional view of this part in Figures 65, 66(A), 66(B), 67, 68(A), 68(B), 69, 70(A), and 70(B) showed no or slight degradation at 700 °C, probably proper operating temperature for a HDA carbon steel C45 is 700 °C or lower operating temperatures, which do not affect the base metal substrate. The dominant phase $FeAl_2$ at the top layer was detected for samples held at 700 and 800 °C for all durations, while it was also found in a portion or separate islands with the sample held at 900 °C. The one-to-one mole ratio of Fe-Al possibly represents the FeAl phase found at the interface with the substrate, especially at 700 °C. Cracks and pores increased with temperature and exposure time, possibly due to differences in thermal expansion [129] or vacancy diffusion, and the interaction of carbon content with oxygen gain. Spall off the scale was also detected. The depletion of aluminum was observed in stages with increasing temperatures, with the amount of Al decreasing to 20 At.% and less than this in harmony with raising the oxygen content. After reducing the Al content to less than 10 At.%, the aluminum alloying element was used for hot dip aluminizing. The compositions of the carbon steel C45 substrate are more susceptible to oxidation, such as Si and Mn.

CHAPTER 5: Thesis points

Structure characteristics during hot dip aluminizing and the impact of the interlayer on the intermetallic layer development

Claim 1. The role of carbon content of the substrate steel C45 in the coating layers evolution during hot dip aluminizing with commercially pure aluminium.

During the hot-dip aluminizing (HDA) process run at 700 °C and for 2.5 min dipping time, the iron (Fe) atoms of the solid substrate steel C45 normally tend to diffuse out into the molten aluminum bath and/or produce new solid Fe-Al intermetallics at the solid/liquid interface. This, in turn, should create more vacant places in the steel lattice structure, enhancing the diffusion of some carbon atoms towards the intermetallics and topcoat aluminum layer. Consequently, the structure of the detected EBSD spot (shown in Figures I and II) is similar to that of the perovskite structure of the so-called κ-carbide phase (Fe_3AlC) identified within the intermetallic layer. Whereas the other EBSD spot (shown below on the right) showed a face-centered cubic structure of phase AlC in the topcoat layer. GDOES analysis also confirmed the above findings.

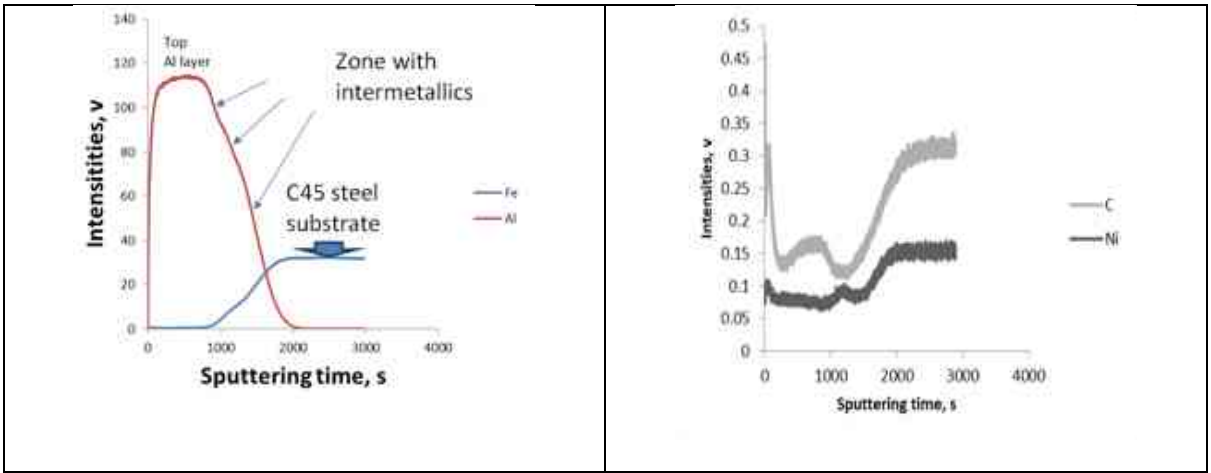

Figure I. GD-OES profiles for Fe and Al, together with the two minor elements C and Ni vs. the argon ion sputtering time, while forming a crater inwards the sample.

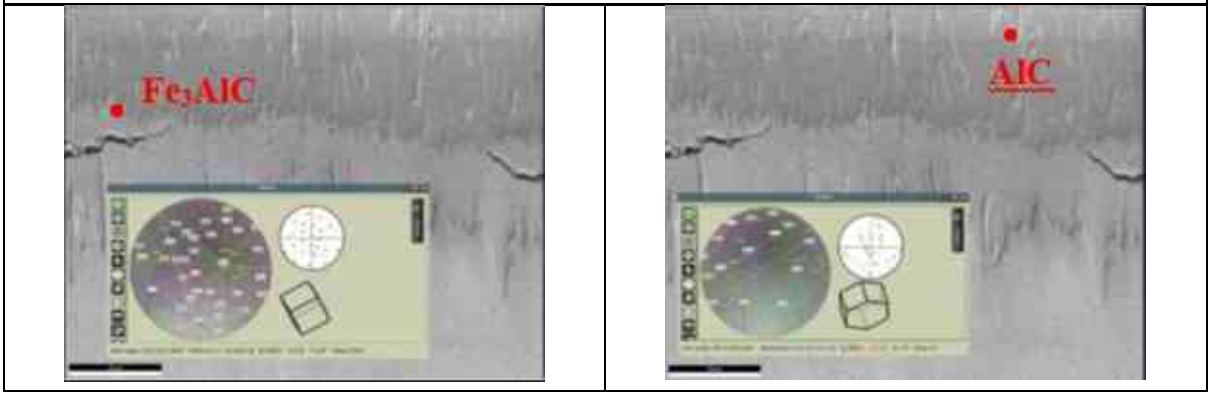

Figure II. The EBSD spot analysis was examined to specify the type of formed phase during HDA.

Claim 2(a)(b). Growth kinetics of Fe_2Al_5 layer due to the copper interlayer before hot dip aluminizing with commercially pure aluminum.

Claim 2(a) Based on my experimental results, I can state that the growth kinetics of η-Fe_2Al_5 follow parabolic growth kinetic with a growth rate equal to 6.46×10^{-13} $m^2.s^{-1}$. The growth rate of η-Fe_2Al_5 has diminished sharply due to using copper as an interlayer before hot dip aluminizing the steel C45 specimens compared with the results of other aluminizing techniques used, such as precoating with other elements or alloying the molten bath (as detailed in Tables I and II).

Claim 2(b) For a short period of immersion of 45 s dipping time, the intermetallic layer thickness amounted to approximately 11 μm, with the η-Fe_2Al_5 layer approximately 4 μm thick and the θ-Fe_4Al_{13} layer approximately 7 μm.

Table I. The intermetallic layer formation characteristics developed on pure and carbon steel substrate during HDA using aluminium alloy as a liquid bath.

Intermetallic Phase type	Bath compositions	Substrate material	Observation based on the structure appearance of the sample's cross-section, including the determined constant growth rate (k)	Dipping time	Aluminizing temperature, ºC	Thickness, µm	Ref.
Fe_3Al, Fe_2Al_5 With 6% Si	Al – 1.8 % Si Al – 6 % Si		The interface exhibits a uniform thickness at 1.8% Si content, while with 6% Si, very smooth and planar could be seen at the interface.	2 and 10 min. The structure of both Si-content in liquid baths does not affect by dipping time.	-	~ 20 with 1.8% Si Around 1-2 with 6% Si	[130]
Al-Cu-Fe, Al-Cu	Al – 11 wt.% Cu	AISI 1040	The IM structure displays smooth and even growth for shorter dipping time, while increasing dipping time, uneven growth and a finger-like structure could be seen. The thickness of IM was reduced by up to 75 %.	2-10 min.	700	~ 40 for 2 min. and ~ 50 for 10 min.	[131]
Fe_3Al, Fe_2Al_5, Al_7Fe_2Si, Al_2FeSi, Al_3FeSi_2	Al – 6.9 Si – 1.4 Mg	Interstitial free steel	The IM structure exhibits even, smooth and thin growth, the thickness increased with increasing dipping time.	0.5, 1, 3, and 6 min.	700	~ 25 for 0.5 min., and over 50 for 6 min.	[132]
Fe-Al, Fe-Al-Si	Al – 10 Si	AISI 1005	A continuous, even, and a thin layer of IM formed at the interface.	180 sec.	700	3	[133]
Fe_4Al_{13}, Fe_2Al_5 At 05 Si up to 4% Si from 4% Si $Al_2Fe_3Si_3$ at 6% Si Al_8Fe_2Si at 10% Si, only Fe_2Al_5 and Al_8Fe_2Si exist.	Al – 1, 2, 4, 6, and 10 Wt.% Si	High-purity iron sheet 99.99 Wt.% Fe	The IM layer at 0% Si displays a finger-like structure that starts to transform with the increasing Si content and becomes flattened at 10% Si.	15, 30, 45, 60, 90, 120, 300, 600, 900, 1800 sec.	700	The IM layer thickness at 0% Si equals 66 and becomes around 5 at 10% Si content.	[134]
With 7% Si; Fe_2Al_7Si, Fe_2Al_5, $Fe_3(Al,Si)_5$, $FeAl_3$ Same with 12% Si, with 3% Mn	Al – 7 Si Al – 12 Si Al – 3 Mn	SAE 1013	The IM layer structure with 7% Si shows a thinner layer in thickness, smooth still the rough (finger-like) structure could be seen but lesser compared to pure aluminium bath and increase slightly with increasing dipping time. In contrast, the bath containing 12% Si had a smoother and	5-900 s	750	13 ± 3 for 7% Si 11 ± 5 for 12% Si. The measurement starts from the initial	[135]

Fe_2Al_5 and $FeAl_3$ and dispersed Mn within the topcoat layer.			flat IM layer growth compared to the previous. The bath, which contains 3% Mn, doesn't show any effect on the structure or the thickness of the intermetallic layer, however, it increases the brittleness of the IM layer, and more cracks could be seen within the IM layer.			time of dipping till 900 s.	
Fe_2Al_5 and $FeAl_3$ with the presence of Si	Al – 8.2 Mg – 4.8 Si	Pure iron	The IM layer exhibit smooth, continuous, thin, and even growth at a certain dipping time and starts to increase slightly.	2 – 1800 s	750		[136]
Fe_2Al_5, $FeAl_3$	Al – 5 Wt.% Cr	Cold-rolled low-carbon steel, 0.036 Wt.%	The structure of IM displayed the same morphology as reported with pure aluminium; it concluded that the chromium has no effect on the intermetallic but improves the scratch hardness due to the presence of Al7Cr dispersed in the top coat layer.	Ranging from 10 to 1800 s.	700	-	[137]
Mainly Fe_2Al_5, and $FeAl_3$ with the presence of a Fe-Al-Si ternary alloy system.	Al – 6.9Si – 1.4Mg	Interstitial-free steel (IF steel)	The IM thickness exhibit smooth, uniform growth and a flat increase in thickness with increasing dipping time.	0.5, 1, 3, and 6 min.	800	Average thickness 4 for 0.5 min. 5 for 1 min. 8 for 3 min. 10 for 6 min.	[138]
-	Al – 1 at.% Si Al – 2 at.% Si Al – 3 at.% Si Al–0.5 at.% Mg Al–1 at.% Mg Al–2 at.% Mg Al–3 at.% Mg	Medium carbon steel 0.44 wt.% C	The IM layer displays uniform growth and is less rough toward the substrate by the addition of Si compared with pure Al bath, and it is increased in thickness with the increasing immersion time. The addition of Mg will return the irregular shape of the IM layer but with less degree compared to pure Al bath. According to the activation energy of 1 at.% Si-Al and 1 at.% Mg-Al, the growth rate is lower compared to pure Al bath.	1, 3, 5, 10, 15, and 20 min.	800	At 1 min. dipping time 3 at.% Si ~ 25 3 at.% Mg ~ 225	[139]

Table II. The intermetallic layer formation characteristics developed on carbon steel substrate during HDA using the precoat method before aluminizing.

Intermetallic Phase type	Bath compositions	Precoat material/ Coating	Substrate material	Observation based on the structure appearance of the sample's cross-	Dipping time	Aluminizing temperature, °C	Thickness, µm	Ref.

		method/Heat treatment		section, including the determined constant growth rate (k)				
$NiAl_3$ with 5 s, Ni_2Al_3, $NiAl_3$, $(Fe,Ni)_2Al_9$ with 60 s, Fe_2Al_5, $FeAl_3$ with 120 s.	Pure aluminium	Nickel/ Electroplating/ without heat treatment	AISI 1005	The IM structure shows even growth for 5 and 30 s dipped time; after longer dipping, i.e., 60 s, the uneven growth starts to appear and clearly could be seen with 120 s dipped time combined with rough growth as a finger-like structure. Growth rate of Fe_2Al_5 layer with n=0.5 was about 6.51×10^{-12} ($m^2.s^{-1}$)	5-720 s	670	The total IM layer was about 30 with 120 s dipped time.	[140]
Fe_2Al_5, $FeAl_3$	AA 6061	Tin powder + flux (24 g $ZnCl_2$, 6 g NaCl, 3 g NH_4Cl, 1 mL HCl and 1 mL H_2O)/ powder dispersed in flux mixture/ hot treated on a hot plate for 2.5 min. at 350 ºC.	Low-carbon steel, 0.14 Wt.% C.	The IM layer showed even, thin and uniform growth at low dipping time, which increased with increasing time.	0.5, 1, 2.5, and 3.5 min.	750	~ 25 for 0.5 min., and ~ 28 for 2.5 min.	[141]
Fe_2Al_5, $FeAl_3$	Pure aluminium purity 99.7%	Aluminium/ magnetron sputtering/ heat treatment was conducted after deposition for 30 min. at 600 ºC in an Ar atmosphere.	Q235	The IM structure exhibits a comb-tooth on the substrate side of the interface, and the neighbouring tooth of the comb-tooth structure was sparsely arranged. The distance between the teeth peak and valley was relatively large.	20 s	720	The average thickness of IM is 9-21, with the mean equal to 15.63 and 3.50 SD.	[142]
Fe_2Al_5, Fe_4Al_{13}	Commercially pure aluminum 98 %	Copper electroplated	Carbon steel C45	The IM structure exhibits slightly even and regular growth for 45 s dipping time at the interface with the substrate carbon steel C45 then irregular growth with the appearance of a finger-like structure start to grow with increasing dipping time. Growth rate of Fe_2Al_5 layer with n=0.58	45, 85, 150, and 300 s.	700 ± 10 ºC	After dipping for 45 s, the IM was about 11µm, the	Present study

				was about 0.646 $m\mu^2 . s^{-1}$ or (6.46×10^{-13} $m^2 . s^{-1}$)			Fe_2Al_5 was about 4µm.	

Claim 3. Having compared the difference in grain size between Fe_2Al_5 and Fe_4Al_{13} phases both for the case of traditional hot dip aluminizing and aluminizing having a copper precoat interlayer.

The average size of about 1.8 µm was achieved for both types of grains at 2.5 min dipping time and a constant aluminizing temperature of 700 °C during the traditional HDA process.

I establish that applying a copper interlayer, which can also form some solid Al-Cu compounds, could hinder the rapid diffusion of both Fe and Al during the first tens of seconds of the dipping process. Hence, it will mitigate the preferential growth in the c-direction of the phase Fe_2Al_5, which will result in getting finer grain than in the case of the traditional HDA process.

Table III. The difference in grain size of the two main intermetallic phases was obtained with traditional hot dip aluminizing using commercially pure aluminum, and the other obtained after using a precoat layer of copper before hot dip aluminizing.

	Traditional hot dip aluminizing		Using the copper precoat before hot dip aluminizing	
	Fe_2Al_5	Fe_4Al_{13}	Fe_2Al_5	Fe_4Al_{13}
Average grain size	1.8 µm	0.4 µm	1.74 µm	0.75 µm
Std.	1.8	0.075	0.45	0.2

Claim 4. By depositing a thin layer of copper using PVD and applying solder paste-type flux before aluminizing, the wettability of carbon steel C45 can be improved.

Based on experimental observation using PVD and applying paste-type solder flux on the carbon steel C45 before dipping, I can establish that the proper modification of the wettability of carbon steel C45 with our solution (as shown in Table IV) makes it possible to achieve remarkable improvement in the evolution of the aluminized surface layer.

Table IV. A collection of photos documenting the use of various techniques to enhance wettability.

Bare ground and polished carbon steel C45 sample	The aluminized sample was obtained with a salt mixture of KCl, NaCl, and CaF_2 as a flux poured on top of the molten aluminium.	The thickness of carbon steel C45 with thin copper deposited on it via PVD was about one micron.	The aluminized carbon steel C45 was obtained after using the thin copper layer with the addition of a salt mixture of KCl, NaCl, and CaF_2 as a flux poured on top of the molten aluminium.

Corrosion resistance of HDA carbon steel C45 in environment with molten salt

Claim 5. The carbon content in the substrate carbon steel C45 and their contribution to the degradation process.

During the high-temperature investigation, I can establish that exposure to molten salt of NaCl and Na_2SO_4 can cause carbon content to accumulate at the interdiffusion layers (emergent layer). It forms a spotty flake-like feature (Figure IV) with different kinds of carbides of the Fe-Al-C system.

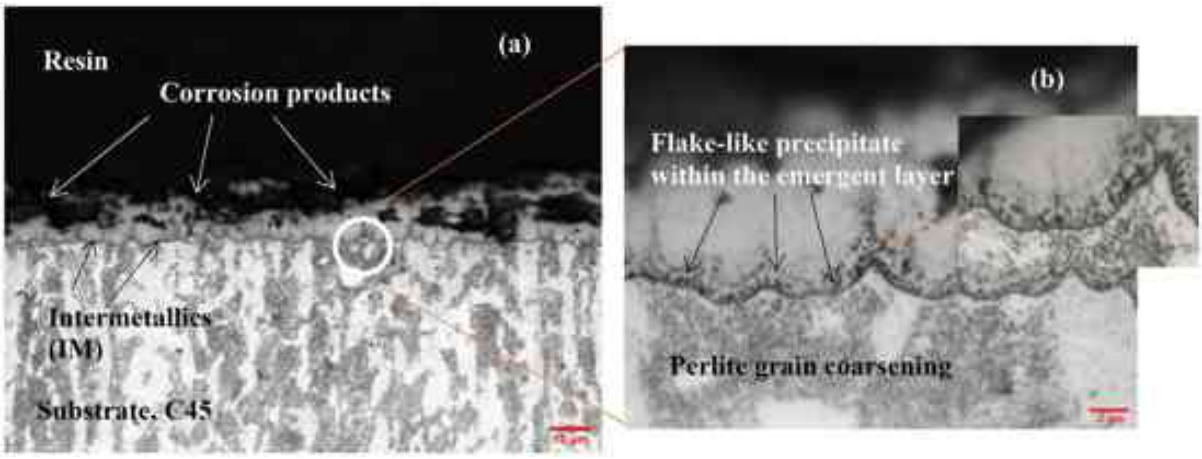

Figure IV. Optical microscope image of HDA half immersed at 700 °C in molten salt with exposure time equal to 24 h; (a) cross-sectional view of the HDA after exposure, (b) the marked portion enlarged to highlight the precipitate of flake-like structure within the emergent layer and the pearlite grain growth/coarsening.

Claim 6. The role of chlorine in the degradation of HDA carbon steel C45 at 700 °C during exposure to molten salt mixture of NaCl and Na_2SO_4 is significant.

Through extensive thermodynamic research, coupled with metallographic analysis, I have discovered the crucial role that chlorine plays in the degradation process by means of cyclic oxychlorination. This finding highlights the importance of understanding and controlling the effects of chlorine in order to improve the durability and performance of such hot dip aluminized (HDA) products.

The oxidation resistance of HDA carbon steel C45 at high temperatures

Claim 7. Suitable temperature for operating HDA carbon steel C45 in hot air environment.

To ensure optimal performance of HDA carbon steel C45 in hot air environment, it has been determined that the hot dip aluminized steel is better operated at a temperature of 700 °C or lower. By doing so, the risk of oxidation and deterioration of the steel substrate is significantly reduced, as demonstrated in Figure V.

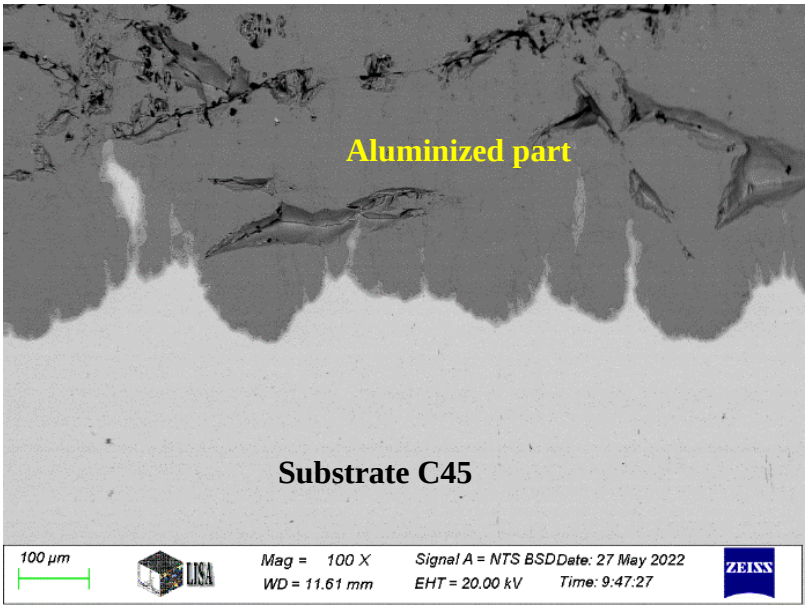

Figure V. The cross-section of HDA carbon steel C45 was held for 72 h at a temperature of 700 °C.

Acknowledgment

I want to give a big shout-out to my supervisor, Prof. Dr. Tamás I Török, for his exceptional guidance, unwavering support, and invaluable feedback. This work would not have been possible without his assistance, advice, and encouragement. Moreover, I want to express my deepest appreciation to my family, particularly my dear parents, especially my mom ❤️, for their unwavering commitment, support, and encouragement throughout this journey. I would like to express my utmost appreciation to my esteemed reviewers and committee, particularly Dr. Zsolt Veres, for thoroughly reviewing my report each semester with great diligence and providing detailed feedback. I extend my sincere gratitude to Mr. Tibor Ferenczi, Mr. Árpád Kovács, Mrs. Anikó Márkus, Mr. Gábor Lassú and Dr. Kulcsár Tibor for their invaluable assistance in the laboratory preparation, material procurement, sample preparation, and conducting laboratory tests including SEM and GD-OES. Their contributions and support were instrumental in the success of my dissertation.

I would like to express my gratitude to Mrs. Ágnes Solczi, Mrs. Zsarnainé Gáthi Gabriella, Mrs. Gabriella Balázsdi-Szabó, and Mrs. Éva Stumpf from the Administration staff. They have been so operative and helpful. Their assistance has been critical in ensuring the smooth running of my Ph.D. program, and I am incredibly thankful for their hard work and dedication.

I also wish to thank the Institute of Chemical Metallurgy and Foundry Engineering, and Institute of Physical Metallurgy, Metal Forming, Nanotechnology Faculty of Materials and Chemical Engineering, University of Miskolc, and the Antal Kerpely Doctoral School of Materials Science & Technology (Faculty of Materials Science & Engineering) at the University of Miskolc.

Thanks to the Stipendium Hungaricum Program and the Kurdistan Region Government/Ministry of Higher Education and Scientific Affairs, I was able to study at the University of Miskolc. Finally, I was lucky to meet such talented scientists.

Lastly, I want to express my gratitude to everyone who contributed to this work, even if they were not mentioned here.

List of Publications and Conferences

Publications:

1. Hawkar J. Muhammed, Márton Benke, Dániel Koncz-Horváth, Zsolt Sályi, Tamás I. Török. Characterization of Hot-Dip Aluminized C45 Carbon Steel before and after Cyclic Heating in Air, *Surface Engineering and Applied Electrochemistry*. **57**, 431–438 (2021). https://doi.org/10.3103/S1068375521040116
2. Hawkar J. Muhammed, Márton Benke, Dániel Koncz-Horváth, Zsolt Sályi, Tamás I. Török, Texture Analysis and Corrosion Testing of Aluminized Carbon Steel C45, *Materials Science and Engineering*, Volume 45, No. 1 (2020), pp. 136–142.DOI: 10.32974.mse.2020.013
3. Hawkar J. Muhammed, Dániel Koncz-Horváth, Gábor Lassú, István Balázs Illés & Tamás I. Török, Characterization Of Fe–Al Intermetallic Phases Formed During Hot-Dip Al Coating on Carbon Steel C45, *MRS Communications* 12, pages 68–73 (2022), https://doi.org/10.1557/s43579-021-00142-9.
4. Hawkar J. Muhammed, Dániel Koncz-Horváth, István Balázs Illés & Tamás I. Török, Surface Protective Layers of Iron Aluminides Developed on Medium Carbon Steel by the Hot-Dip Aluminizing (HDA) Process, *Multidiszciplináris tudományok*, 11. kötet. (2021) 5 sz. pp.68-77, https://doi.org/10.35925/j.multi.2021.5.7.
5. Hawkar J. Muhammed, Dániel Koncz-Horváth & Tamás I. Török, Corrosion Behavior of HDA (Hot-Dip Aluminized) Carbon Steel C45 Half Immersed in Molten Salts (NaCl, Na_2SO_4) Isothermally at 973 K, *Journal of Adhesion Science and Technology*, 13 Dec 2022, https://doi.org/10.1080/01694243.2022.2159305

Conferences:

1. Aluminizing (HDA) Process, MultiScience - XXXIV. microCAD International Multidisciplinary Scientific Conference, Miskolc, Hungary, Sep. 2021 https://multiscience.uni-miskolc.hu/session-programs.
2. Hawkar J. Muhammed, Dániel Koncz-Horváth, Tamás I. Török, Corrosion behavior of HDA (hot-dip aluminized) carbon steel C45 half immersed in molten salts (NaCl, Na_2SO_4) isothermally at 700 °C, International conference oral presentation, not in Hungarian, Istanbul, Turkey, 25-26 May 2022, https://caspconferences.com/docs/CaspProgram.pdf.
3. Oral presentation: Coatings of Turbine Engine Components A review of slurry aluminizing, Ph.D. Forum/ Faculty of Material Science and Technology/ University of Miskolc/ Miskolc/ Hungary, 21.11.2019.

References

[1] P. R. Roberge, *Handbook of corrosion engineering*, Third. New York: McGraw-Hill, 2019.

[2] *Uhlig's Corrosion Handbook*. 2011. doi: 10.1002/9780470872864.

[3] M. G. Fontana, *Corrosion engineering*. New York: McGraw-Hill, 1987.

[4] N. Birks, G. H. Meier, and F. S. Pettit, *Introduction to the high temperature oxidation of metals, Second edition*, vol. 9780521480420. 2006. doi: 10.1017/CBO9781139163903.

[5] R. A. Rapp, "High Temperature Oxidation of Metals Forming Cation-Diffusing Scales," *Metallurgical transactions. A, Physical metallurgy and materials science*, vol. 15 A, no. 5, 1984, doi: 10.1007/BF02644552.

[6] C. J. Wang and J. Y. Pan, "Corrosion of carbon steel with NaCl coating in an atmosphere produced by burning emulsified diesel oil," *Mater Chem Phys*, vol. 82, no. 3, 2003, doi: 10.1016/j.matchemphys.2003.08.017.

[7] M. Badaruddin, A. Y. E. Risano, H. Wardono, and D. Asmi, "Hot-corrosion of AISI 1020 steel in a molten NaCl/Na_2SO_4 eutectic at 700°C," in *AIP Conference Proceedings*, 2017. doi: 10.1063/1.4968319.

[8] H. Gerengi, N. Sen, I. Uygur, and E. Kaya, "Corrosion behavior of dual phase 600 and 800 steels in 3.5 wt.% NaCl environment," *J Adhes Sci Technol*, vol. 34, no. 8, 2020, doi: 10.1080/01694243.2019.1688925.

[9] D. Pradhan, M. Manna, and M. Dutta, "Al-Mg-Mn alloy coating on steel with superior corrosion behavior," *Surf Coat Technol*, vol. 258, 2014, doi: 10.1016/j.surfcoat.2014.08.061.

[10] D. Lee and X. Xiao, "Corrosion of Fe-17%Cr Steels in (Na_2SO_4+NaCl) Salts at 800 and 900 °C," *Korean Journal of Surface Engineering*, vol. 51, no. 4, 2018.

[11] C. Ciszak, I. Popa, J. M. Brossard, D. Monceau, and S. Chevalier, "NaCl induced corrosion of Ti-6Al-4V alloy at high temperature," *Corros Sci*, vol. 110, 2016, doi: 10.1016/j.corsci.2016.04.016.

[12] M. Nimmervoll, A. Schmid, G. Mori, S. Hönig, and R. Haubner, "Surface sulphide formation on high-temperature corrosion resistant alloys in a H_2S-HCl-CO_2 mixed atmosphere," *Corros Sci*, vol. 181, 2021, doi: 10.1016/j.corsci.2021.109241.

[13] Y. F. Yan *et al.*, "Hot corrosion behaviour and its mechanism of a new alumina-forming austenitic stainless steel in molten sodium sulphate," *Corros Sci*, vol. 77, 2013, doi: 10.1016/j.corsci.2013.08.003.

[14] S. Zhang *et al.*, "Chloride- and sulphate-induced hot corrosion mechanism of super austenitic stainless steel S31254 under dry gas environment," *Corros Sci*, vol. 163, 2020, doi: 10.1016/j.corsci.2019.108295.

[15] A. C. S. Sabioni, A.-M. Huntz, E. C. da Luz, M. Mantel, and C. Haut, "Comparative study of high temperature oxidation behaviour in AISI 304 and AISI 439 stainless steels," *Materials Research*, vol. 6, no. 2, 2003, doi: 10.1590/s1516-14392003000200012.

[16] M. Badaruddin, C. J. Wang, Y. Saputra, and A. K. Rivai, “High Temperature Corrosion of Aluminized AISI 4130 Steel with the Different Composition of NaCl/Na_2SO_4 Deposits,” *Makara Journal of Technology*, vol. 19, no. 2, 2015, doi: 10.7454/mst.v19i2.3033.

[17] C.-C. Tsaur, “High temperature oxidation and NaCl-induced accelerated corrosion of hot-dip aluminized 9Cr-1Mo and 310 stainless steel,” Doctoral dissertation, Texas A&M University, 2004. Accessed: Nov. 24, 2022. [Online]. Available: https://hdl.handle.net/1969.1/1375

[18] M. Badaruddin, C. J. Wang, H. Wardono, Tarkono, and D. Asmi, “High-temperature oxidation behavior of aluminized AISI 4130 steel,” in *AIP Conference Proceedings 1711*, 2016, p. 040002. doi: 10.1063/1.4941624.

[19] J. Fite, S. Eswarappa Prameela, J. A. Slotwinski, and T. P. Weihs, “Evolution of the microstructure and mechanical properties of additively manufactured AlSi10Mg during room temperature holds and low temperature aging,” *Addit Manuf*, vol. 36, p. 101429, Dec. 2020, doi: 10.1016/j.addma.2020.101429.

[20] B. Parveez, M. I. Kittur, I. A. Badruddin, S. Kamangar, M. Hussien, and M. A. Umarfarooq, “Scientific Advancements in Composite Materials for Aircraft Applications: A Review,” *Polymers (Basel)*, vol. 14, no. 22, p. 5007, Nov. 2022, doi: 10.3390/polym14225007.

[21] S. Akhtar, M. Saad, M. R. Misbah, and M. C. Sati, “Recent Advancements in Powder Metallurgy: A Review,” *Mater Today Proc*, vol. 5, no. 9, pp. 18649–18655, 2018, doi: 10.1016/j.matpr.2018.06.210.

[22] P. Descamps, J. Tirlocq, and F. Cambier, “Ceramic Matrix Composites: Properties and Applications,” in *3rd European Symposium on Engineering Ceramics*, Dordrecht: Springer Netherlands, 1991, pp. 109–125. doi: 10.1007/978-94-011-7990-4_9.

[23] R. Aslam, M. Mobin, S. Zehra, and J. Aslam, “A comprehensive review of corrosion inhibitors employed to mitigate stainless steel corrosion in different environments,” *J Mol Liq*, vol. 364, p. 119992, Oct. 2022, doi: 10.1016/j.molliq.2022.119992.

[24] L. Antoni, “Materials for Solid Oxide Fuel Cells: the Challenge of their Stability,” *Materials Science Forum*, vol. 461–464, pp. 1073–1090, Aug. 2004, doi: 10.4028/www.scientific.net/MSF.461-464.1073.

[25] H. Bhadeshia and R. Honeycombe, “Stainless Steel,” in *Steels: Microstructure and Properties*, Elsevier, 2017, pp. 343–376. doi: 10.1016/B978-0-08-100270-4.00012-3.

[26] Y. Y. Liu *et al.*, “Effect of Al content on high temperature oxidation resistance of AlxCoCrCuFeNi high entropy alloys (x=0, 0.5, 1, 1.5, 2),” *Vacuum*, vol. 169, p. 108837, Nov. 2019, doi: 10.1016/j.vacuum.2019.108837.

[27] R. P. Oleksak, C. S. Carney, G. R. Holcomb, and Ö. N. Doğan, “Structural Evolution of a Ni Alloy Surface During High-Temperature Oxidation,” *Oxidation of Metals*, vol. 90, no. 1–2, pp. 27–42, Aug. 2018, doi: 10.1007/s11085-017-9821-6.

[28] Y. Zhang *et al.*, “Microstructures and properties of high-entropy alloys,” *Prog Mater Sci*, vol. 61, pp. 1–93, Apr. 2014, doi: 10.1016/j.pmatsci.2013.10.001.

[29] Y. F. Ye, Q. Wang, J. Lu, C. T. Liu, and Y. Yang, “High-entropy alloy: challenges and prospects,” *Materials Today*, vol. 19, no. 6, pp. 349–362, Jul. 2016, doi: 10.1016/j.mattod.2015.11.026.

[30] B. Cantor, I. T. H. Chang, P. Knight, and A. J. B. Vincent, “Microstructural development in equiatomic multicomponent alloys,” *Materials Science and Engineering: A*, vol. 375–377, pp. 213–218, Jul. 2004, doi: 10.1016/j.msea.2003.10.257.

[31] D. K. Mukhopadhyay, F. H. Froes, and D. S. Gelles, “Development of oxide dispersion strengthened ferritic steels for fusion,” *Journal of Nuclear Materials*, vol. 258–263, pp. 1209–1215, Oct. 1998, doi: 10.1016/S0022-3115(98)00188-3.

[32] I. López-Ferreño, J. F. Gómez-Cortés, T. Breczewski, I. Ruiz-Larrea, M. L. Nó, and J. M. San Juan, “High-temperature shape memory alloys based on the Cu-Al-Ni system: design and thermomechanical characterization,” *Journal of Materials Research and Technology*, vol. 9, no. 5, pp. 9972–9984, Sep. 2020, doi: 10.1016/j.jmrt.2020.07.002.

[33] F. Zhang *et al.*, “Self-healing mechanisms in smart protective coatings: A review,” *Corros Sci*, vol. 144, pp. 74–88, Nov. 2018, doi: 10.1016/j.corsci.2018.08.005.

[34] H. M. H. Farh, M. E. A. Ben Seghier, and T. Zayed, “A comprehensive review of corrosion protection and control techniques for metallic pipelines,” *Eng Fail Anal*, vol. 143, p. 106885, Jan. 2023, doi: 10.1016/j.engfailanal.2022.106885.

[35] L. T. Nhiem, D. T. Y. Oanh, and N. H. Hieu, “Nanocoating toward anti-corrosion: A review,” *Vietnam Journal of Chemistry*, vol. 61, no. 3. John Wiley and Sons Inc, pp. 284–293, Jun. 01, 2023. doi: 10.1002/vjch.202300025.

[36] H. Zhou, H. Niu, H. Wang, and T. Lin, “Self-Healing Superwetting Surfaces, Their Fabrications, and Properties,” *Chem Rev*, vol. 123, no. 2, pp. 663–700, Jan. 2023, doi: 10.1021/acs.chemrev.2c00486.

[37] M. Shourgeshty, M. Aliofkhazraei, and M. M. Alipour, “Introduction to High-Temperature Coatings,” in *High Temperature Corrosion*, InTech, 2016. doi: 10.5772/64282.

[38] H. Xu, H. Guo, and S. Gong, “Thermal barrier coatings,” in *Developments in High Temperature Corrosion and Protection of Materials*, Elsevier, 2008, pp. 476–491. doi: 10.1533/9781845694258.2.476.

[39] N. P. Padture, M. Gell, and E. H. Jordan, “Thermal Barrier Coatings for Gas-Turbine Engine Applications,” *Science (1979)*, vol. 296, no. 5566, pp. 280–284, Apr. 2002, doi: 10.1126/science.1068609.

[40] G. Barroso, Q. Li, R. K. Bordia, and G. Motz, “Polymeric and ceramic silicon-based coatings – a review,” *J Mater Chem A Mater*, vol. 7, no. 5, pp. 1936–1963, 2019, doi: 10.1039/C8TA09054H.

[41] J. D. Torrey and R. K. Bordia, “Phase and microstructural evolution in polymer-derived composite systems and coatings,” *J Mater Res*, vol. 22, no. 7, pp. 1959–1966, Jul. 2007, doi: 10.1557/jmr.2007.0246.

[42] R. S. Dutta, S. Bhandari, Y. Chakravarthy, B. Vishwanadh, K. Singh, and G. K. Dey, “Development Of Aluminide Coatings On Ni-Cr-Fe Based Superalloy 690 Substrates For High Temperature Applications Using Atmospheric Plasma Spraying Technique,” *Mater Today Proc*, vol. 3, no. 9, pp. 3018–3024, 2016, doi: 10.1016/j.matpr.2016.09.016.

[43] J. Boyner, *Workshop Practice Series- Electroplating. 11*. Hertfordshire: Trans-Atlantic Publications, 1986.

[44] W. Giurlani *et al.*, “Electroplating for Decorative Applications: Recent Trends in Research and Development,” *Coatings*, vol. 8, no. 8, p. 260, Jul. 2018, doi: 10.3390/coatings8080260.

[45] “Electroplating,” https://en.wikipedia.org/wiki/Electroplating#/media/File:Copper_electroplating_principle_(multilingual).svg.

[46] P. ’Møller and L. P. ’Nielsen, *Advanced Surface Technology*, vol. 01. Washington, DC: National Association for Surface Finishing , 2013.

[47] C. M. ’ ’Cotell, J. A. ’ ’Sprague, F. A. ’ ’Smidt, and Asm International Staff, *ASM Handbook Volume 5: Surface Engineering*. Ohio: ASM International, 1994.

[48] “physical vapor depositon,” https://www.arceo-eng.com/assets/083977b6-c2c8-44be-a580-870d943181ad/physical-vapor-depositon-2019.pdf.

[49] B. ’Rannou, “Slurry coatings from aluminum microparticles on Ni-based super alloys for high temperature oxidation protection,” Université de La Rochelle, 2012.

[50] “Polyvinyl alcohol,” https://en.wikipedia.org/wiki/Polyvinyl_alcohol.

[51] “Particoat,” http://www.particoat.eu/.

[52] B. Grégoire, G. Bonnet, and F. Pedraza, “Development of a new slurry coating design for the surface protection of gas turbine components,” *Surf Coat Technol*, vol. 374, pp. 521–530, Sep. 2019, doi: 10.1016/j.surfcoat.2019.06.020.

[53] J. Lu *et al.*, “Preparation and characterization of slurry aluminide coating on Super304H boiler tube in combination with heat-treatment process,” *Surf Coat Technol*, vol. 370, pp. 97–105, Jul. 2019, doi: 10.1016/j.surfcoat.2019.04.061.

[54] M. D. Nguyen *et al.*, “Slurry spray coating of carbon steel for use in oxidizing and humid environments,” *Ceram Int*, vol. 44, no. 7, pp. 8306–8313, May 2018, doi: 10.1016/j.ceramint.2018.02.017.

[55] J. T. Bauer, X. Montero, M. Schütze, and M. C. Galetz, “Innovative slurry coating concepts for aluminizing of an austenitic steel in chlorine and sulfur containing atmosphere,” *Surf Coat Technol*, vol. 285, pp. 179–186, Jan. 2016, doi: 10.1016/j.surfcoat.2015.10.074.

[56] B. Bouchaud, B. Rannou, and F. Pedraza, “Slurry aluminizing mechanisms of Ni-based superalloys incorporating an electrosynthesized ceria diffusion barrier,” *Mater Chem Phys*, vol. 143, no. 1, pp. 416–424, Dec. 2013, doi: 10.1016/j.matchemphys.2013.09.022.

[57] A. J. Rasmussen, A. Agüero, M. Gutierrez, and M. José Landeira Østergård, “Microstructures of thin and thick slurry aluminide coatings on Inconel 690,” *Surf Coat Technol*, vol. 202, no. 8, pp. 1479–1485, Jan. 2008, doi: 10.1016/j.surfcoat.2007.06.056.

[58] X. Montero, I. Demler, V. Kuznetsov, and M. C. Galetz, “Factors governing slurry aluminization of steels,” *Surf Coat Technol*, vol. 309, pp. 179–186, Jan. 2017, doi: 10.1016/j.surfcoat.2016.11.067.

[59] P. Maaß and P. Peißker, Eds., *Handbook of Hot-Dip Galvanization*. Wiley, 2011. doi: 10.1002/9783527636884.

[60] “Hot dip galvanized ,” https://www.dak.hu/en/termekek/tuzihorganyzas/the-technology-behind-hot-dip-galvanizing.

[61] “Hot dip galvanized process,” https://galvanizeit.org/hot-dip-galvanizing/hdg-process.

[62] “Hot dip galvanized ,” https://www.hitoeng.com/hot-dip-galvanizing-line-for-galvanized-coils.html.

[63] “Galvanized sheet,” https://pshop7.pw/ProductDetail.aspx?iid=666223733&pr=68.88.

[64] Z. ’Ahmad, *Principles of Corrosion Engineering and Corrosion Control*, 1st Edition. Elsevier, 2006. doi: 10.1016/B978-0-7506-5924-6.X5000-4.

[65] “Aluminized Steel Sheet,” https://www.alro.com/divsteel/metals_gridpt.aspx?gp=0060#:~:text=Type%201%20aluminized%20steel%20is,dipped%20in%20commercially%20pure%20aluminum.

[66] R. W. Richards, R. D. Jones, P. D. Clements, and H. Clarke, “Metallurgy of continuous hot dip aluminising,” *International Materials Reviews*, vol. 39, no. 5, pp. 191–212, 1994, doi: 10.1179/imr.1994.39.5.191.

[67] American Society for Metals. ; ASM International.; Handbook Committee, *ASM Handbook Volume 3: Alloy Phase Diagrams*. Ohio: ASM International, 1992.

[68] W. J. Cheng and C. J. Wang, “Growth of intermetallic layer in the aluminide mild steel during hot-dipping,” *Surf Coat Technol*, vol. 204, no. 6–7, pp. 824–828, 2009, doi: 10.1016/j.surfcoat.2009.09.061.

[69] P. P. Dey, P. Modak, A. Ghosh, D. Chakrabarti, P. S. Banerjee, and M. Ghosh, “Investigation of phase evolution of Al–Si–Mg coating on hot dipped interstitial-free steel,” *Results in Materials*, vol. 6, no. February, p. 100078, 2020, doi: 10.1016/j.rinma.2020.100078.

[70] P. P. Dey *et al.*, “Studies on the characterization and morphological features of the coating on interstitial free steel dipped in molten Al-Si-Mg alloy at 800 ◦C,” *Journal of Materials Research and Technology*, vol. 9, no. 3, pp. 4788–4805, 2020, doi: 10.1016/j.jmrt.2020.02.104.

[71] H. Azimaee, M. Sarfaraz, M. Mirjalili, and K. Aminian, “Effect of silicon and manganese on the kinetics and morphology of the intermetallic layer growth during hot-dip aluminizing,” *Surf Coat Technol*, vol. 357, no. October 2018, pp. 483–496, 2019, doi: 10.1016/j.surfcoat.2018.10.035.

[72] S. K. Kim, “Hot-dip aluminizing with silicon and magnesium addition I. Effect on intermertallic layer thickness,” *Journal of Korean Institute of Metals and Materials*, vol. 51, no. 11, pp. 795–799, 2013, doi: 10.3365/KJMM.2013.51.11.795.

[73] H. He, W. Gou, S. Wang, Y. Hou, C. Ma, and P. F. Mendez, “Kinetics of intermetallic compound layers during initial period of reaction between mild steel and molten aluminum,” *International Journal of Materials Research*, vol. 110, no. 3, pp. 194–201, Mar. 2019, doi: 10.3139/146.111735.

[74] N. Zhang *et al.*, “Effect of Si on the Growth Behavior of the Fe2Al5 Phase at Al-xSi(liquid)/Fe(solid) Interface During Holding by In-Situ Synchrotron Radiography,” *Metall Mater Trans A Phys Metall Mater Sci*, vol. 51, no. 6, pp. 2711–2718, 2020, doi: 10.1007/s11661-020-05754-9.

[75] B. Lemmens *et al.*, “Deformation induced degradation of hot-dip aluminized steel,” *Materials Science and Engineering A*, vol. 710, no. July 2017, pp. 385–391, 2018, doi: 10.1016/j.msea.2017.10.094.

[76] M. Zhao, Y. Cai, F. Yin, Y. liu, Z. Li, and Q. Yang, “Effect and controlling mechanism of vanadium on Fe–Al interface reaction in Al–Zn bath,” *Surf Coat Technol*, vol. 306, pp. 408–417, 2016, doi: 10.1016/j.surfcoat.2015.12.017.

[77] L. Yajiang, W. Juan, Z. Yonglan, and X. Holly, “Fine structures in Fe_3Al alloy layer of a new hot dip aluminized steel,” *Bulletin of Materials Science*, vol. 25, no. 7, pp. 635–639, 2002, doi: 10.1007/BF02707896.

[78] A. O. Mekhrabov and M. V. Akdeniz, “Effect of ternary alloying elements addition on atomic ordering characteristics of Fe–Al intermetallics,” *Acta Mater*, vol. 47, no. 7, pp. 2067–2075, May 1999, doi: 10.1016/S1359-6454(99)00087-7.

[79] P. Huilgol, K. U. Bhat, and K. R. Udupa, “Hot-dip Aluminizing of Low Carbon Steel in Al & Al-5wt % Cr Baths,” *Mater Today Proc*, vol. 5, no. 11, pp. 24702–24709, 2018, doi: 10.1016/j.matpr.2018.10.268.

[80] D. Pradhan, M. Manna, and M. Dutta, “Al-Mg-Mn alloy coating on steel with superior corrosion behavior,” *Surf Coat Technol*, vol. 258, pp. 405–414, 2014, doi: 10.1016/j.surfcoat.2014.08.061.

[81] H. C. Liang and C. J. Wang, “The hot corrosion resistance of hot-dip aluminized low carbon steel with nickel interlayer under static load,” *Surf Coat Technol*, vol. 350, no. April, pp. 496–501, 2018, doi: 10.1016/j.surfcoat.2018.05.093.

[82] W. J. Cheng, Y. J. Liao, and C. J. Wang, “Effect of nickel pre-plating on high-temperature oxidation behavior of hot-dipped aluminide mild steel,” *Mater Charact*, vol. 82, no. 43, pp. 58–65, 2013, doi: 10.1016/j.matchar.2013.05.007.

[83] M. Li, N. Li, J. Zhang, and C. Zhou, “Inhibiting effect of Ni-Re interlayer between Ni-Al coating and steel substrate on interdiffusion and carburization,” *Surf Coat Technol*, vol. 337, no. December 2017, pp. 68–74, 2018, doi: 10.1016/j.surfcoat.2017.12.065.

[84] M. Manna and M. Dutta, “Improvement in galvanization and galvannealing characteristics of DP 590 steel by prior Cu or Cu-Sn flash coating,” *Surf Coat Technol*, vol. 251, pp. 29–37, 2014, doi: 10.1016/j.surfcoat.2014.03.065.

[85] S. Gembal’ski, “Diffusion aluminizing of steel, cast iron, copper, and titanium,” in *New and progressive heat-treatment methods*, 1967, pp. 4–10.

[86] B. Bouchaud, B. Rannou, and F. Pedraza, “Slurry aluminizing mechanisms of Ni-based superalloys incorporating an electrosynthesized ceria diffusion barrier,” *Mater Chem Phys*, vol. 143, no. 1, pp. 416–424, 2013, doi: 10.1016/j.matchemphys.2013.09.022.

[87] K. Kishore, S. Chhangani, M. J. N. V. Prasad, and K. Bhanumurthy, “Microstructure evolution and hardness of hot dip aluminized coating on pure iron and EUROFER 97 steel: Effect of substrate chemistry and heat treatment,” *Surf Coat Technol*, vol. 409, p. 126783, Mar. 2021, doi: 10.1016/j.surfcoat.2020.126783.

[88] M. Niinomi, Y. Ueda, and M. Sano, “Dissolution of Ferrous Alloys into Molten Aluminium,” *Transactions of the Japan Institute of Metals*, vol. 23, no. 12, pp. 780–787, 1982, doi: 10.2320/matertrans1960.23.780.

[89] S.-H. Hwang, J.-H. Song, and Y.-S. Kim, “Effects of carbon content of carbon steel on its dissolution into a molten aluminum alloy,” *Materials Science and Engineering: A*, vol. 390, no. 1–2, pp. 437–443, Jan. 2005, doi: 10.1016/j.msea.2004.08.062.

[90] T. SASAKI, T. YAKOU, K. MOCHIDUKI, and K. ICHINOSE, “Effects of Carbon Contents in Steels on Alloy Layer Growth during Hot-dip Aluminum Coating,” *ISIJ International*, vol. 45, no. 12, pp. 1887–1892, 2005, doi: 10.2355/isijinternational.45.1887.

[91] S. H. Hwang, J. H. Song, and Y. S. Kim, “Effects of carbon content of carbon steel on its dissolution into a molten aluminum alloy,” *Materials Science and Engineering A*, vol. 390, no. 1–2, pp. 437–443, 2005, doi: 10.1016/j.msea.2004.08.062.

[92] S. Kobayashi and T. Yakou, “Control of intermetallic compound layers at interface between steel and aluminum by diffusion-treatment,” *Materials Science and Engineering A*, vol. 338, no. 1–2, pp. 44–53, 2002, doi: 10.1016/S0921-5093(02)00053-9.

[93] Y. Yürektürk and M. Baydoğan, “Effect of aluminizing and austempering processes on structural, mechanical and wear properties of a SSF ductile iron,” *Mater Res Express*, vol. 6, no. 1, p. 016550, Oct. 2018, doi: 10.1088/2053-1591/aae804.

[94] M. Zamanzade, A. Barnoush, and C. Motz, “A Review on the Properties of Iron Aluminide Intermetallics,” *Crystals (Basel)*, vol. 6, no. 1, p. 10, Jan. 2016, doi: 10.3390/cryst6010010.

[95] P. F. Tortorelli and K. Natesan, “Critical factors affecting the high-temperature corrosion performance of iron aluminides,” *Materials Science and Engineering: A*, vol. 258, no. 1–2, pp. 115–125, Dec. 1998, doi: 10.1016/S0921-5093(98)00924-1.

[96] A. Mohsenifar, M. R. Aboutalebi, and S. H. Aboutalebi, “Effect of High Temperature Oxidation on the Corrosion Behavior of Aluminized Low Carbon Steel in Molten Aluminum,” *Iranian Journal of Materials Science and Engineering*, vol. 12, no. 3, pp. 88–94, 2015, doi: 10.22068/IJMSE.12.3.11.

[97] N. Takata, M. Nishimoto, S. Kobayashi, and M. Takeyama, “Crystallography of Fe_2Al_5 phase at the interface between solid Fe and liquid Al,” *Intermetallics (Barking)*, vol. 67, pp. 1–11, Dec. 2015, doi: 10.1016/j.intermet.2015.07.011.

[98] Z. Ding *et al.*, “Microstructural evolution and growth behavior of intermetallic compounds at the liquid Al/solid Fe interface by synchrotron X-ray radiography,” *Mater Charact*, vol. 136, pp. 157–164, Feb. 2018, doi: 10.1016/j.matchar.2017.12.024.

[99] T. Timmerscheidt *et al.*, “The Role of κ-Carbides as Hydrogen Traps in High-Mn Steels,” *Metals (Basel)*, vol. 7, no. 7, p. 264, Jul. 2017, doi: 10.3390/met7070264.

[100] T. Ma, H. Li, J. Gao, and Y. Li, “Corrosion Behaviour of Cu/Carbon Steel Gradient Material,” *Crystals (Basel)*, vol. 11, no. 9, p. 1091, Sep. 2021, doi: 10.3390/cryst11091091.

[101] S.-H. Hwang, J.-H. Song, and Y.-S. Kim, “Effects of carbon content of carbon steel on its dissolution into a molten aluminum alloy,” *Materials Science and Engineering: A*, vol. 390, no. 1–2, pp. 437–443, Jan. 2005, doi: 10.1016/j.msea.2004.08.062.

[102] S. Kobayashi and T. Yakou, “Control of intermetallic compound layers at interface between steel and aluminum by diffusion-treatment,” *Materials Science and Engineering: A*, vol. 338, no. 1–2, pp. 44–53, Dec. 2002, doi: 10.1016/S0921-5093(02)00053-9.

[103] K. Bouché, F. Barbier, and A. Coulet, “Intermetallic compound layer growth between solid iron and molten aluminium,” *Materials Science and Engineering: A*, vol. 249, no. 1–2, pp. 167–175, Jun. 1998, doi: 10.1016/S0921-5093(98)00573-5.

[104] G. Pasche, M. Scheel, R. Schäublin, C. Hébert, M. Rappaz, and A. Hessler-Wyser, “Time-resolved X-ray microtomography observation of intermetallic formation between solid Fe and liquid Al,” *Metall Mater Trans A Phys Metall Mater Sci*, vol. 44, no. 9, pp. 4119–4123, Sep. 2013, doi: 10.1007/s11661-013-1788-6.

[105] X. Yu, J. Huang, T. Yang, and D. Fan, “The Growth Behavior for Intermetallic Compounds at the Interface of Aluminum-Steel Weld Joint,” *Materials*, vol. 15, no. 10, May 2022, doi: 10.3390/ma15103563.

[106] R. Pretorius, A. M. Vredenberg, F. W. Saris, and R. De Reus, “Prediction of phase formation sequence and phase stability in binary metal-aluminum thin-film systems using the effective heat of formation rule,” *J Appl Phys*, vol. 70, no. 7, pp. 3636–3646, 1991, doi: 10.1063/1.349211.

[107] J.-M. Lee, S.-B. Kang, T. Sato, H. Tezuka, and A. Kamio, “Evolution of iron aluminide in Al/Fe in situ composites fabricated by plasma synthesis method,” *Materials Science and Engineering: A*, vol. 362, no. 1–2, pp. 257–263, Dec. 2003, doi: 10.1016/S0921-5093(03)00639-7.

[108] Prepared under the direction of the ASM International Handbook Committees, *ASM handbook, Alloy Phase Diagrams*, vol. 3. Ohio: Materials Park, ASM International, 1992.

[109] A. Barba Pingarrón, M. A. G. Hernández, V. A. Covelo, and N. R. Valdez, “Corrosion resistance of hot dip aluminized copper alloys,” in *Advanced Materials Research*, Trans Tech Publications Ltd, 2014, pp. 8–13. doi: 10.4028/www.scientific.net/AMR.976.8.

[110] Z. Yu, Y. Duan, L. Liu, S. Liu, X. Liu, and X. Li, “Growth behavior of Cu/AI intermetallic compounds in hot-dip aluminized copper,” *Surface and Interface Analysis*, vol. 41, no. 5, pp. 361–365, May 2009, doi: 10.1002/sia.3020.

[111] Y. Guo, G. Liu, H. Jin, Z. Shi, and G. Qiao, “Intermetallic phase formation in diffusion-bonded Cu/Al laminates,” *J Mater Sci*, vol. 46, no. 8, pp. 2467–2473, Apr. 2011, doi: 10.1007/s10853-010-5093-0.

[112] P. Liberski, A. Gierek, H. Kania, P. Podolski, and A. Tatarek, “Formation of coatings from a liquid phase on the surface of iron-base alloys,” *Archives of Foundry Engineering*, vol. 8, no. 4, pp. 93–98, Jul. 2008.

[113] C. J. Wang, J. W. Lee, and T. H. Twu, “Corrosion behaviors of low carbon steel, SUS310 and Fe–Mn–Al alloy with hot-dipped aluminum coatings in NaCl-induced hot corrosion,” *Surf Coat Technol*, vol. 163–164, pp. 37–43, Jan. 2003, doi: 10.1016/S0257-8972(02)00588-1.

[114] C.-J. Wang and S.-M. Chen, “The high-temperature oxidation behavior of hot-dipping Al–Si coating on low carbon steel,” *Surf Coat Technol*, vol. 200, no. 22–23, pp. 6601–6605, Jun. 2006, doi: 10.1016/j.surfcoat.2005.11.031.

[115] W.-J. Cheng and C.-J. Wang, “Growth of intermetallic layer in the aluminide mild steel during hot-dipping,” *Surf Coat Technol*, vol. 204, no. 6–7, pp. 824–828, Dec. 2009, doi: 10.1016/j.surfcoat.2009.09.061.

[116] C. J. Wang and Mohd. Badaruddin, “The dependence of high temperature resistance of aluminized steel exposed to water-vapour oxidation,” *Surf Coat Technol*, vol. 205, no. 5, pp. 1200–1205, Nov. 2010, doi: 10.1016/j.surfcoat.2010.08.153.

[117] P. Kofstad, “On the formation of porosity and microchannels in growing scales,” *Oxidation of Metals*, vol. 24, no. 5–6, pp. 265–276, Dec. 1985, doi: 10.1007/BF00657061.

[118] R. A. Rapp, “The high temperature oxidation of metals forming cation-diffusing scales,” *Metallurgical Transactions B*, vol. 15, no. 2, pp. 195–212, Jun. 1984, doi: 10.1007/BF02667322.

[119] C. J. Wang and S. M. Chen, “The high-temperature oxidation behavior of hot-dipping Al-Si coating on low carbon steel,” *Surf Coat Technol*, vol. 200, no. 22-23 SPEC. ISS., 2006, doi: 10.1016/j.surfcoat.2005.11.031.

[120] C. J. Wang and Mohd. Badaruddin, “The dependence of high temperature resistance of aluminized steel exposed to water-vapour oxidation,” *Surf Coat Technol*, vol. 205, no. 5, pp. 1200–1205, Nov. 2010, doi: 10.1016/j.surfcoat.2010.08.153.

[121] C. Wagner, “The distribution of cations in metal oxide and metal sulphide solid solutions formed during the oxidation of alloys,” *Corros Sci*, vol. 9, no. 2, pp. 91–109, Jan. 1969, doi: 10.1016/S0010-938X(69)80046-6.

[122] N. Otsuka and R. A. Rapp, “Effects of Chromate and Vanadate Anions on the Hot Corrosion of Preoxidized Ni by a Thin Fused Na_2SO_4 Film at 900°C,” *J Electrochem Soc*, vol. 137, no. 1, pp. 53–60, Jan. 1990, doi: 10.1149/1.2086437.

[123] Alan M. Kruizenga, “Corrosion mechanisms in chloride and carbonate salts,” Livermore, California, 2012. Accessed: Nov. 24, 2022. [Online]. Available: https://www.osti.gov/servlets/purl/1051732

[124] M. Zorc, A. Nagode, J. Burja, B. Kosec, and B. Zorc, “Surface decarburization of the hypo-eutectoid carbon steel C45 during annealing in steady air at temperatures $T > AC_1$,” *Metals (Basel)*, vol. 8, no. 6, 2018, doi: 10.3390/met8060425.

[125] Y. Niu, F. Gesmundo, F. Viani, and W. Wu, “The corrosion of Ni3Al in a combustion gas with and without Na_2SO_4-NaCl deposits at 600-800°C,” *Oxidation of Metals*, vol. 42, no. 3–4, 1994, doi: 10.1007/BF01052027.

[126] C. Ciszak, I. Popa, J.-M. Brossard, D. Monceau, and S. Chevalier, “NaCl induced corrosion of Ti-6Al-4V alloy at high temperature,” *Corros Sci*, vol. 110, pp. 91–104, Sep. 2016, doi: 10.1016/j.corsci.2016.04.016.

[127] Y. Ihara, H. Ohgame, K. Sakiyama, and K. Hashimoto, “The corrosion behaviour of iron in hydrogen chloride gas and gas mixtures of hydrogen chloride and oxygen at high temperatures,” *Corros Sci*, vol. 21, no. 12, pp. 805–817, Jan. 1981, doi: 10.1016/0010-938X(81)90023-8.

[128] D. Koszelow, M. Makowska, F. Marone, J. Karczewski, P. Jasiński, and S. Molin, “High temperature corrosion evaluation and lifetime prediction of porous Fe22Cr stainless steel in

air in temperature range 700–900 °C," *Corros Sci*, vol. 189, p. 109589, Aug. 2021, doi: 10.1016/j.corsci.2021.109589.

[129] M. A. Abro and D. B. Lee, "High temperature corrosion of hot-dip aluminized steel in Ar/1%SO_2 gas," *Metals and Materials International*, vol. 23, no. 1, pp. 92–97, Jan. 2017, doi: 10.1007/s12540-017-6366-9.

[130] G. H. Awan and F. ul Hasan, "The morphology of coating/substrate interface in hot-dip-aluminized steels," *Materials Science and Engineering: A*, vol. 472, no. 1–2, pp. 157–165, Jan. 2008, doi: 10.1016/j.msea.2007.03.013.

[131] M. Yousaf, J. Iqbal, and M. Ajmal, "Variables affecting growth and morphology of the intermetallic layer (Fe_2Al_5)," *Mater Charact*, vol. 62, no. 5, pp. 517–525, May 2011, doi: 10.1016/j.matchar.2011.03.004.

[132] P. P. Dey, P. Modak, A. Ghosh, D. Chakrabarti, P. S. Banerjee, and M. Ghosh, "Investigation of phase evolution of Al–Si–Mg coating on hot dipped interstitial-free steel," *Results in Materials*, vol. 6, p. 100078, Jun. 2020, doi: 10.1016/j.rinma.2020.100078.

[133] W.-J. Cheng and C.-J. Wang, "Observation of high-temperature phase transformation in the Si-modified aluminide coating on mild steel using EBSD," *Mater Charact*, vol. 61, no. 4, pp. 467–473, Apr. 2010, doi: 10.1016/j.matchar.2010.02.001.

[134] H. Wang, S. Sun, X. Li, J. Wang, and X. Su, "Effect of silicon on interfacial reaction and morphology of hot-dip aluminizing," *Journal of Materials Research and Technology*, vol. 20, pp. 3723–3734, Sep. 2022, doi: 10.1016/j.jmrt.2022.08.095.

[135] H. Azimaee, M. Sarfaraz, M. Mirjalili, and K. Aminian, "Effect of silicon and manganese on the kinetics and morphology of the intermetallic layer growth during hot-dip aluminizing," *Surf Coat Technol*, vol. 357, pp. 483–496, Jan. 2019, doi: 10.1016/j.surfcoat.2018.10.035.

[136] N. Takata, M. Nishimoto, S. Kobayashi, and M. Takeyama, "Morphology and formation of Fe–Al intermetallic layers on iron hot-dipped in Al–Mg–Si alloy melt," *Intermetallics (Barking)*, vol. 54, pp. 136–142, Nov. 2014, doi: 10.1016/j.intermet.2014.06.003.

[137] P. Huilgol, K. U. Bhat, and K. R. Udupa, "Hot-dip Aluminizing of Low Carbon Steel in Al & Al-5wt % Cr Baths," *Mater Today Proc*, vol. 5, no. 11, pp. 24702–24709, 2018, doi: 10.1016/j.matpr.2018.10.268.

[138] P. P. Dey *et al.*, "Studies on the characterization and morphological features of the coating on interstitial free steel dipped in molten Al-Si-Mg alloy at 800 °C," *Journal of Materials Research and Technology*, vol. 9, no. 3, pp. 4788–4805, May 2020, doi: 10.1016/j.jmrt.2020.02.104.

[139] S. K. Kim, "Hot-Dip Aluminizing with Silicon and Magnesium Addition I. Effect on Intermertallic Layer Thickness," *Korean Journal of Metals and Materials*, vol. 51, no. 11, pp. 795–799, Nov. 2013, doi: 10.3365/KJMM.2013.51.11.795.

[140] W.-J. Cheng and C.-J. Wang, "Characterization of intermetallic layer formation in aluminide/nickel duplex coating on mild steel," *Mater Charact*, vol. 69, pp. 63–70, Jul. 2012, doi: 10.1016/j.matchar.2012.04.007.

[141] N. Fathy *et al.*, "Influence of Pre-Tinning Process on Coating Morphology and Interface Structure of Low Carbon Steel Dipped in Molten 6061 Al Alloy," *Coatings*, vol. 12, no. 10, p. 1499, Oct. 2022, doi: 10.3390/coatings12101499.

[142] X. Zhao *et al.*, “Preparation and deformation behaviour of multi-structural aluminium-coated steels,” *Surf Coat Technol*, vol. 428, p. 127861, Dec. 2021, doi: 10.1016/j.surfcoat.2021.127861.